Numerical study of electro-thermal effects in silicon devices

Thu Trang Nghiem Thi

UNIVERSITÉ PARIS-SUD

ÉCOLE DOCTORALE : STITS
Institut d'Électronique Fondamentale

***DISCIPLINE** : PHYSIQUE*

THÈSE DE DOCTORAT

soutenue le 25 janvier 2013

par

Thu Trang NGHIEM THI

Numerical study of electro-thermal effects in silicon nanodevices

Directeur de thèse :	Philippe DOLLFUS	Directeur de Recherche (CNRS, IEF, Orsay)
Co-encadrant:	Jérôme SAINT-MARTIN	Maître de Conférences (Université Paris-Sud, IEF, Orsay)
Composition du jury :		
Président du jury :	Mireille MOUIS	Directeur de Recherche (CNRS, IMEP-LAHC, Grenoble)
Rapporteurs :	Jean-Luc THOBEL	Chargé de Recherche (CNRS, IEMN, Lille)
	Jesús Enrique VELÁZQUEZ PÉREZ	Professeur (Université de Salamanque)
Examinateurs :	Jean-Charles BARBÉ	Ingénieur-Chercheur (CEA, LETI, Grenoble)

Acknowledgement

First and foremost, I would like to express my deep gratitude to Philippe DOLLFUS, my supervisor. He has passion in his profession and his indisputable qualities in science, education and humanity. He was always there to help and give me advice, arousing my initiative without force.

I extend my warmest thanks to my co-supervisor Dr. Jerome SAINT MARTIN. In the last two years of my PhD research, he followed, helped and supported me in all activities with spontaneity and sympathy. He was very patient and always willing to listen to me. I also thank him for his guidance in scientific knowledge and French vocational training.

Beside my supervisors, I also would like to thank Claude CHAPPERT and André DE LUSTRAC, the leader of the IEF (Fundamental Electronics Institute), for giving me the opportunity to work in this laboratory.

My grateful thanks also go to Dr. Mireille MOUIS, Dr. Jesús Enrique VELÁZQUEZ PÉREZ, Dr. Jean-Luc THOBEL and Dr. Jean-Charles BARBÉ for their interest in my research and for having accepted to be the reviewers of my PhD thesis. It is a great honour for me to gather you around in my thesis.

I would like to thank my Vietnamese professors Ai-Viet NGUYEN and Van-Lien NGUYEN who have supported me to overcome difficulty in scientific research.

In addition, I would like to thank Valérie AUBRY-FORTUNA for her help in the first year with the **k**.**p** method and also for the good bread that she made. Furthermore, I want to thank Arnaud BOURNEL and Hugues CAZIN D'HONINCTHUN for their sympathy and interesting discussions, Christophe CHASSAT for his support in informatic calculation, Damien QUERLIOZ for his advices in scientific problem and Sylvie RETAILLEAU for her sympathy and dynamic that was transmitted to me each time I met her.

My sincere thanks also go to my colleagues for giving me a sympathetic "laboratory's life". Among my colleagues, I would like to thank Ming SHI for his kindness and availability.

I thanks to Vincent TALBO, Fulvio MAZZAMUTO, Viet-Hung NGUYEN, Huu-Nha NGUYEN, Salim BERRADA and Yann APERTET who gave me a lot of advices and shared their work experiences. Without forgetting anyone, I thank all the colleagues in the team during my stay at the IEF, and all my friends who have supported and helped me during these three years not only in the most difficult times, but also in everyday life.

These acknowledgments would not be complete without thanking my family for their constant support and care. I want to thank my parents Hoa Hồng, my little sister Hồng Nhung, and my little brother Thành Nam. Through their daily support and their love, even distant, I have been encouraged to develop this thesis in the best conditions.

SUMMARY

General introduction

The semiconductor technology is actually scaling down the feature size of transistors towards the nanometer regime to continue increasing the density of devices on a single chip. This strategy has been very effective and successful in the past to improve the overall performance of circuits. However, the power density per unit volume tends to be dependent on the channel length L_g and proportional to $L_g^{-1.7}$ [Rowlette08]; which raises new problems: For a 20 nm channel length device, the power density is in the order of 10 TW/cm^3. Hence, the high current densities flowing in active areas of such small devices generate significant local heating due to phonon emission by hot carriers leading to reductions in performance and even to failures. This phenomenon, called self-heating effect, is identified as one of the most critical for the continued increase in the integration density of circuits.

At this scale, the transport of both electrons (charge) and phonons (heat) are ballistic or quasi-ballistic, accordingly both heat and charge transports are non-stationary.. In addition, the thermal conductivity of semiconductor thin films, in particular silicon (Si) films, is significantly reduced because of the boundary and surface scattering. It is therefore appropriate to model not only the electron transport and the generation of phonons, but also the transport of non-equilibrium phonons and the coupling of the two non-equilibrium populations of particles to evaluate the electro-thermal effects in nanoscale devices.

In this context, the aim of this thesis is to study (i) the heat transport in Silicon nano-structures and in short channel Si MOSFET (Metal-Oxide-Semiconductor Field-Effect Transistor), and (ii) the coupling of non-equilibrium electron and phonon transport in this transistor.

In the first chapter, we review the models that can be used to study the transport of electrons and phonons at deep sub-micron dimensions, for which the Boltzmann transport equation (BTE) describes well the transport of both electrons and phonons, together with their coupling in view of electro-thermal simulation.

In the second chapter, a new algorithm to solve the steady-state phonon Boltzmann transport equation (pBTE) under relaxation time approximation is presented. The relaxation time set in this work is validated by the comparison of calculated and experimental thermal conductivity of bulk Si. Both analytic and numerical calculations have been implemented and performed. The analytic model can predict the thermal conductivity for various geometries at different scales by including the phonon-boundary scattering, as well as the roughness scattering.

The novelty in the numerical BTE algorithm is the introduction of the scattering temperature at which the relaxation time is calculated and injected in the steady-state pBTE. This scattering temperature is given by the heat diffusion equation. The results on the thermal conductivity of Si bulk are presented as a validation of this algorithm which allows us to describe all transport regimes in Si and their physical origin, from diffusive to ballistic regimes. Then, the same procedure is used to analyse the thermal conductivity of GaAs ballistic point contacts.

In chapter 3, we study the self-heating effects in a 20 nm-channel length double-gate MOSFET. The phonon generation in Si bulk and in Si DG-MOSFET is extracted from electron Monte Carlo (eMC) simulation and compared to the simple macroscopic evaluation of the Joule heating. The generation term is used as an input for steady state pBTE solver in this DG-MOSFET. The temperatures, thermal flux and the non-equilibrium transport are investigated for different bias conditions.

The procedure of coupled non-equilibrium electro-thermal simulation in this transistor is finally presented in this chapter. The resulting ballisticity, electron velocity, energy and potential are compared with these of the isothermal eMC simulation. The degradation of drain current is estimated as a function of the source-drain bias and the surface roughness.

Etude numérique des effets thermoélectriques dans les nanodispositifs silicium

Introduction

Le développement des technologies de composants pour les filières CMOS ultimes à grille ultra-courte (L < 20 nm) se heurte à de nombreuses difficultés technologiques, mais également à des limites thermiques qui perturbent notablement les règles de mise à l'échelle communément employées jusqu'à présent. Les fortes densités de courant obtenues dans des zones actives aussi réduites génèrent un important échauffement local (par effet Joule), lié à l'émission de phonons par les porteurs chauds, qui peut conduire à des réductions très sensibles des performances, voire à des défaillances. Ce phénomène est identifié comme un des plus critiques pour la poursuite de l'augmentation de la densité d'intégration des circuits. Cela est particulièrement crucial dans les technologies SOI (silicium sur isolant), où la présence de l'isolant enterré constitue un frein à l'évacuation de la chaleur.

À l'échelle nanométrique, l'étude théorique de ces phénomènes d'échauffement n'est plus possible par des modèles macroscopiques (coefficient de diffusion de la chaleur) mais nécessite une description microscopique détaillée des transferts de chaleur qui sont localement hors équilibre. Il s'agit donc de modéliser de façon appropriée, non seulement le transport électronique et la génération de phonons, mais aussi le transport de phonons hors équilibre et les interactions phonons-phonons et électrons-phonons.

Le formalisme de l'équation de transport de Boltzmann (BTE) est très bien adapté à l'étude de ce problème. En effet, il est largement utilisé avec succès depuis des années pour l'étude du transport des particules chargées dans les composants semi-conducteurs. Ce formalisme est cependant beaucoup moins commun pour étudier le transport des phonons bien qu'il soit en principe très approprié. La difficulté provient du couplage de la BTE des électrons et celle des phonons.

Au cours de ce travail de thèse, un algorithme de calcul du transport de phonons par résolution directe de la BTE a été développé. Ce modèle est présenté au chapitre 1. Ensuite, le chapitre 2 décrit le couplage au transport électronique simulé par le logiciel "MONACO", basé sur une résolution statistique (ou Monte Carlo) de la BTE, développé dans l'équipe. Finalement, ce nouveau simulateur électro-thermique a été utilisé pour étudier les effets

d'auto-échauffement dans les nano-transistors. L'intérêt principal de ces travaux est de permettre une analyse du transport électro-thermique au-delà du formalisme de Fourier. En effet, il donne accès aux distributions locales de phonons dans le dispositif pour chaque mode de phonon. En particulier, ce simulateur apporte une meilleure compréhension des effets des électrons chauds au niveau des points chauds et leur relaxation dans les accès.

Sommaire

Chapitre 1 : Introduction

Dans ce chapitre, nous passons en revue les modèles qui peuvent être utilisés pour étudier le transport des électrons et des phonons dans des structures submicroniques en utilisant l'équation de transport de Boltzmann (BTE). On détaille en particulier les modèles de la littérature couplant les deux équations, en vue de simuler le transport électro-thermique [Sadi12, Vasileska10, Kamakura10, Ni12].

Parmi les principales méthodes de résolution de la BTE, une résolution statistique de type Monte-Carlo a été retenue pour résoudre le transport électronique. Cette méthode éprouvée permet de décrire rigoureusement le transport d'électrons hors d'équilibre qui a lieu dans les dispositifs réels de taille nanométrique. Nous avons donc utilisé le simulateur MONACO

développé dans l'équipe [HDRDollfus99]. Pour le transport des phonons, notre choix s'est porté sur une résolution directe de la BTE, dans l'approximation du temps de relaxation. Nous avons développé un nouveau modèle à cet effet, couplé ensuite à MONACO.

Chapitre 2 : Modèles de transport de phonons et conductivités thermiques des nanostructures

Dans ce chapitre, nous détaillons les modèles utilisés pour décrire le transport thermique dans cette thèse. L'équation de transport de Boltzmann (BTE) est utilisée pour décrire le transport des phonons dans des structures submicroniques. Les modèles utilisés pour décrire les différents mécanismes d'interactions sont présentés. Le modèle numérique de résolution de la BTE est également détaillé. Ensuite, des conductivités thermiques dans des nanostructures (Films, fil Si, GaAs) sont calculées. Enfin, on illustre les différents régimes de transport de phonons du diffusif au balisitique.

Modèle de transport

Formalisme de Boltzmann

Les modèles utilisés dans cette thèse sont basés sur l'équation de transport de Boltzmann (BTE) qui est l'équation d'évolution de la fonction de distribution $f\left(\vec{r},\vec{k},t\right)$. Cette fonction décrit la densité de probabilité d'une particule d'être à la position $\vec{r}$ et d'avoir un vecteur d'onde $\vec{k}$ à l'instant *t*. La connaissance de cette fonction permet de calculer toutes les grandeurs physiques pertinentes liées à la population de phonons : énergies, vitesse…

De façon très générale, la BTE s'écrit comme :

$$\frac{\partial f}{\partial t}+\vec{v}\cdot\nabla_{\vec{r}}f+\frac{\vec{F}}{\hbar}\cdot\nabla_{\vec{k}}f=\left.\frac{\partial f}{\partial t}\right|_{coll}$$

où $\vec{r}$, $\vec{k}$ et *t* sont la position, le vecteur d'onde et le temps. *v* est la vitesse de particule, $\vec{F}$ est la force externe appliquée aux particules et h est la constante de Planck réduite. Pour les phonons, il n'y a pas de force appliquée et le terme correspondant disparaît de l'équation.

La détermination l'intégrale du terme de collision $\left.\frac{\partial f}{\partial t}\right|_{coll}$ est une difficulté majeure dans la résolution de la BTE, spécialement pour les phonons.

Aussi, l'intégrale de collision est souvent simplifiée en écrivant la fonction de distribution hors-équilibre comme :

$$\left.\frac{\partial f}{\partial t}\right|_{coll} = -\frac{f - f_S}{\tau}$$

Où τ est un temps de relaxation qui décrit comment la fonction de distribution relaxe vers f_S qui est la distribution d'équilibre. Cette simplification est appelée l'approximation du temps de relaxation (RTA). Cette approximation est valable lorsque la diffusion est isotrope. Le temps caractéristique τ peut être vu comme un temps moyen entre deux collisions.

Relation de dispersion des phonons

Dans ce travail, nous utilisons la dispersion isotrope et quadratique proposé par Pop *et al*. [Pop05]. Cette dispersion donne une bonne approximation dans la direction cristalline (100). Elle s'écrit sous la forme : $\omega_s = \omega_{0s} + v_s \cdot q + c_s \cdot q^2$

Mécanismes d'interaction des phonons

Les interactions à trois-phonons liés aux effets anharmoniques sont de deux types : Normal et Umklapp. Le modèle utilisé dans cette thèse provient du modèle de Holland [Holland63]. Le temps de relaxation pour les phonons optiques dans le Silicium a été fixé à 3.5 ps [Menéndez84].

$$\tau_{NU} = B_L \omega^2 T^3 \left(\text{LA, Umklapp} + \text{Umklapp}\right)$$

$$\tau_N^{-1} = B_{TN} \omega T^4 \left(\text{TA, Normal}\right)$$

$$\tau_U^{-1} = \begin{cases} 0 & \left(\text{TA, Umklapp for } \omega < \omega_{1/2}\right) \\ B_{TU}\omega^2 \,/\, \sinh\left(\dfrac{\hbar\omega}{k_B T}\right) & \left(\text{TA, Umklapp for } \omega > \omega_{1/2}\right), \end{cases}$$

où $\omega_{1/2}$ est la fréquence qui correspond à $q/q_{max} = 0.5$, et B_L, B_{TN} et B_{TU} sont des paramètres empiriques [Holland63].

Pour les interactions avec les impuretés, nous avons utilisé le modèle développé par [Asheghi02], avec un temps de relaxation qui s'écrit sous la forme ;

$$\tau_{impurity}^{-1} = \left(A_{\delta M} + A_{\delta R} + A_x\right) \cdot \omega^4 ,$$

Où $A_{\delta M}$, $A_{\delta R}$ et A_x sont de paramètres empiriques décrivant l'influence respectivement de la différence de masse δM entre une impureté et un atome du cristal, de la différence δR entre la distance impureté-atome et la distance atome-atome dans le cristal, et enfin du niveau de dopage et de la nature du dopant.

Pour décrire les interactions aux frontières du cristal, nous utilisons le modèle de Holland avec un temps de relaxation de la forme [Holland63] :

$$\frac{1}{\tau_b}=\frac{v_g}{LF}, L=\frac{2}{\sqrt{\pi}}\sqrt{l_1 l_2}$$

Où L est la section de l'échantillon et F est un facteur représentant la correction liée à la rugosité de la surface et au rapport longueur/épaisseur de l'échantillon.

Conductivités thermiques analytiques

Dans le formalisme de Boltzmann la conductivité thermique s'écrit :

$$K_s = \sum_{s=LA,TA} \frac{1}{3}\cdot\int_0^G \frac{\hbar\omega_s^2(q)}{k_B T^2}.v_s^2(q).\tau_s(q)\cdot\frac{\exp(X_s)}{(\exp(X_s)-1)^2}q^2\frac{dq}{2\pi^2}. \qquad (2.17)$$

En utilisant les temps de relaxation présentés précédemment, les conductivités thermiques dans des barreaux massifs de silicium ont été calculées pour valider l'approche. Ensuite, des conductivités thermiques dans des nanofilms de Si et des nanofils de Si et de GaAs ont été évaluées. En particulier, les estimations de ce modèle ont été comparées avec succès avec des mesures sur des fils réalisé dans le laboratoire dans le groupe MicroNanoBio. Ces résultats pour des fils de section rectangulaire d'épaisseur 160 nm et de largeurs 80 nm, 140 nm, 200 nm et 260 nm sont rappelés ci-dessous.

Les valeurs de rugosité qui donnent les meilleurs résultats sont raisonnables par rapport à la technologie utilisée.

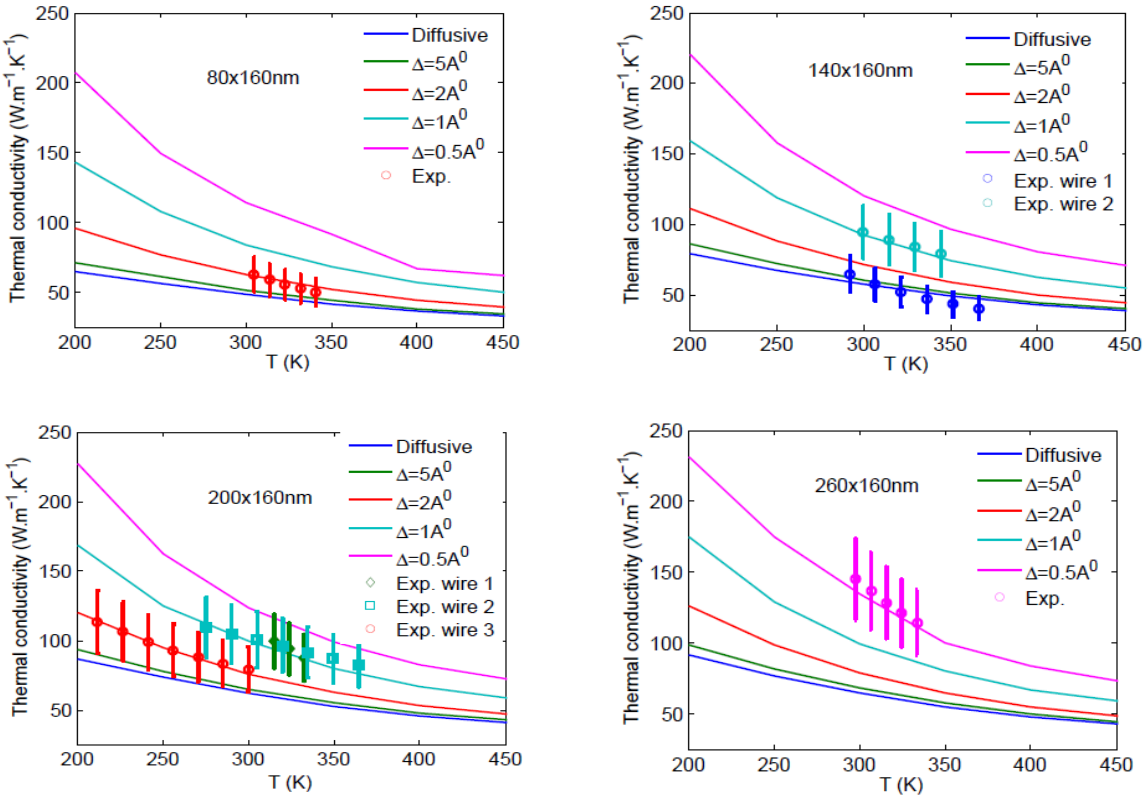

Résolution numérique de la BTE

Pour aller au-delà de la résolution de la BTE en situation de quasi équilibre (modèle précédent de conductivité thermique), une méthode numérique originale pour résoudre l'équation de Boltzmann stationnaire pour les phonons est présentée.

Ce modèle comprend les phonons LA et TA avec la relation de dispersion quadratique (voir chapitre I) et le modèle modifié de Holland pour les interactions dans l'approximation du temps de relaxation. La solution de l'équation de la chaleur de Fourier est couplée pour estimer la température intervenant dans le terme d'interaction, c'est à dire la température T_{scatt} dans les équations suivantes :

Pour les modes optiques, l'équation de transport s'écrit:

$$\vec{v}_{g,s}(\vec{q})\cdot\tau_{LTO}(\vec{q})\cdot\vec{\nabla}_{\vec{q}}N_s(\vec{r},\vec{q}) = -\left[N_s(\vec{r},\vec{q}) - N_{s,Tscatt}(\vec{r},\vec{q})\right] + G_s^{e-LTO}(\vec{q},\vec{r})\cdot\tau_{LTO}(\vec{q})$$

Pour les modes acoustiques, l'équation de transport s'écrit:

$$\vec{v}_{g,s}\cdot\tau_s(\vec{q})\cdot\vec{\nabla}_{\vec{q}}N_s(\vec{r},\vec{q})=-\left[N_s(\vec{r},\vec{q})-N_{s,Tscattering}(\vec{r},\vec{q})\right]+G_s^{e-LTA}(\vec{q},\vec{r})\cdot\tau_s(\vec{q})+G_s^{LTO\to LTA}(\vec{q},\vec{r})\cdot\tau_s(\vec{q}),$$

Le terme $G^{LTO->LTA}$ est un terme calculé selon une approche similaire à celle de [Rowlette08] afin de prendre en compte la relaxation des modes optiques en modes acoustiques tout en essayant de garantir la conservation de l'énergie.

Les équations sont discrétisées en utilisant l'approche des différences finies. Les températures à chaque extrémité sont fixées. Le transport le long des dispositifs est supposé adiabatique.

Validation et conductivités thermiques.

Ce modèle est utilisé pour calculer la conductivité thermique dans les films de silicium dans la plage de température de [100 K-600 K]. Les prédictions numériques sont en très bon accord avec les données expérimentales pour le silicium pur jusqu'à150 K. L'interaction phonons-bord est prise en compte pour prévoir la conductivité dans le plan (in-plane) ainsi que la conductivité transverse (cross-plane). La conductivité thermique dans le plan (in-plane) correspond très bien aux données expérimentales. En outre, la conductivité transverse (cross-plane) qui est jusqu'à présent difficile à mesurer expérimentalement est étudiée avec notre modèle de BTE. La conductivité transverse résultante est plus proche de l'expérience que d'autres approches théoriques.

Nos résultats numériques sont évalués avec succès dans différents régimes de transfert de chaleur, de diffusif à balistique, comme l'illustre la figure ci-dessous. Notre méthode est en d'accord avec la loi de Stefan-Boltzmann à la limite balistique et à la loi de Fourier dans la limite du régime diffusif.

De plus, les occupations de phonons LA et TA ont été étudiées pour illustrer clairement ces différents régimes de transport.

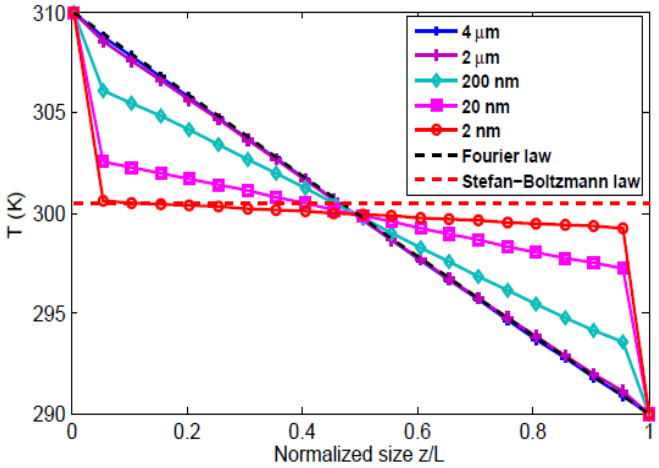

Nanofils de GaAs

Par cette approche les conductances thermiques de nanofils de GaAs ont aussi été évaluées. Une dispersion sinusoïdale et des paramètres d'interaction spécifiques au matériau GaAs massif ont été ajustés. Des conductances thermiques de nano-piliers de 4 nm et 6 nm de diamètre en bon accord avec les valeurs mesurées ont été obtenues. Notre approche montre que pour des piliers nanométriques (6 nm de long) fonctionnent très probablement en régime balistique pour des températures inférieures à 100 K.

Chapitre 3 : Génération de phonons et effet d'auto-échauffement dans les dispositifs de Si

Dans ce chapitre, nous nous concentrons sur la génération de phonons dans le matériau Si massif puis dans des nano-transistors SOI, en particulier dans un MOSFET à double-grille (DG-MOSFET). Puis, nous étudions le transport de phonons dans un tel dispositif grâce au modèle présenté dans le chapitre précédent.

Enfin, le couplage entre les transports d'électrons et de phonons est réalisé. Les effets électro-thermiques sont analysés.

Génération de phonons

En utilisant le simulateur Monte Carlo (MONACO) et en tenant compte de la dispersion quadratique pour les phonons, nous obtenons les phonons générés par les interactions électron-phonon dans les dispositifs de Si. Le transistor étudié est le suivant :

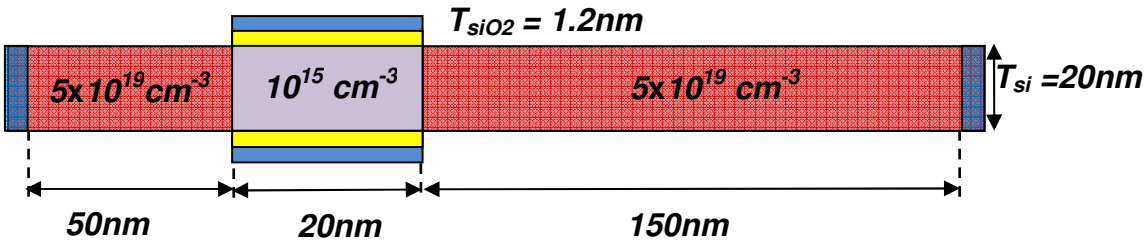

Le drain est étendu pour que les électrons puissent relaxer totalement leur énergie avant d'atteindre le contact.

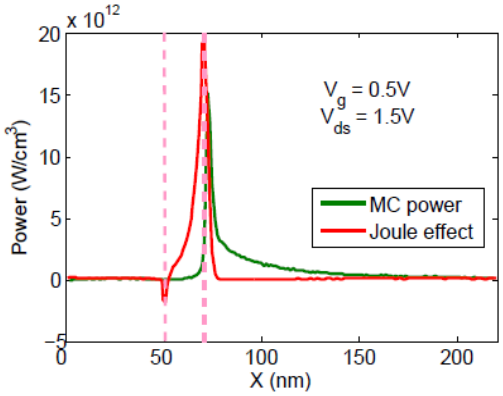

Comme illustré sur la figure ci-dessus, la dissipation thermique (principalement composé de LA et TA) a été comparée à une approche macroscopique(J.E). Un grand écart est observé entre ces deux modèles à la fin du canal. En effet, ce n'est pas là où le champ électrique est le plus fort que la majorité des phonons est réellement générée. Cela est en contradiction avec l'approche macroscopique qui localise mal la génération thermique.

Transport de phonons

Notre modèle inclut la décroissance des phonons optiques vers les modes acoustiques. Notre étude a mis en évidence deux populations de phonons hors équilibre. L'une est généré par les électrons chauds, l'autre par la décroissance des modes optiques. On constate néanmoins que cet écart est relativement faible et que l'utilisation de la distribution de Bose-Einstein dans ces dispositifs reste globalement pertinente.

Transport couplé des électrons et des phonons - Auto-échauffement

Enfin, nous avons couplé le transport des électrons et phonons dans les DG-MOSFET. Comme schématisé ci-dessous, une boucle de simulation comprend une résolution e-MC suivis par une résolution pBTE. Au début de chaque boucle, les taux d'interaction des électrons dans le simulateur Monte Carlo sont modifiés pour tenir compte de la température effective obtenue à partir de la solution de la BTE pour les phonons. La convergence est atteinte après seulement 3 ou 4 boucles.

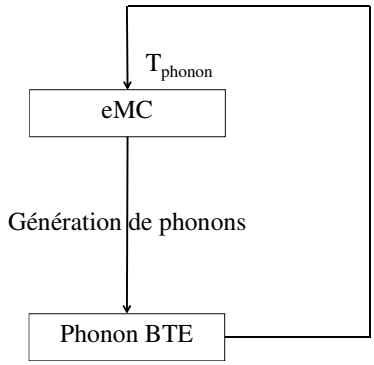

Les effets électro-thermiques dans les DG-MOSFET ont été analysés : on observe notamment une modification de la température effective, du flux thermique, du potentiel électronique, de la vitesse des électrons et de leur énergie.

Les effets électro-thermiques augmentent le nombre d'interactions subies par les électrons le long du dispositif, et diminue donc la balisticité. Par conséquent, la vitesse et l'énergie des électrons sont réduites par rapport au cas de la simulation isotherme à 300K.

Le courant est aussi diminué, avec une dégradation de courant qui peut atteindre 8.1% à la polarisation de V_g = 0.5V, V_{ds} = 1.5V, comme on peut le voir sur la figure ci-dessous. Il s'avère également que le profil de température et la dégradation de courant dépendent de la rugosité de l'interface silicium/oxyde.

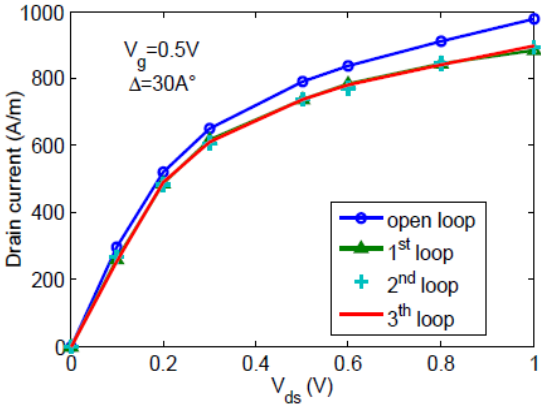

Conclusion

Au cours de ce travail de thèse nous avons développé un algorithme de calcul du transport de phonons par résolution directe de la BTE des phonons. Ce modèle a ensuite été couplé au le logiciel "MONACO" de transport électronique basé sur une résolution statistique (Monte Carlo) de la BTE, développé auparavant dans l'équipe. Finalement, ce nouveau simulateur électro-thermique a été utilisé pour étudier les effets d'auto échauffement dans les nano-transistors. L'intérêt principal de ces travaux est de permettre une analyse du transport électro-thermique au-delà du formalisme de Fourier. En effet, il donne accès aux distributions locales de phonons dans le dispositif, et ce pour chaque mode de phonon. En particulier, ce simulateur apporte une meilleure compréhension des effets des électrons chauds au niveau des points chauds et leur relaxation dans les accès.

Chapter I: INTRODUCTION

1. INTRODUCTION TO MOSFETs

Silicon (Si) based integrated circuits (ICs) have become the pivot of today's semiconductor world [Slisher12]. The heart of the Si based ICs is the transistor, dominated by CMOS (Complementary Metal Oxide Semiconductor) [Thompson] which makes use of both n-channel and p-channel MOSFETs (Metal Oxide Semiconductor Field Effect Transistors).

The semiconductor technology is actually scaling down the feature size of transistors towards the nanometer regime to continue increasing the density of devices on a single chip. This strategy has been very effective for many years to improve the overall performance of circuits. The size of device is governed by the Moore's law which predicts that the number of transistors per integrated circuit doubles every 24 months. In 2012, the 22 nm is introduced as the next CMOS step following the 32nm step on the International Technology Roadmap for Semiconductor (ITRS).

The short channel effects, such as threshold voltage roll-off and drain-induced-barrier-lowering [Kumar05], increase significantly as the gate length of semiconductor devices is reduced to the nanometer scale. In short channel devices, electron transport can be quasi-ballistic or even ballistic with a ballisticity up to 65% [StMartin04-1, StMartin04-2]. In a quasi-ballistic and ballistic channel, electrons injected from the source region to the drain region do not undergo or undergo few scattering when they cross the channel. Their energy gained in the electric field cannot be relaxed efficiently along their trajectory via the lattice through electron-lattice collisions. Therefore, a non-equilibrium situation occurs, referred as hot electron transport. An over-population of phonons is emitted in the drain extension beyond the gated region of the channel, which induces local heating. Hot electron phenomena have become an important issue for the understanding of modern ultra-scale semiconductor devices [Young89, Balkan99, Vitusevich03]. This unwelcome effect gives rise to a degradation of transistor characteristics and may lead to circuit failure.

Numerical simulation can greatly reduce the design cost of new devices. That is mandatory not only for the device engineering, but also for the understanding of underlying fundamental physics. At the beginning, analytical MOS models were relevant in device modeling. But when the gate length was scaled down to the submicron-scale short channel and hot-electron

effects became a problem and analytical modeling had to be backed by more advanced models [Jungeman03].

The main approaches in ultra-scale semiconductor simulation (for electron and also for phonon transport) is solving the semi-classical Boltzmann equation (BTE), the balance equations derived for different moments of the BTE, the hydrodynamic (HD) models [Jungeman03] and the drift-diffusion (DD) one that is the most commonly used and the simplest. Despite their limitations, the two former models are still frequently used in "corrected" releases to include the effects of small size [Odanaka04, Degond04, Degond05, Baro05, Granzner06, Gardner94, Romano01]. However, in the case of deep submicron device, some problems like spurious velocity overshoot or artificially enhanced particles diffusion occur. These problems are avoided by solving the BTE directly. There are two groups of methods: one group consists of direct numerical solvers, and the other one comprises stochastic approaches based on the Monte Carlo (MC) method [Jungeman03]. The MC model includes various scattering mechanisms, the band structure (analytical and/or full band structure). As a result, the MC method is able to provide accurate predictions for non-equilibrium effects occurring in short channel devices.

To compare the three models, in Fig. 1.1, we plot the drain currents obtained using the above methods in 20 nm- and 100 nm-long gate MOSFETs. These results are taken from the work of R. Granzner and co-workers [Granzner06].

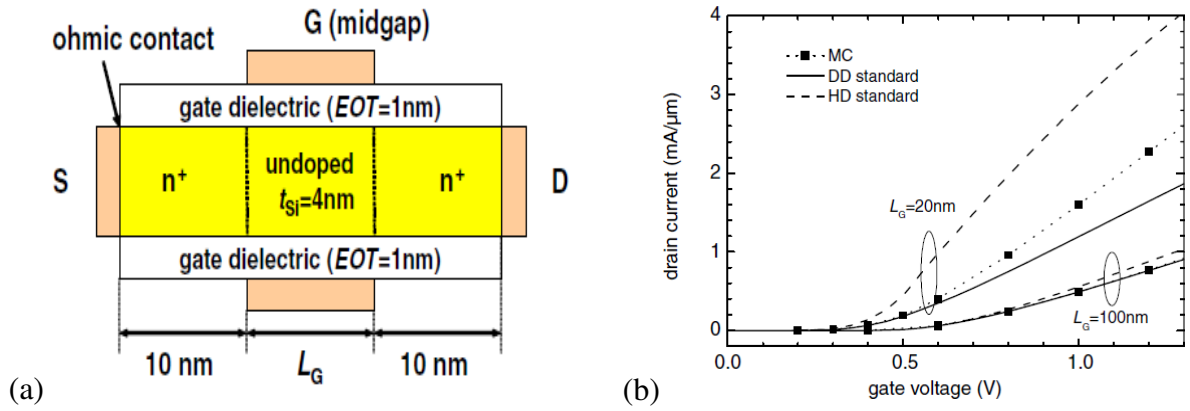

Fig. 1.1. (a) Cross-section of the double gate MOSFETs structure studied. The source and drain regions are doped to 10^{20} cm^{-3}. (b) The drain current as a function of gate voltage for MOSFET of 20nm- and 100nm-gate length obtained using the three models: DD, HD, MC [Granznier06].

They showed that the DD currents are in good agreement with the MC results for the long single-gate device. For the 20-nm gate transistor, however, DD underestimates the on-current by about 25% due to the increasing role of non-stationary carrier transport and ballistic effects [Granzner06].

As the size of the device still decreases, quantum models for electron and phonon transport are necessary to include and explain quantum effects such as quantum interference, size quantization and tunneling current. Such attempts make use of the Wigner function [Querlioz10] or the Green function [Anantram08, HVNguyen09, Mazzamutto11, Mazzamuto12].

An illustration of the hierarchy of transport models is represented in Fig. 1.2.

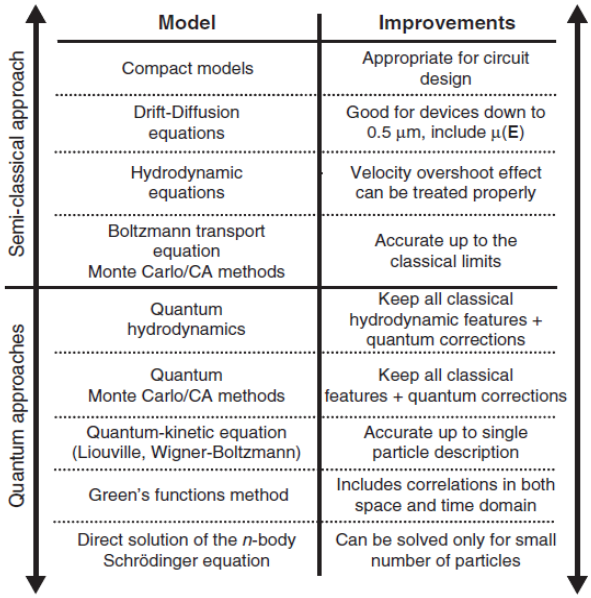

Fig. 1.2. Illustration of the hierarchy of transport models [Vasileska08].

In this work, we focus on devices with sizes comparable to the mean free path of electrons and phonons, in which the BTE describes well enough the transport of electrons and phonons. We describe the electron transport models in section 2 and phonon transport modes in section 3. The main electro-thermal models for transistors are reviewed in section 4. Finally, the aim of the present work will be presented in section 5.

2. ELECTRON TRANSPORT MODELS

In this subsection, a brief introduction into semi-classical transport models: BTE, drift-diffusion and Monte Carlo is presented. These models are well described in many textbooks and reviews ([Jungeman03], [Lungstrom00], [Vasileska08]). Several parts of this section are inspired by these references.

2.1. Boltzmann transport equation

The distribution function $f\left(\vec{r},\vec{k},t\right)$ gives the probability of finding carriers at time *t*, located at a position $\vec{r}$, with a wave vector $\vec{k}$. The BTE accounts for all possible mechanisms by which *f* may change [Lungstrom00]. Here, we represent the BTE in terms of trajectories in position-momentum spaces.

- **The phase space and density function**

The set of all possible positions $\vec{r}$ and wave vector $\vec{k}$ is called the phase space of the system; in other words a set of three coordinates for each position coordinate *x, y, z*, and three more for each momentum component k_x, k_y, k_z. The entire space is 6-dimensional: a point in this space is $\left(\vec{r},\vec{k}\right)=\left(x,y,z,k_x,k_y,k_z\right)$, and each coordinate is parameterized by time *t*. The small volume ("differential volume element") is written $d^3\vec{r}\,d^3\vec{k}=dx\,dy\,dz\,dk_x\,dk_y\,dk_z$.

Since the probability of *N* particles which all have $\vec{r}$ and $\vec{k}$ within $d^3\vec{r}\,d^3\vec{k}$ is in question, at the heart of the equation is a quantity *f* which gives this probability per unit phase-space volume, or probability per unit length cubed per unit momentum cubed, at an instant of time *t*. This is a probability density function: $f\left(\vec{k},\vec{r},t\right)$, defined so that,

$$dN=f\left(\vec{k},\vec{r},t\right)d\vec{r}d\vec{k} \tag{1.1}$$

is the number of particles which all have positions lying within a volume element $d^3\vec{r}$ about $\vec{r}$ and wave vector lying within a wave vector space element $d^3\vec{k}$ about $\vec{k}$, at time *t*. Integrating over a region of position space and momentum space gives the total number of particles which have positions and momenta in that region:

$$N = \int d^3\vec{r} \int d^3\vec{k}\ f\left(\vec{r},\vec{k},t\right) = \underset{positions}{\iiint} \underset{wave\,vector}{\iiint} f\left(x,y,z,k_x,k_y,k_z,t\right) dxdydzdk_x dk_y k_z \,. \tag{1.2}$$

- **General equation (principal form)**

The general equation can be written such as

$$\frac{df}{dt} = \left.\frac{\partial f}{\partial t}\right|_{force} + \left.\frac{\partial f}{\partial t}\right|_{diff} + \left.\frac{\partial f}{\partial t}\right|_{coll} \tag{1.3}$$

where the "force" term corresponds to the forces exerted on the particles by an external influence (not by the particles themselves), the "diff" term represents the diffusion of particles, and "coll" is the collision term - accounting for the forces acting between particles in collisions. Expressions for each term on the right side are provided below.

- **The force and diffusion terms**

Consider particles described by *f*, each of them experiencing an *external* force $\vec{F}$ not due to other particles (see the collision term for the latter treatment).

Suppose at time *t* some particles have energy ε, position $\vec{r}$ within element $d^3\vec{r}$ and wave vector $\vec{k}$ within $d^3\vec{k}$. Note that some authors use the particle velocity $\vec{v} = \hbar^{-1}\partial\varepsilon/\partial\vec{k}$ instead of wave vector $\vec{k}$; in the case of parabolic energy band of effective mass *m*, they are related in the definition of momentum by $\vec{p} = m\vec{v} = \hbar\vec{k}$. If a force $\vec{F}$ instantly acts on each particle, then at time $t + \Delta t$ their position will be $\vec{r} + \Delta\vec{r} = \vec{r} + \hbar\vec{k}\,\Delta t/m$ and wave vector $\vec{k} + \Delta\vec{k} = \vec{k} + \frac{\vec{F}}{\hbar}\Delta t$. Then, in the absence of collisions, *f* must satisfy

$$f\left(\vec{r} + \vec{v}\Delta t, \vec{k} + \frac{\vec{F}}{\hbar}\Delta t, t + \Delta t\right) d^3\vec{r}d^3\vec{k} = f\left(\vec{r},\vec{k},t\right) d^3\vec{r}d^3\vec{k} \tag{1.4}$$

Note that the phase space volume element $d^3\vec{r}d^3\vec{k}$ is constant. However, since collisions do occur, the particle density in the phase-space volume $d^3\vec{r}d^3\vec{k}$ changes, so

$$
\begin{aligned}
dN_{coll} &= \left(\frac{\partial f}{\partial t}\right)_{coll} \Delta t\, d^3\vec{r}\, d^3\vec{k} \\
&= f\left(\vec{r}+\vec{v}\Delta t, \vec{k}+\frac{\vec{F}}{\hbar}\Delta t, t+\Delta t\right) d^3\vec{r}\, d^3\vec{k} - f\left(\vec{r},\vec{k},t\right) d^3\vec{r}\, d^3\vec{k} \\
&= \Delta f\, d^3\vec{r}\, d^3\vec{k}
\end{aligned}
\tag{1.5}
$$

where Δf is the total change in *f*.

Dividing (1.5) by $d^3\vec{r}\, d^3\vec{k}\, \Delta t$ and taking the limits $\Delta t \to 0$ and $\Delta f \to 0$, we have

$$
\frac{df}{dt} = \left.\frac{\partial f}{\partial t}\right|_{coll} \tag{1.6}
$$

The total difference of *f* is:

$$
\begin{aligned}
df &= \frac{\partial f}{\partial t}dt + \left(\frac{\partial f}{\partial x}dx + \frac{\partial f}{\partial y}dy + \frac{\partial f}{\partial z}dz\right) + \left(\frac{\partial f}{\partial k_x}dk_x + \frac{\partial f}{\partial k_y}dk_y + \frac{\partial f}{\partial k_z}dk_z\right) + G\left(\vec{r},\vec{k},t\right)dt \\
&= \frac{\partial f}{\partial t}dt + \overrightarrow{\nabla_{\vec{r}}} f \cdot d\vec{r} + \overrightarrow{\nabla_{\vec{k}}} f . d\vec{k} + G\left(\vec{r},\vec{k},t\right)dt \\
&= \frac{\partial f}{\partial t}dt + \overrightarrow{\nabla_{\vec{r}}} f \cdot \vec{v}\, dt + \overrightarrow{\nabla_{\vec{k}}} f . \frac{\vec{F}}{\hbar}dt + G\left(\vec{r},\vec{k},t\right)dt
\end{aligned}
\tag{1.7}
$$

Where $G\left(\vec{r},\vec{k},t\right)$ is the generation rate, $\overrightarrow{\nabla_{\vec{r}}}$, $\overrightarrow{\nabla_{\vec{k}}}$ are the spatial and reciprocal gradient operator, respectively and "·" is the dot product.

- **General equation (stronger form)**

Dividing (1.7) by *dt* and substituting into (1.6) gives the stronger form of the equation:

$$
\frac{\partial f}{\partial t} + \vec{v}\cdot\nabla_{\vec{r}} f + \frac{\vec{F}}{\hbar}\cdot\nabla_{\vec{k}} f = \left.\frac{\partial f}{\partial t}\right|_{coll} \tag{1.8}
$$

The term on the right hand side is added to describe the effect of collisions between particles; if it is zero then the particles do not collide.

This equation is more useful than the principal one above, yet still incomplete, since *f* cannot be solved unless the collision term in *f* is known. This term cannot be found as easily or generally as the others - it is a statistical term representing the particle collisions, and requires knowledge of the statistics the particles obey, like the Maxwell-Boltzmann, Fermi-Dirac or Bose-Einstein distributions.

- **Integral of the collision term - Relaxation Time Approximation**

Determining the integral of the collision term $\left.\frac{\partial f}{\partial t}\right|_{coll}$ is one major difficulty in the resolution of BTE. The net rate of increase of $f\left(\vec{k},\vec{r},t\right)$ due to collisions is a result of the competition between the in-scattering process (carriers at $\vec{k}'$ could be scattered to $\vec{k}$ thereby increasing *f*) and out-scattering process (carriers at $\vec{k}$ could scatter out decreasing *f*) and is given by

$$\left.\frac{\partial f}{\partial t}\right|_{coll} = \sum_{\vec{k}'} f\left(\vec{k}'\right) S\left(\vec{k}',\vec{k}\right) - \sum_{\vec{k}'} f\left(\vec{k}\right) S\left(\vec{k},\vec{k}'\right) \tag{1.9}$$

The transition rate $S\left(\vec{k}',\vec{k}\right)$ is the probability per second that a carrier at $\vec{k}'$ will scatter to $\vec{k}$ (assuming that the state $\vec{k}'$ is occupied and that state $\vec{k}$ is empty).

The collision integral is commonly simplified by writing the non-equilibrium distribution function as

$$\left.\frac{\partial f}{\partial t}\right|_{coll} = -\frac{f - f_S}{\tau} \tag{1.10}$$

Where τ is a characteristic time which describes how the distribution function relaxes and f_S is a symmetric equilibrium distribution. This approach is called the relaxation time approximation (RTA). This approximation is valid when the scattering is isotropic. The characteristic time, τ, is just the average time between collisions.

In what follows it is better to use the velocity *v* than $\hbar k / m$, which is only true for a parabolic band and is not applicable for the full-band simulation. We will use *v* in the formulas below.

2.2. Drift-diffusion model

The widely used drift-diffusion (DD) current equations can be easily derived from the BTE by considering moments of the BTE. For simplicity, a 1-D geometry is considered at the steady state. With the use of the RTA, the BTE may be written as

$$\frac{e\vec{E}}{\hbar}\frac{\partial f}{\partial \vec{k}}+\vec{v}\frac{\partial f}{\partial x}=\frac{f_0-f}{\tau_f} \tag{1.11}$$

The charge *e* has to be taken with the proper sign of the particle (positive for holes and negative for electrons). The current density is defined as

$$J(x)=e\int_{\vec{v}}\vec{v}f(\vec{v},x)d\vec{v} \tag{1.12}$$

Here, to make easier the access to this definition, the distribution function *f* is rewritten as a function of position *x* and velocity $\vec{v}$. Note that in the case of a parabolic energy band of effective mass *m*, or in the so-called effective mass approximation, the velocity $\vec{v}$ and the wave vector $\vec{k}$ are related by $\vec{p}=m\vec{v}=\hbar\vec{k}$. Then, the Eq. 1.11 is rewritten such as

$$\frac{e\vec{E}}{m}\frac{\partial f}{\partial \vec{v}}+\vec{v}\frac{\partial f}{\partial x}=\frac{f_0-f(\vec{v},x)}{\tau} \tag{1.13}$$

The definition of current density can be related to Eq. 1.13 after multiplying both sides of Eq.1.13 by $\vec{v}$ and integrating over $\vec{v}$. From the right-hand-side of Eq. 1.13, we get

$$\frac{1}{\tau}\left[\int_{\vec{v}}\vec{v}f_0d\vec{v}-\int_{\vec{v}}\vec{v}f(\vec{v},x)d\vec{v}\right]=-\frac{J(x)}{e\tau} \tag{1.14}$$

The equilibrium distribution function is symmetric in $\vec{v}$, and hence the first integral is zero. Therefore, we have

$$J(x)=-e\frac{e\tau}{m^*}E\int_{\vec{v}}\vec{v}\frac{\partial f}{\partial \vec{v}}d\vec{v}-e\tau\frac{d}{dx}\int_{\vec{v}}v^2f(\vec{v},x)d\vec{v} \tag{1.15}$$

Integrating by parts, we have

$$\int_{\vec{v}}\vec{v}\frac{\partial f}{\partial \vec{v}}d\vec{v}=\left[\vec{v}f(\vec{v},x)\right]_{-\infty}^{\infty}-\int_{\vec{v}}f(\vec{v},x)d\vec{v}=-n(x) \tag{1.16}$$

And we can write

$$\int_{\vec{v}}v^2f(\vec{v},x)d\vec{v}=n(x)\left\langle v^2\right\rangle \tag{1.17}$$

Where $\left\langle v^2\right\rangle$ is the average of the square of the velocity. The drift-diffusion equations are derived by introducing the mobility $\mu=\frac{e\tau}{m}$ and replacing $\left\langle v^2\right\rangle$ with its average equilibrium

value $\frac{k_B T}{m}$ for a 1D and $\frac{3k_B T}{m}$ for a 3D case, therefore neglecting thermal effects. The diffusion coefficient D is also introduced and the resulting DD current expression for electrons and holes are

$$\begin{aligned} J_n(x) &= q\,n(x)\,\mu_n E(x) + q\,D_n \frac{dn(x)}{dx} \\ J_p(x) &= q\,p(x)\,\mu_p E(x) - q\,D_p \frac{dp(x)}{dx} \end{aligned}, \tag{1.18}$$

respectively, where q is used to indicate the absolute value of the electron charge.

For the 3D geometry and at stationary state, Eq. 1.19 can be extended under the form

$$\begin{aligned} \vec{J}_n(\vec{r},t) &= q\,n(\vec{r},t)\,\mu_n \vec{E} + q\,D_n \nabla n(\vec{r},t) \\ \vec{J}_p(\vec{r},t) &= q\,p(\vec{r},t)\,\mu_p \vec{E} - q\,D_p \nabla p(\vec{r},t) \end{aligned} \tag{1.19}$$

With $D_n = \frac{k_B T}{q}\mu_n$ and $D_p = \frac{k_B T}{q}\mu_p$.

The complete DD model is based on the Eq. 1.19 and the following set of equations

Continuity equations:
$$\begin{aligned} \frac{\partial n(\vec{r},t)}{\partial t} &= G_n(\vec{r},t) + \frac{1}{q}\nabla \vec{J}_n(\vec{r},t) \\ \frac{\partial p(\vec{r},t)}{\partial t} &= G_p(\vec{r},t) - \frac{1}{q}\nabla \vec{J}_p(\vec{r},t) \end{aligned} \tag{1.20}$$

Poisson's equation: $\nabla\left(\varepsilon \vec{E}\right) = q\left[\,p(\vec{r},t) - n(\vec{r},t) + N_D + N_A\,\right]$ (1.21)

Where $G_n(\vec{r},t)$ and $G_p(\vec{r},t)$ are the net generation-recombination rates. N_D and N_A are the donor and acceptor doping densities, respectively.

In the derivation of Eq. 1.19, the choice of equilibrium (thermal) velocity means that the DD equations are only valid for small perturbations of the equilibrium state (low fields). The validity of the DD equations is empirically extended by introducing field-dependent mobility $\mu(E)$ and diffusion coefficient $D(E)$, obtained from empirical models or detailed calculation to capture effects such as velocity saturation at high electric fields due to hot carrier effects.

In the approach of the DD model, the carrier temperatures are assumed to be in equilibrium with the lattice temperature that is $T_C = T_L$. However, in the presence of a strong electric field,

electrons gain energy from the field and the temperature T_n of the electron gas is elevated. To inform about the average carrier energy is available in form of carrier temperature, the hydrodynamic (HD) model is introduced. Many parameters in this model depend on this average carrier energy, e.g., the nobilities and the energy relaxation times. In the computational electronics community, the necessity for the HD transport model is normally checked by comparison of simulation results for HD and DD simulations [Vasileska08].

2.3. Particle based Monte Carlo method

In the previous sub-section, we have considered the drift-diffusion model that was derived from the BTE. This approximation of the BTE, at some limit, becomes inaccurate or fails completely. In these cases, the Monte Carlo (MC) method is widely used. The MC method solves the BTE by simulating the trajectories of individual carriers. They move through a device under the influence of an electric field and random scattering forces. If the number of simulated particle trajectories is large enough, the average results are a good approximation of the behavior of the device. By using a large ensemble of particles, the time-dependent evolution of electron and hole distributions may be simulated.

To simulate a single free flight stopped by a scattering event, a sequence of random numbers is generated. The first number quantifies the free-flight duration. This duration is determined by a random number r varying from 0 and 1, and by the sum of all scattering rates at a given energy Γ_0. To simplify the treatment, we introduce a fictitious scattering mechanism whose scattering rate always adjust itself in such a way that the total rate is a constant in time. Hence, the free flight duration is given by

$$t_r = -\frac{\ln r}{\Gamma_0}. \tag{1.22}$$

During the free flight the carrier moves in accordance with the Newton's law.

$$\vec{F}_e = \frac{d\vec{p}}{dt} = -q\vec{E} \tag{1.23}$$

At the end of the free flight, the carrier's position and momentum are updated according to the following equations

$$\vec{k}(t) = \vec{k}(0) + \frac{\vec{F}}{\hbar} t \text{ and } \vec{r}(t) = \vec{r}(0) + \int_0^t \vec{v}(t')\,dt' \quad (1.24)$$

According to the scattering effects, we calculate the magnitude and direction of the wave vector after the scattering event. In this step, two more random numbers are then generated to specify the polar and azimuthal angles after scattering.

We assume that the interaction process is instantaneous, which is valid as the interaction time is very small compared to the free flights duration. After the interaction, a new free flight in real and reciprocal spaces occurs. To determine the electrostatic field which governs the particle motion during the free flight, the MC simulator is self-consistently coupled with Poisson equation solver. The boundary conditions to the Poisson equation are carefully studied by the group of J.E. Velázquez-Perez [Volovichev08].

Then, the contribution of each carrier to the electronic concentration n_e is weighted by the time t_m passed in each mesh, such that $n_e = n_e + t_m/\Delta t$. The solution of the Poisson's equation is performed periodically to update the electric field within the device. The time step δt between two solutions is adjusted according to the dielectric relaxation time. The processes are iterated until the stationary state is reached, i.e. when the carrier flux becomes constant.

For moderate and high carrier energies, where MC simulations are typically employed, the energy bands are considered within the non-parabolic approximation, this is frequently used as the model for conduction bands.

For extremely high energies, particularly in the presence of strain, the transport properties in realistic Si devices are affected by a strong anisotropy of the valence band [Thompson06], and a full-band description is necessary.

In the next paragraphs, we describe the general principle of our particular simulator MONACO. MONACO has been developed by our group for 30 years [Hesto84, Galdin92, Brisset94, HDRDollfus99, SaintMartin04, HDRBournel06, Huet08, Querlioz08]. A non-parabolic band structure is used for electrons, while a full-band description is used for hole transport in double gate MOSFETs.

2.3.1. Analytic band structure – Conduction band

The electronic band structures are generally described by an analytic approach based on the effective mass approximation, which provides a direct relationship between wave vector and energy.

The minimum of the conduction band in Si is made of six ellipsoidal valleys which are along the three principal axes and are centered at 85% of the X-Γ distance. These valleys, called Δ valleys, are characterized by a longitudinal effective mass m_l and a transverse effective mass m_t. Taking into account the non-parabolicity coefficient α, leads to energy dispersion is written as [HDRDollfus99]

$$E\left(\vec{k}\right)\left(1+\alpha\cdot E\left(\vec{k}\right)\right)=\frac{\hbar^2}{2m_0}\left(\frac{k_l^2}{m_l}+\frac{k_t^2}{m_t}\right) \tag{1.25}$$

With $\begin{cases} m_l = 0.9163 m_0 \\ m_t = 0.1905 m_0 \\ \alpha = 0.5 \end{cases}$.

The density of states effective mass per valley m_D is defined as $m_D = \left(m_t^2 m_l\right)^{1/3} = 0.32 m_0$.

2.3.2. Full-band valence band structure

Ab initio methods, such as the density functional theory, allow calculating the band structure from first principles (without any fitting parameters) to the price of large computational resources. More efficient semi empirical methods, involving fitting parameters, such as empirical pseudo-potentials (EPM), tight-binding (TB) or *k.p*, are commonly used. The *k.p* method is based on the perturbation theory and some symmetry considerations [Rideau06; Luttinger, Cardona66; Richard04].

For a periodical lattice, the wave functions Φ_{nk} can be expressed in a periodical Bloch function basis (u_{nk}):

$$\Phi_{nk} = \exp\left(i\vec{k}\cdot\vec{r}\right)u_{nk}\left(\vec{r}\right), \tag{1.26}$$

where n is the band number, $\vec{k}$ the reciprocal lattice vector and $\vec{r}$ the (real space) position vector of the atoms.

Using the Bloch theorem and assuming that eigenfunctions (wave functions) and eigenvalues (energies) at state $\vec{k} = 0$ are known, the Schrödinger equation writes:

$$H_k u_{nk} = \left(H_0 + \frac{\hbar}{m_0} \vec{k} \cdot \vec{p} + \frac{\hbar^2 \left| \vec{k} \right|^2}{2m_0} \right) u_{nk} = E_{nk} u_{nk} \tag{1.27}$$

where H_0 is the Hamiltonian at $\vec{k} = 0$, m_0 the free carrier mass, $\vec{p}$ the carrier momentum and E_{nk} the energy associated with a carrier wave vector $\vec{k}$ and a band n.

The Hamiltonian H is projected on a truncated basis, here the Zinc-Blende Γ-centered Bloch functions. The resulting matrix is diagonalized to obtain the eigenenergies and wave functions. Adding spin-orbit interaction gives a better description of the band structure but doubles the size of H. The matrix elements of H depend on interband coupling parameters and eigenenergies at $\vec{k} = 0$. The matrix elements are adjusted to fit the band gap and the effective masses around specific **k**-points. The accuracy of the resulting band structure depends on the number of bands that are taken into account (i.e. the number of Bloch functions of the truncated basis). When "full-zone" $\vec{k} . \vec{p}$ methods are considered, a great number of interband coupling parameters is needed. In this work, the $\vec{k} . \vec{p}$ approach with 30 bands and spin-orbit coupling is used. Due to the lack of experimental data, they are determined thanks to ab initio calculations. To include mechanical strain in the calculation, the other band calculation methods (EPM, TB) treat the strained crystal as a new system. However, taking strain into account in the $\vec{k} . \vec{p}$ formalism, as first introduced by Bir and Pikus [Bir & Pikus74], is straightforward using correctly adjusted deformation potentials [Rideau06].

The influence of biaxial strain, extracted from [Aubry-Fortuna11] can be seen on Fig. 1.3. For unstrained Si, the "heavy hole" band (hereafter called the 1st band) shape is very anisotropic and the "light hole" band (hereafter called the 2nd band) shape is more isotropic. Under strain, the degeneracy at the Γ point is lifted. For compressive strain, the nature of the bands is similar to the unstrained case. For tensile strain, the nature of the bands is inverted at low energy and returns to the unstrained case shape at higher energies. For the 2nd band, the effective mass in the [100] direction does not vary significantly with strain. For the 1st band, it shows a 20% decrease under compressive strain and a 3% decrease under tensile strain.

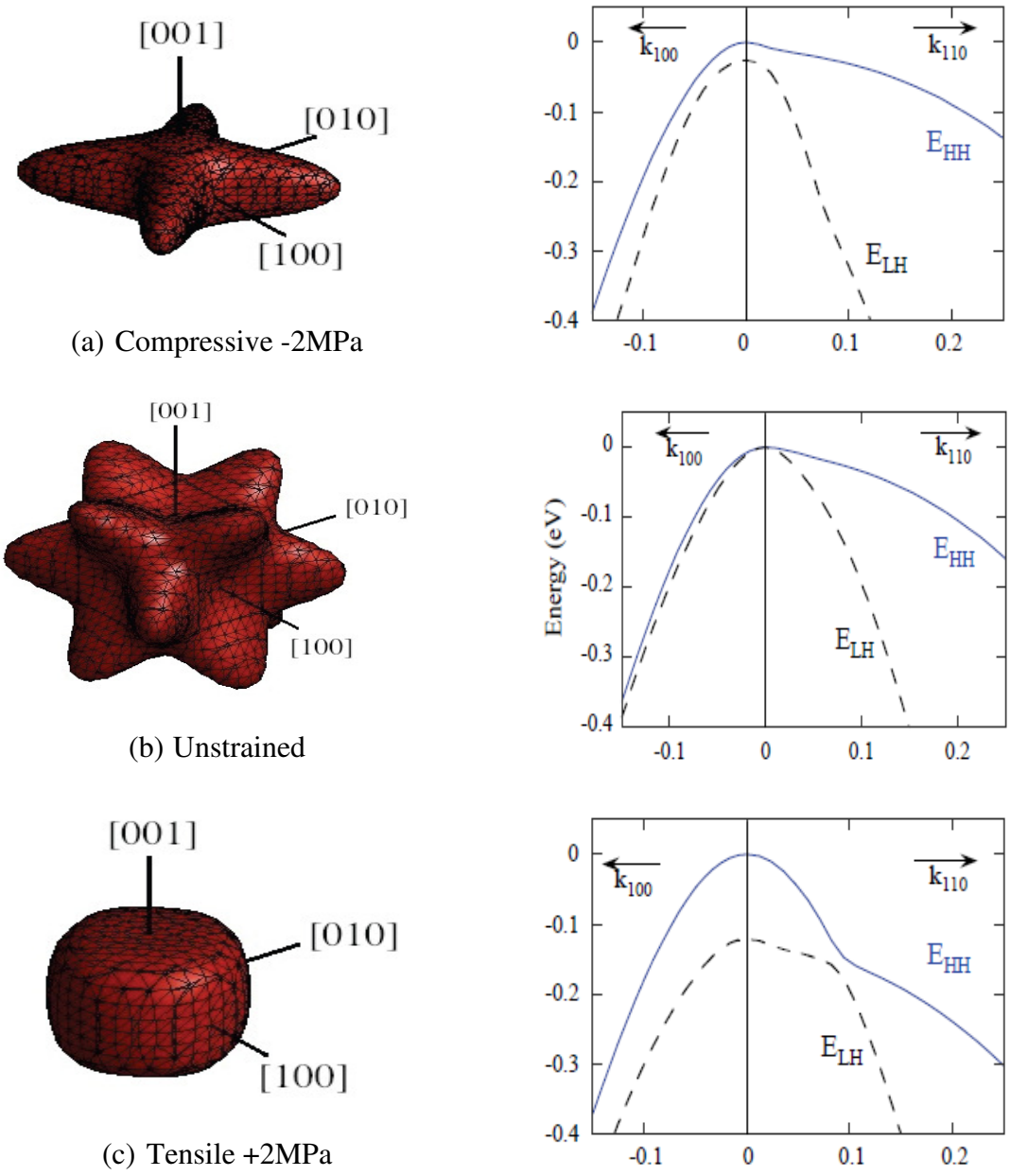

(a) Compressive -2MPa

(b) Unstrained

(c) Tensile +2MPa

Fig. 1.3. Si bandstructures obtained using 30 band *k.p* method with and without strain. On the left: constant energy surface at 40 meV from band edge for the 1st hole band (heavy holes). On the right: corresponding E(k) (eV) in [100] and [110] directions for the 1st (HH) and 2nd (LH) bands. (a) Compressive strain - 2 GPa, (b) unstrained, (c) tensile strain + 2 GPa.

By using the 30 band $\vec{k}.\vec{p}$ approach together with the hypothesis of A.C.H. Rowe [Rowe08], we have successfully reproduced the giant piezo-resistivity in Si nanowires in the first year of my PhD. The main results obtained in this first year are presented in the Appendix A. The giant effect was investigated by He&Yang [He&Yang08] in 2008, while it

was very promising at the beginning of my PhD. But, it has been seriously questioned by the experimental work of [Milne10]. Hence, I have reoriented my PhD subject to the thermal effects in Si structures and the electro-thermal effects in Si devices.

3. PHONON AND PHONON TRANSPORT MODELS

In this subsection, we summarize briefly the basic notions related to heat conduction in a crystalline material. The main vailable models to study the thermal transport in Si such as Fourier model and BTE model (pBTE) will be described. In particular, we will focus on the different approaches to solve the pBTE.

3.1. Lattice vibrations – phonons

The fundamentals of the lattice dynamic properties of a crystal have been widely described [Ziman99], [Kittel71], [Yu&Cardona95].

A crystal may be treated as a three dimensional array of massive particles interacting with each other through interatomic forces. For simplicity, a one dimensional chain with two atoms per unit cell is considered (as illustrated in Fig. 1.4). These atoms which are treated like hard spheres have masses M_1 and M_2, connected by springs with the spring constant C. The lattice constant is a.

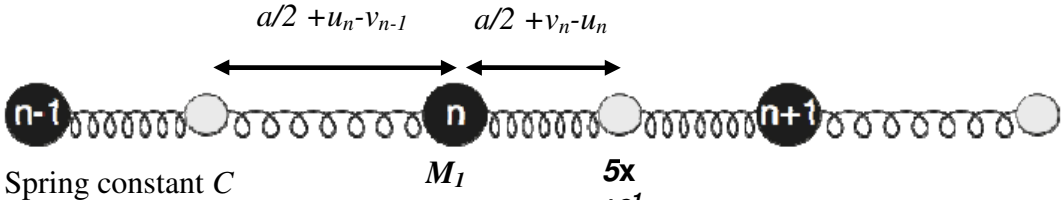

Fig. 1.4. Schema of a 1D chain with two atoms per unit cell.

The equations of motion for this atomic chain can be written in the form of coupled oscillators as:

$$\begin{cases} M_1 \dfrac{d^2 u_n}{dt^2} = C\left(v_n + v_{n-1} - 2u_n\right) \\ M_2 \dfrac{d^2 v_n}{dt^2} = C\left(u_n + u_{n+1} - 2v_n\right) \end{cases} \tag{1.28}$$

Where u_n, u_{n+1} are the displacement from the equilibrium positions of n^{th} and $(n+1)^{th}$ particles of mass M_1; v_n and v_{n-1} are the deviations from the equilibrium positions of n^{th} and $(n-1)^{th}$ particles of mass M_2.

By considering that the plane waves of these oscillators propagate as:

$$\begin{cases} u_s = u \cdot e^{in\vec{q}\vec{a}} \cdot e^{-i\omega t} \\ v_s = v \cdot e^{in\vec{q}\vec{a}} \cdot e^{-i\omega t} \end{cases} \quad (1.29),$$

The dynamic matrix governing the dispersion behavior of the system is:

$$\begin{bmatrix} 2C - M_1\omega^2 & -C\left(1+e^{-i\vec{q}\vec{a}}\right) \\ -C\left(1+e^{-i\vec{q}\vec{a}}\right) & 2C - M_2\omega^2 \end{bmatrix} \cdot \begin{bmatrix} u \\ v \end{bmatrix} = 0. \quad (1.30)$$

This equation in ω yields two roots, i.e. two phonon polarizations (acoustic and optical); the corresponding dependence $\omega\left(\vec{k}\right)$ is called the dispersion relation. The $\omega\left(\vec{k}\right)$ relationship is $\vec{G}_{i(1-3)}$ periodic where $\vec{G}_{i(1-3)}$ are the reciprocal lattice vectors. The dispersion relationships for the optical and acoustic branches are given by:

$$\omega_+^2 = C\left(\frac{1}{M_1}+\frac{1}{M_2}\right) + C\sqrt{\left(\frac{1}{M_1}+\frac{1}{M_2}\right)^2 - \frac{4\sin^2\left(\vec{q}\vec{a}\right)}{M_1M_2}} \text{ (optical branch),} \quad (1.31)$$

$$\omega_-^2 = C\left(\frac{1}{M_1}+\frac{1}{M_2}\right) - C\sqrt{\left(\frac{1}{M_1}+\frac{1}{M_2}\right)^2 - \frac{4\sin^2\left(\vec{q}\vec{a}\right)}{M_1M_2}} \text{ (acoustic branch).} \quad (1.32)$$

These vibrational branches are illustrated in Fig. 1.5.

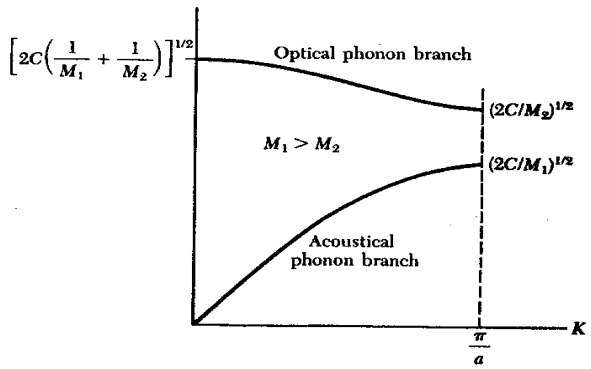

Fig.1.5. Optical and acoustic phonon branches of the dispersion relation for a diatomic linear lattice, showing the limiting frequency at $\vec{q}=0$ and $\vec{q}=\pi/a$, taken from [Kittel71].

The group velocity is the velocity of a wave packet and is defined as

$$\vec{v}_g = \nabla_{\vec{k}}\omega \tag{1.33}$$

If there are p atoms in the primitive cell, there will be $3p$ branches in the phonon dispersion relation: 3 acoustic branches and $3p$-3 optical branches. Thus silicon with two atoms in a primitive cell has six phonon branches: one longitudinal acoustic mode (LA), one longitudinal optical mode (LO), two transverse acoustic modes (TA) and two transverse optical modes (TO). The Fig.1.6 illustrates this relation in Si.

The number of vibration modes in the frequency range $[\omega, \omega+d\omega]$ for polarization s (s = LA, TA) is $D_s(\omega)\,d\omega$ where D_s is the density of states (DOS). The DOS $D_s(\omega)$ of mode s can be derived from the dispersion $\omega(\vec{q})$. In the case of isotropic three-dimensional crystal ($V = L^3$), we will have:

$$D_s(\omega_s)\,d\omega = \frac{Vq^2 d\omega}{2\pi^2 v_g}, \tag{1.34}$$

where g_s is the degeneracy of the considered branch (g_s = 1 for LA and 2 for TA).

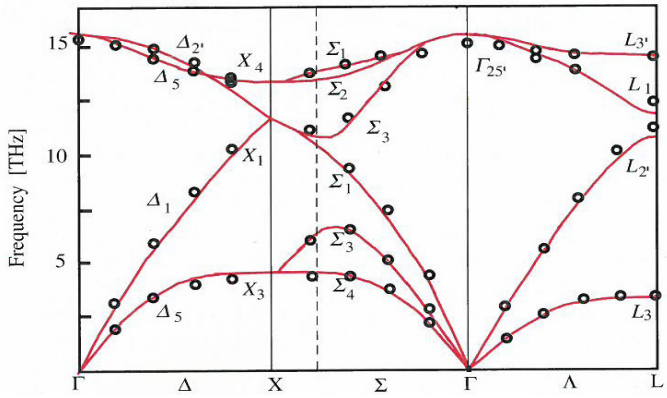

Fig. 1.6. Phonon dispersion curves in Si along high-symmetry axes, taken from [Yu&Cardona95]. The circles are data points from [Nilsson72]. The continuous curves are calculated with the adiabatic bond charge model of Weber ([Weber90]).

The isotropic dispersion relation in Si has been proposed by E. Pop [Pop05], and coworkers in 2004 by using quadratic polynomials, which offers a good fit in the (100) crystal direction. These quadratic dispersions are written as:

$$\omega_s = \omega_{0s} + v_s \cdot q + c_s \cdot q^2. \tag{1.35}$$

The quadratic dispersion coefficients are represented in Table 1.1. The resulting dispersions are plotted in Fig. 1.7a and the group velocity as a function of frequency in Fig. 1.7b. Within this approximation, the Brillouin zone is generally assumed to be a sphere of diameter 2π/a.

	ω_0 10^{13} rad/s	v_s 10^5 cm/s	c 10^{-3} cm^2/s
LA	0	9.01	-2.00
TA	0	5.28	-2.26
LO	9.88	0.00	-1.60
TO	10.20	-2.57	1.11

Table 1.1. Quadratic phonon dispersion coefficients cf. Eq 1.46. [Pop05],

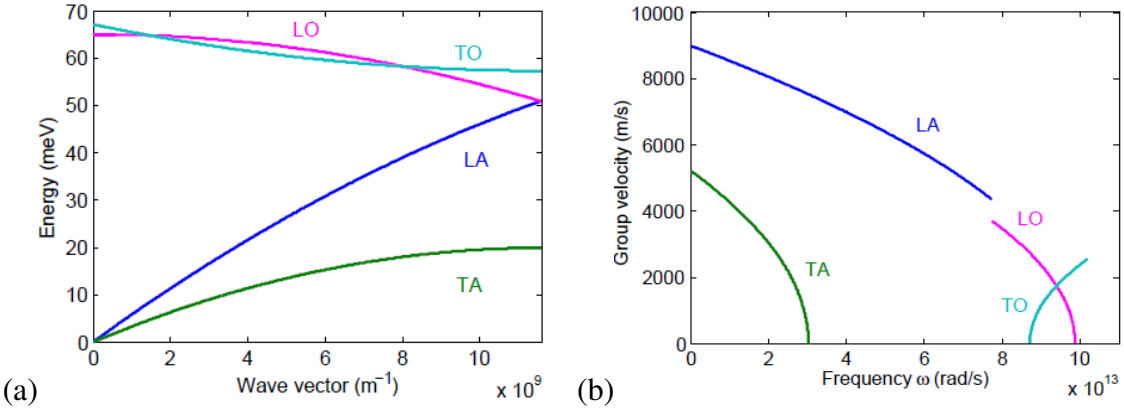

Fig. 1.7. (a) Phonon dispersion in silicon along the (100) direction from quadratic approximation. (b) Group velocity of the four phonon modes as a function of frequency from quadratic approximation.

This approximation is frequently used to treat the phonon transport ([Pop05], [Lacroix05], [Lacroix06], [Sinha06], [Rowlette08], [Martin09], [Terris09], [Mittal10],[Vasileska10] [Ramayya12]).

3.2. Phonon distribution and related quantities

The vibrational energy can be described by the quantum theory of phonons [Kittel71]. Phonons are quanta of the lattice vibrational energy. The energy of a vibrational mode can be written as:

$$\varepsilon = \left(n + \frac{1}{2} \right) \mathrm{h}\omega, \tag{1.36}$$

where n is the phonon occupation number, h is the Planck constant and $\hbar\omega/2$ is the zero point energy of the mode.

The equilibrium distribution of phonons at a temperature T is given by the Bose-Einstein distribution

$$f_{B-E}(\omega) = \frac{1}{\exp\left(\frac{\mathrm{h}\omega}{k_B T}\right) - 1}, \tag{1.37}$$

where k_B is the Boltzmann constant.

- The phonon density corresponding to all phonons of all polarizations is obtained by integrating over all phonon modes

$$N = \sum_{s} \int_{\omega} D_s(\omega) \cdot f_{B-E}(\omega) \cdot g_s \cdot d\omega \ (\text{in m}^{-3}) \tag{1.38}$$

where s is the polarization mode. The phonon density as a function of energy for each phonon mode is plotted in Fig. 1.8.

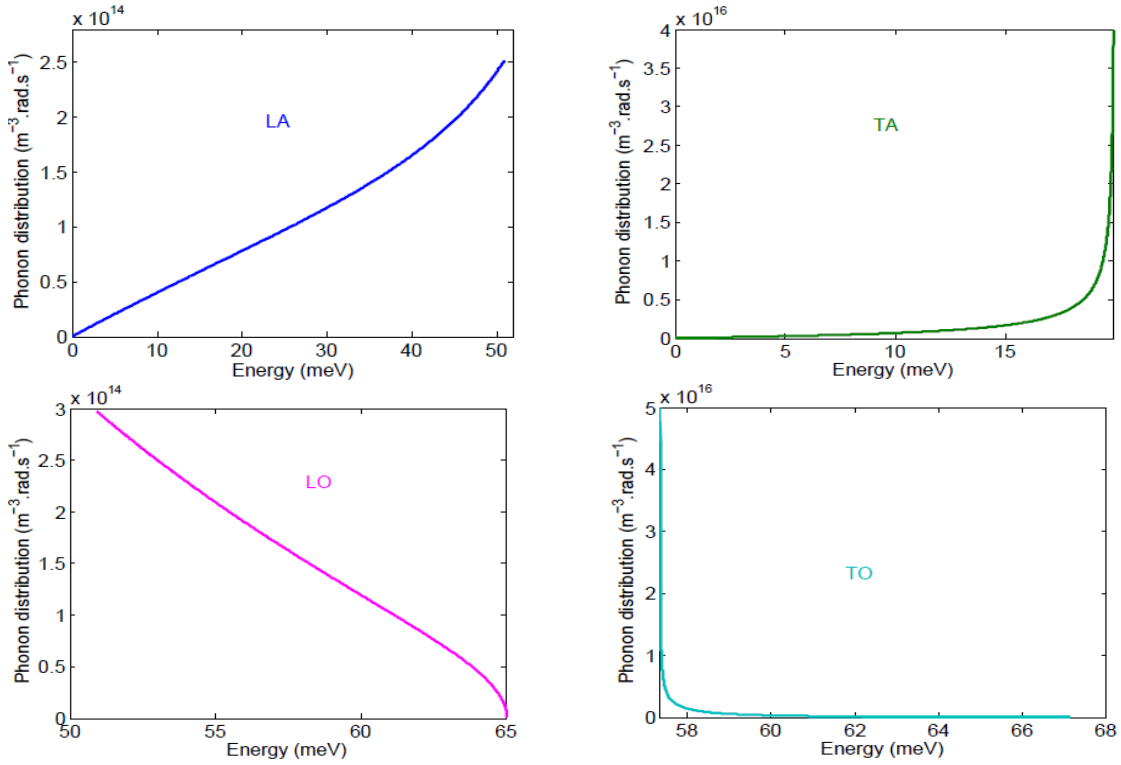

Fig. 1.8. Phonon distribution as a function of energy for four phonon modes: LA, TA, LO and TO.

Then, the evolution of the phonon density (number of phonons in an elementary volume) with temperature is displayed in Fig. 1.9a. The probability to find a phonon of a given mode is shown in Fig. 1.9b.

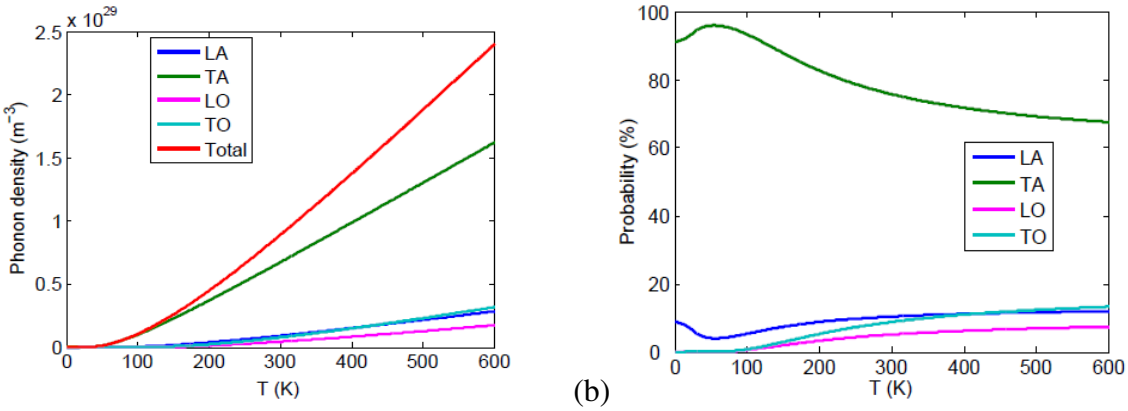

(a) (b)

Fig. 1.9. (a) Total and mode-dependent phonon distribution as a function of temperature. (b) Probability to find a mode as a function of temperature.

- The total lattice energy corresponding to all phonons of all polarizations is obtained by integrating over all phonon modes

$$E = \sum_{s} \int_{\omega} D_s(\omega) \cdot f_{B-E}(\omega) \cdot g_s \cdot \mathrm{h}\omega \cdot d\omega, \tag{1.39}$$

- The volumic phonon heat capacitance $C(\omega, T)$ is defined by

$$C = \frac{\partial E}{\partial T} = k_B \frac{X^2 e^X}{\left(e^X - 1\right)^2}, \tag{1.40}$$

where $X = \mathrm{h}\omega / k_B T$.

- The conductivity coefficient K is also defined with respect to the steady-state flow of heat across a long bar with temperature gradient dT/dz:

$$J = -K \frac{dT}{dz}, \tag{1.41}$$

Where J is the flux of thermal energy (energy transmitted across unit area per unit time).

In the next subsections, we will focus on some common models used to describe for the phonon transport, such as the heat diffusion model and BTE model for phonon (pBTE). We will review the main dispersion relationships that are used: gray model, semi-gray model and

non-gray model. Then the main resolution methods will be presented: analytical solution, the discrete ordinate method and statistical model (Monte Carlo).

3.3. Heat diffusion equation and Fourier's law

The phonons travel through the seconductor and could engage anharmonic interactions with another phonon (phonon-phonon interaction), with electrons, with impurities or with geometric boundaries. Phonon-phonon scattering helps to restore the thermodynamic equilibrium. If the characteristic size is much larger than the mean free path of phonons (the mean distance between two scattering events), the number of scattering events is large. A local thermodynamic equilibrium is achieved and the heat transport occurs within the diffusion regime [MazumderJHT01]. Under these conditions, the heat transport is governed by the standard Fourier heat equation (or diffusion equation)

$$\partial T / \partial t = \nabla \cdot \left(K_T \nabla T \right) , \tag{1.42}$$

Where K_T is the thermal conductivity that depends on the "local" temperature.

When the temperature difference is small (i.e. $K_T = K$ is assumed uniform), the equation can be simplified into:

$$\partial T / \partial t = K \Delta T . \tag{1.43}$$

If the characteristic size of the device is smaller than the phonon mean free path, which is approximately 300 nm in Si at room temperature [Ju99], scattering events are rare, and then a thermodynamic equilibrium even local may not exist in the active region of the semiconductor device. That is the length scale limitation of this model.

3.4. Models based on Boltzmann transport equation (BTE)

The general form of the BTE is described in subsection 1.2.1 (Eq. 1.8). For phonons which are quasi-particles and have no charge, i.e. there is no force term in the BTE becomes

$$\frac{\partial f}{\partial t} + \vec{v}_g \cdot \nabla_{\vec{r}} f = \left. \frac{\partial f}{\partial t} \right|_{coll} , \tag{1.44}$$

where $f = f(\vec{r}, \vec{k}, t)$ is the distribution function of phonons. The space and momentum dependences make the equation very expensive to solve in terms of computation time. A number of approximations have been developed to make it tractable.

As the scattering term is very complex (like in the BTE for electrons), it is common to introduce the relaxation time approximation (RTA) to solve the pBTE:

$$\frac{\partial f\left(\vec{r},\vec{k},t\right)}{\partial t} + \vec{v}_g \cdot \nabla f = \frac{f_{eq}\left(\omega,T\right) - f\left(\vec{r},\vec{k},t\right)}{\tau}. \tag{1.45}$$

Here, f_{eq} is the equilibrium Bose-Einstein distribution function and it depends on both frequency and temperature. The time τ is the effective relaxation time associated with all scattering processes.

3.4.1. Approximation of the dispersion relationship

3.4.1a. Non gray model

The complete details of this model have been described in [Narumanchi04, Narumanchi05]. The acoustic branches are divided into (N_{bands}-1) frequency bands of spread $\Delta\omega_i$ centered around ω_i. The number and spread of the bands are chosen to satisfactorily compute the dispersion curve.

In this model, the pBTE is written for the energy density associated with each band in each angular direction e_ω (J/m^3).

$$\begin{aligned} & e_\omega'''\left(\vec{r},\hat{s},\omega\right) = \hbar\omega f_\omega D\left(\omega\right);\ e''\left(\vec{r},\hat{s}\right) = \int_{\Delta\omega_i} e_\omega''' d\omega \\ & e_\omega\left(\vec{r}\right) = \int_{4\pi} e'' d\Omega\ ;\ e_\omega^0 = \frac{1}{4\pi}\int_{4\pi} e_\omega'' d\Omega = \frac{1}{4\pi} e_\omega \end{aligned}, \tag{1.46}$$

Where e_ω''' is the volumetric energy density per unit frequency per unit solid angle (Js/(m^3.sr.rad)), e_ω'' is the volumetric energy density per unit solid angle (Js/m^3 sr) for a given frequency band, $\vec{r}$ is the position vector, and $\hat{s}$ is the unit direction vector, e_ω^0 is the angular average of the volumetric energy density e_ω. The frequency integration is done over a discrete frequency band $\Delta\omega_i$.

The optical mode for Si has a negligible group velocity $\left(\vec{v}_g \approx 0\right)$ and therefore the pBTE for this mode can be written as

$$\frac{\partial e_0}{\partial t} = \sum_{j=1}^{N_{bands}-1} \left(\int_{T_{ref}}^{T_{oj}} C_o dT - e_0 \right) \gamma_{oj} + q_{vol} \,, \tag{1.47}$$

where $e_o = \int_{T_{ref}}^{T_o} C_o dT$, $\gamma_{oj} = \overline{\left(1/\tau_{oj}\right)} = \frac{1}{\omega_0} \int_{\omega_0} \frac{1}{\tau_{oj}} d\omega$ is the band-averaged inverse relaxation time for the interaction between the optical phonons and the j^{th} band of an acoustic branch, and C_o is the optical mode specific heat. The interaction temperature T_{oj} is defined below in Eq. 1.49. The term q_{vol} is the volumetric heat generation. In microelectronic applications, it would represent the transfer of energy from the energetic electrons to the optical phonons.

The pBTE for the i^{th} frequency band of the acoustic branches (valid for both LA and TA) in the direction $\hat{s}$ is written as

$$\frac{\partial e_i^{"}}{\partial t} + \nabla\left(v_i \hat{s} e_i^{"}\right) = \left(e_i^0 - e_i^{"}\right)\gamma_{ii} + \sum_{\substack{j=1 \\ j\neq 1}}^{N_{bands}} \left\{ \left(\frac{1}{4\pi} \int_{T_{ref}}^{T_{ij}} C_i dT - e_i^{"} \right) \gamma_{ij} \right\} \tag{1.48}$$

$$v_i = \frac{1}{\Delta\omega_i} \int_{\Delta\omega_i} v_\omega d\omega \;;\; C_i = \int_{\Delta\omega_i} C_{\omega_i} d\omega \;;$$

$$e_i^{"} = \int_{\Delta\omega_i} \hbar\omega f_\omega D(\omega) d\omega \;;\; \gamma_{ii} = \overline{\left(1/\tau_{ii}\right)} = \frac{1}{\Delta\omega_i} \int_{\Delta\omega_i} \frac{1}{\tau_{ii}} d\omega \;;$$

$$\gamma_{ij} = \overline{\left(1/\tau_{ii}\right)} = \frac{1}{\Delta\omega_i} \int_{\Delta\omega_i} \frac{1}{\tau_{ij}} d\omega \;;$$

Where v_i is the band-average group velocity, $C_{\omega i}$ is the specific heat per unit frequency in band i, C_i is the band-integrated specific heat, $e_i^{"}$ is the band-integrated energy density per unit solid angle, γ_{ii} is the band-averaged inverse relaxation time for interaction time for interaction of band i with itself, and γ_{ij} is the band-averaged inverse relaxation time for interaction time for interaction of band i and band j. T_{ij} is an interaction temperature between the two bands i and j. In order to satisfy energy conservation, the scattering terms on the right hand side of the pBTE (Eq. 1.47) must cancel out the sum over all bands. This requirement leads to

$$T_{ij} = T_{ji}\text{; and } \int_{\Delta\omega_i} \frac{1}{\tau_{ij}} d\omega = \int_{\Delta\omega_i} \frac{1}{\tau_{ji}} d\omega \tag{1.49}$$

Where i is any frequency band in a given phonon branch and j is any other band, in the same or different branch, with which energy is being exchanged.

The equilibrium energy density is defined as

$$e_i^0 = \frac{1}{4\pi} \int_{4\pi} e_i^{"} d\Omega \; = \frac{1}{4\pi} \int_{T_{ref}}^{T_i} C_i dT = \frac{e_i}{4\pi} \tag{1.50}$$

Where T_i is the temperature associated with the i^{th} band of the branch considered.

To satisfy energy conservation [Narumanchi04], the following condition is also required:

$$\int_{T_{ref}}^{T_{ij}} \left(\frac{C_i}{\Delta\omega_i} + \frac{C_j}{\Delta\omega_j} \right) dT = \int_{T_{ref}}^{T_i} \frac{C_i}{\Delta\omega_i} dT + \int_{T_{ref}}^{T_j} \frac{C_j}{\Delta\omega_j} dT \tag{1.51}$$

This is satisfied for all i and j band combinations (with $i \neq j$) including the optical phonon band. Eq. 1.51 serves as the definition of the interaction temperature T_{ij}. An overall lattice temperature T_L may be defined as follows [Narumanchi04]

$$e_{total} = \int_{T_{ref}}^{T_L} C dT = \int_{T_{ref}}^{T_o} C_o dT + \sum_{i=1}^{N_{bands}-1} \left(\int_{T_{ref}}^{T_i} C_i dT \right) \tag{1.52}$$

Where C is the total specific heat of the solid, and e_{total} energy density.

This model has been checked [Narumanchi04]. It recovers the bulk thermal conductivity of Si at different temperatures [Narumanchi05].

3.4.1b. Gray model

In this approach, all phonons are assumed to have the same group velocity and relax to equilibrium with the same relaxation time τ. The pBTE becomes

$$\frac{\partial e^{"}}{\partial t} + \nabla \left(v \hat{z} e^{"} \right) = \frac{e^0 - e^{"}}{\tau} + q_{vol} \tag{1.53}$$

$$e^0 = \frac{1}{4\pi} \int_{4\pi} e^{"} d\Omega = \frac{1}{4\pi} C \left(T_L - T_{ref} \right) \tag{1.54}$$

Where $e^{"}$ is the energy density per unit solid angle, e^0 is the equilibrium energy density, C is the total specific heat, and T_L is the lattice temperature. The value of v for Si is chosen to be

6400 m/s [Klemens69], while C is 1.66×10^6 J/m^{3}K at 300 K. The relaxation time of τ = 6.28 ps is obtained from the relation $K = 1/3Cv^2\tau$, where K = 142.3 W/mK for Si.

3.4.1c. Semi-Gray model

The next modeling approach is a semi-gray model proposed in [Sverdrup00, Sverdrup01] and it is compared with other approaches in the work of S. V. J. Narumanchi *et al.* [Narumanchi05]. In this approach, the phonons are divided into propagating and reservoir modes. Propagating mode phonons are responsible for transporting energy while the reservoir mode phonons are purely capacitive which means that they are only involved in energy storage. Longitudinal acoustic phonons are considered to be propagating modes, while the transverse acoustic and optical phonons are lumped together in the reservoir mode. The pBTE is written as

$$\frac{\partial e_p^{"}}{\partial t} + \nabla\left(v_p \hat{s} e_p^{"}\right) = \frac{\frac{1}{4\pi} C_P\left(T_L - T_{ref}\right) - e_p^{"}}{\tau} \tag{1.55}$$

$$C_R \frac{\partial\left(T_R - T_{ref}\right)}{\partial t} = \frac{C_R\left(T_L - T_{ref}\right) - C_R\left(T_R - T_{ref}\right)}{\tau} + q_{vol} \tag{1.56}$$

$$C_P\left(T_P - T_{ref}\right) = \int_{4\pi} e_P^{"} d\Omega \tag{1.57}$$

$$T_L = \frac{C_R T_R + C_P T_P}{C_R + C_P} \tag{1.58}$$

Where T_L is the lattice temperature, T_P is the propagating mode phonon temperature, T_R is the reservoir mode phonon temperature, C_P and C_R are the propagating and reservoir mode specific heats, respectively, τ is the relaxation time, v_P is the propagating mode group velocity, $e_P^{"}$ is the propagating mode energy density per unit solid angle (J/m^3 sr). T_L is the overall lattice temperature and is to be interpreted as an average value of the propagating and reservoir mode temperatures as expressed in Eq. 1. 58. The value of C_P is 0.32×10^6 J/m^{3}K, τ is 74.2 ps, v_P is 4240 m/s [S. Sverdrup00, Sverdrup01].

The semi-gray model captures some of the complexities of the phonon dispersion curves at a relatively low cost. Since the reservoir mode equation does not involve direction, it is relatively inexpensive to compute, even if the cost of the propagating mode computation is similar to that of the gray model. However, the value of τ computed using this model is

typically far larger than the value of typical optical-to-acoustic relaxation times, leading to temperature overestimation in FET simulations [Narumanchi03].

3.4.2. The different approaches to solve the pBTE

In the previous subsection, we have presented different models based on the dispersion relationship approximations. In this subsection, we present three models to solve BTE: analytical model, the discrete ordinate method (DOM) and the Monte Carlo (MC) model.

3.4.2a. Analytic model – Kinetic theory of gases

Pioneer works by Klemens [Klemens51], Callaway [Callaway59] and Holland [Holland63] have used analytical solution as they assume a single relaxation time approximation. Within this formalism, boundary and impurity scattering as well as three-phonon processes (Normal and Umklapp) contributions to phonon scattering can be described by a single relaxation time. The resulting models have successfully predicted the bulk thermal conductivity for various semiconductors (Si, Ge, with several dopant concentrations) at low and high temperatures.

These models are derived from the pBTE under the relaxation time approximation (RTA). The steady-state pBTE for the mode *s* (Eq. 2.11) in direction *x* can be reduced to

$$v_x \frac{\partial n_s(\omega)}{\partial x} = \frac{n_s(\omega) - n_{s,T_{scatt}}(\omega)}{\tau_s(\omega)}, \tag{1.59}$$

or to $$n_s(\omega) = n_{s,T_{scatt}}(\omega) + \tau_s(\omega).v_{s,x}(\omega).\frac{\partial n_s(\omega)}{\partial x} \quad . \tag{1.60}$$

By writing $\frac{\partial n_s(\omega)}{\partial x} = \frac{\partial n_s(\omega)}{\partial T} \cdot \frac{\partial T}{\partial x}$, we have

$$n_s(\omega) = n_{s,T_{scatt}}(\omega) + \tau_s(\omega).v_{s,x}(\omega).\frac{\partial n_s(\omega)}{\partial T} \cdot \frac{\partial T}{\partial x} \tag{1.61}.$$

The heat flux is calculated as:

$$j_{s,x} = \int_{\omega} \mathrm{h}\omega.v_x(\omega).n_s(\omega)\,d\omega\,. \tag{1.62}$$

By substituting Eq. 1.61 in Eq. 1.62, the heat flux becomes

$$j_{s,x} = j_{s,x}^{symmetric} + \int_{\omega} \mathrm{h}\omega \cdot v_{s,x}(\omega) \cdot \frac{\partial n_s(\omega)}{\partial T} \cdot d\omega, \tag{1.63}$$

where $j_{s,x}^{symmetric}$ is the symmetric term that includes the equilibrium and symmetric phonon number $n_{s,T_{scatt}}$.

We rewrite here the expression of the phonon number (Eq. 1.38)

$$n(\omega)d\omega = \frac{1}{\exp\left(\frac{\hbar\omega}{k_B T}\right)} \cdot DOS(\omega)d\omega = \iint \frac{1}{\exp\left(\frac{\hbar\omega(\vec{q})}{k_B T}\right)} \cdot \frac{d\vec{q}^3}{(2\pi)^3}.$$

In the spherical coordinates, the term dq^3 is $q^2 dq \sin\theta d\theta d\varphi$, with $\theta = [0, \pi]$, $\varphi = [0, 2\pi]$. By subtitling this term and integrating over θ and φ, and using the Fourier's law $j_x = K \cdot \partial R / \partial x$, we obtain the common thermal conductivity formula as

$$K_s = \sum_{s=LA,TA} \frac{1}{3} \cdot \int_0^G \frac{\hbar\omega_s^2(q)}{k_B T^2} . v_s^2(q) . \tau_s(q) \cdot \frac{\exp(X_s)}{(\exp(X_s) - 1)^2} q^2 \frac{dq}{2\pi^2}. \tag{1.64}$$

3.4.2b. The Discrete Ordinate method

In the phonon transport problem, this numerical tool is frequently used to solve the BTE in a form similar to the radiative heat transfer equation (RTE) which was originally proposed by Majumdar [Majumdar93]. In this method, a set of discrete directions (or ordinates) is chosen and directional fluxes are evaluated for these directions.

A specific spectral intensity $I_{\omega,p}(\vec{r}, \vec{u})$ for phonons which depends on the angular frequency ω, on the polarization branch *p*, on the location $\vec{r}$ and on the direction $\vec{u}$ is introduced. Under the RTA and in steady-state, the pBTE reads [Terris09]

$$\vec{u} \frac{\partial I_{\omega,p}(\vec{r}, \vec{u})}{\partial \vec{r}} + \kappa_{\omega,p} I_{\omega,p}(\vec{r}, \vec{u}) = \kappa_{\omega,p} I_{\omega,p}^0(\vec{r}) \tag{1.65}$$

$\kappa_{\omega,p}$ is an equivalent phonon absorption coefficient which can be expressed in terms of relaxation times $\kappa_{\omega,p} = 1/(\upsilon_{g\,\omega,p} \cdot \tau_{\omega,p})$; and $I_{\omega,p}^0$ is an equilibrium phonon specific intensity which is written as

$$I^0_{\omega,p}(T) = \frac{\omega^2 d\omega}{2\pi^2 v^2_{\varphi\omega,p} v_{g\,\omega,p}} \cdot \frac{\mathrm{h}\omega}{\exp(\mathrm{h}\omega / k_B T - 1)} \cdot \frac{v_{g\,\omega,p}}{4\pi}, \tag{1.66}$$

where $v_{g\,\omega,p}$ is the group velocity and $v_{\varphi\omega,p}$ is the phase velocity.

In complete generality, the reflexion conditions at a point $\vec{r}$ on the wall, in the direction $\vec{u}$ can be written

$$I_{\omega,p}(\vec{r},\vec{u}) = \frac{\rho^d}{\pi} \int_{\vec{u}'\cdot\vec{n}<0} I_{\omega,p}(\vec{r},\vec{u}')\left|\vec{u}'\cdot\vec{n}\right| d\Omega' + \rho^s I_{\omega,p}(\vec{r},\hat{u}), \tag{1.67}$$

where $\hat{u}$ is the incident specular direction relatively to $\vec{u}$ and $\vec{u}'$ is the other incident direction. $d\Omega'$ is an infinitesimal part of the solid angle associated to the direction $\vec{u}'$. ρ^d is the diffusive reflectivity and ρ^s corresponds to specular reflectivity.

In the in-plane configuration, with three direction cosines (μ, η, ξ), the discretized equation in rectangular mesh in the (x, z) plane reads

$$\mu \frac{\partial I_{\omega,p}}{\partial x} + \xi \frac{\partial I_{\omega,p}}{\partial z} + \kappa_{\omega,p} I_{\omega,p} = \kappa_{\omega,p} I^0_{\omega,p} \tag{1.68}$$

To obtain the intensity field, one can use the following iterative integration procedure. The equation is solved by starting from one of the surfaces on which the temperature is imposed. This solution is worked out given the initial temperature field in the medium. It is then solved in the same way starting from the second surface. The new temperature field is calculated at the end of the iteration by expressing the conservation of the heat flux in the steady-regime ($\nabla q = 0$). The integral phonon intensity equation over the frequencies and solid angles is then [Volz09]

$$\int \kappa_\omega I_\omega d\Omega d\omega = \int \kappa_\omega I^0_\omega d\Omega \tag{1.69}$$

At each point, the temperature satisfies the previous relationship. The iterative process is continued until both the intensity and temperature fields converge, in accordance with a previously specified criterion [Volz09].

Majumdar [Majumdar93] used this method to study the steady-state heat transport in diamond thin films. By including the quadratic dispersion for Si (Eq. 1.35) Terris *et al.* [Terris09-1, Terris09-2] obtained the thermal conductivity of Si bulk and of Si nanowires in good agreement with the experimental data.

3.4.2c. Monte Carlo method

As described in subsection 2.3, as in most statistical techniques, the accuracy of the results is related number of particles in the sample. This method (MC) is widely used to solve the pBTE without any approximation [Mazumder01, Lacroix05, Lacroix06, Wong11, Terris01-1, Hamzeh11]. The results of these studies that use these techniques are very close to the experimental data.

Lacroix and co-workers [Lacroix05] showed that this model can reproduce all regimes of phonon transport (Fig. 1.10a). By taking into account the boundary scattering, the conductivities in nanowires obtained by this method are very close to the experimental ones (Fig. 1.10b) [Lacroix06].

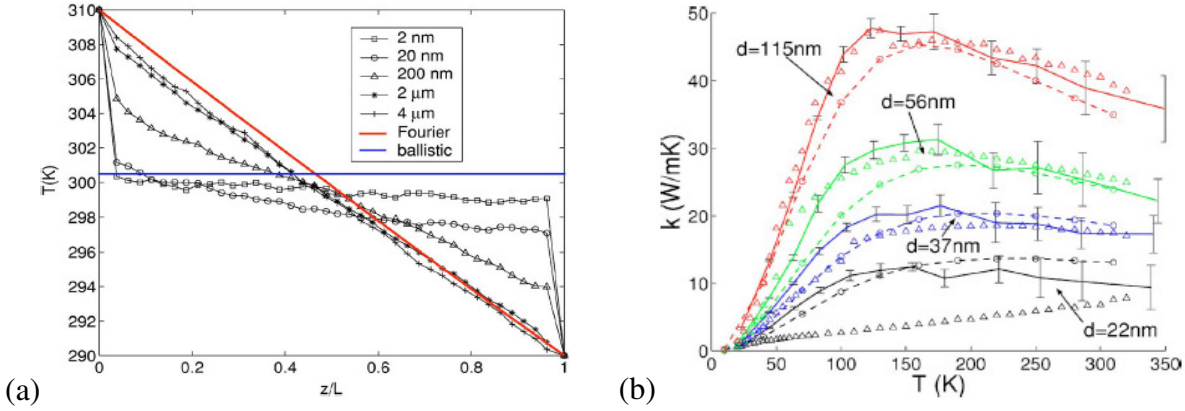

Fig. 1.10. (a) Steady-state temperature for Si, influence of the slab thickness; comparison to the analytical solution in the diffusive and ballistic limits (taken from [Lacroix05]). (b) Nanowire thermal conductivity; comparison between MC simulations - solid lines, experimental data (taken from [Lacroix06]).

Using this method, H. Hamzeh and F. Aniel [Hamzeh11] calculated the scattering rates for all individual three-phonon processes with only one adjustable parameter. They also studied the zone-centre LO lifetimes and the decay dynamics, the distributions evolution with time in GaAs and InP.

4. COUPLED ELECTRON-PHONON TRANSPORT IN SI-FET AND SI-MOSFET

As mentioned at the beginning of this chapter, electro-thermal simulation of sub-micron electron devices is of great interest for both academia and industry, due to the fact that self-

heating may cause device performance degradation in submicron devices [Ni12]. When the transistor dimensions become sub-micron, the thermal model should be carefully chosen.

As the MC method can capture the complexities of electron transport in real device and gives electrical characteristics extremely close to experimental results, we review the coupled electron-phonon transport simulation of Si transistors by using the MC method for electrons and various thermal models.

Sadi *et al*. used a 2D electron Monte Carlo (eMC) simulation coupled with a 2D solution of the heat diffusion equation to study the electro-thermal phenomena in SOIFETs and in Silicon-Germanium-on-Insulator metal-oxide FETs [Sadi10]. They highlighted the electron velocity and the drain current degradations in a 0.1µm-long-channel transistor. Then, the coupled simulations are extended to study the self-heating effect in InGaAs channel high-electron mobility transistor (HEMT) at nanoscale by the group of T. Sadi and J-L. Thobel [Sadi12].

Ravela, Vasileska and Goodnick [Raleva08, Vasileska09, Vasileska10, Raleva12] coupled eMC simulation with transport equations for optical and acoustic energy transfer derived from the BTE which has been developed by [Lai96]. They defined three temperatures in the device: electron temperature T_e, optical temperature T_O and acoustic temperature T_A that was assumed to be the lattice temperature T_L . A constant energy transfer rate for the optical-acoustic phonon of 10 ps was used. The temperature profile was changed when different boundary conditions were applied (Neumann/Dirichlet). They showed that the drain current is degraded by the heating. Furthermore, it was obtained that this degradation depends on the thermal conductivity of thin Si film that was introduced analytically in the model [Vasileska10]. Although they solved the equations for optical and acoustic energy transfer derived from pBTE, the transfer model used was too simplistic model which might not be able to capture detailed physics of phonon transport in sub-micron devices [Ni12]. They studied the self-heating with channel lengths devices in the range from 25 nm to 180 nm. Hatakeyama and Fushinobu [Hatakeyma08] employed this model to study the thermal cross-talk between the nMOS and pMOS FETs that were set side-by-side to design a CMOS device. The channel length of the two MOSFETs was 90 nm while their entire length is 680 nm.

More complex, Kamakura *et al*. [Kamakura10] coupled the MC method to solve the transient BTE for both electrons and phonons. They simulated a simple 1D *n-i-n* Si device.

The contribution of optical phonons was neglected, while the heating modes can only be dissipated through the conversion into acoustic modes with a relaxation time of 10 ps. The acoustic phonons were approximated by the Debye approximation with a constant velocity of $v_{ac} = 5.9$ km/s. The solution of transient pBTE was validated by calcultating the thermal conductivity obtained for some temperatures. The temperatures of both acoustic and optical modes were estimated.

To build a better thermal transport model in submicron devices, it is necessary to take into account the phonon dispersion. Pop *et al*. [Pop04] proposed an isotropic and quadratic relationship for Si in the [100] direction. The frequency-dependent net phonon generation was exploited [Pop05, Pop10] by using the eMC simulation. That is an important point to study the heat transport at the submicron scale.

Rowlette and Goodson [Rowlette08] coupled the eMC model of Pop et al. [Pop04] with the split-flux model for phonon transport to perform a self-consistent simulation of non-equilibrium transport in Si-FETs. Their coupled simulation begun with an isothermal eMC simulation at 300 K, and then the net phonon generation rates as a function of position and phonon frequency were collected and used as an input for the split-flux phonon transport model. The solution gives an updated distribution of phonons at each spatial position. The simulator iterates until satisfactory convergence is reached. The model was used to study a 1D 20 nm-long-n-region in a n^+-n-n^+ Si diode. They emphasized the role of g-LO and the phonon bottleneck effect.

More recently, Ni *et al*. [Ni12] estimated the hotspot temperature in a MOSFET device by using an anisotropic relaxation time in a pBTE solver. The phonon generation spectrum obtained via eMC simulation was incorporated into the anisotropic relaxation time pBTE model of [Ni09]. The phonon dispersion includes six branches (TA1, TA2, LA, TO1, TO2 and LO). A fully anisotropic Brillouin zone is also taken into account. However, the computational cost of this model is expensive [Ni09].

5. PURPOSE OF THIS WORK

This chapter highlighted the importance of studying the self-heating of nano-scale devices. Various models for electron and phonon transports were presented. The BTE appears of great interests for studying non-equilibrium thermal effects at the nanoscale.

In Chapter 2, the numerical pBTE solver developed in this thesis is described in detail and validated against experimental results. Next in Chapter 3, the coupling with this new pBTE solver and our eMC (MONACO) simulator will be presented and discussed. Fully self-consistent Electro-thermal simulations in nano-scale DG-MOSFET were performed and deeply investigated in terms of microscopic (non-equilibrium transport) and macroscopic effects (current degradation).

Chapter II: Phonon transport models and the thermal conductivity in nanostructures

1. INTRODUCTION

In this chapter, we will summarize the basic notions related to the phonon heat conduction in a crystalline material. The phonon dispersion and phonon scattering mechanisms will be described. We will focus on the particular case of Silicon (Si). By using an isotropic and quadratic dispersion approximation, a new set of scattering parameters will be introduced and implemented to reproduce the thermal conductivity of bulk Si.

In equilibrium conditions (300K), the quasi-equilibrium heat conduction is principally carried by acoustic phonons in a sample where a small temperature gradient is forced. In out of equilibrium, a situation that occurs in conventional operation of transistors, the decay of hot optical phonons into acoustic phonons plays an important role too. A model of this decay mechanism is proposed and used to simulate realistic devices. As mentioned in the first chapter, at the micro- and nano-scales, the phonon transport can be well described by the BTE. An analytic model is presented to adjust the scattering rates and to evaluate the dependence of the thermal conductivity on the size and the geometry of the sample. This model is also used to interpret recent measurements in silicon nanowires.

In the third part of this chapter, we present a numerical algorithm developed in the present work and specially dedicated to directly solve the steady-state BTE under the relaxation time approximation considering the quadratic phonon dispersion. The main advantage of this method is its ability to point out the local thermodynamics of phonons along the sample. After having validated the model for Si bulk, different phonon transport regimes are investigated, from the diffusive regime to the ballistic regime.

2. SCATTERING MECHANISMS

Phonons in a crystal are scattered according to a variety of mechanisms, including three-phonon interactions, scattering on lattice imperfections as vacancies and impurities, and boundary scattering [Murthy05]. Scattering mechanisms are either elastic when the energy (or frequency) of the phonon remains unchanged, or inelastic when the energy (or frequency) are changed during the scattering event. Scattering due to impurities are considered to be elastic [Klemens58]. Boundary scattering is an important type of scattering encountered in micro- and nano-structures that induces phonon reflection at sample boundaries with a fraction of

specular/diffusive reflections. The two main types of inelastic scattering processes for phonons are normal (N) and Umklapp (U) phonon-phonon scattering processes that are described below. The decay of optical phonons into acoustic modes is also included.

2.1. Three-phonon scattering for acoustic phonon

The three-phonon scattering processes are related to the anharmonic nature of the interatomic forces and the discrete nature of the lattice structure. Phonon-phonon scattering involving four or more phonons is important only at temperature much higher than the Debye temperature (645K for silicon) [Murthy05] and are not considered here since 645K is higher than the operating temperature of most electronic devices.

Both Normal (N) and Umklapp (U) processes are governed by energy and momentum conservation rules

$$\omega+\omega' \leftrightarrow \omega''\text{(Normal and Umklapp)} \tag{2.1a}$$

$$\vec{q}+\vec{q}' \leftrightarrow \vec{q}''\text{(Normal)} \tag{2.1b}$$

$$\vec{q}+\vec{q}' \leftrightarrow \vec{q}''+\vec{G}\text{(Umklapp)} \tag{2.1c}$$

Where ω, ω' and ω'' are the angular frequencies of the interacting phonons, $\vec{q}$, $\vec{q}'$ and $\vec{q}''$ are their wave vectors and $\vec{G}$ is a reciprocal lattice vector.

In normal processes the total wave vector is conserved (Eq. 2.1b). In Umklapp processes (or U processes) that is not the case. A typical Umklapp process is shown in Fig. 2.1 for a linear lattice. After a U process two phonons, both having a positive q_x, may generate a phonon with a negative q_x [Kittel71].

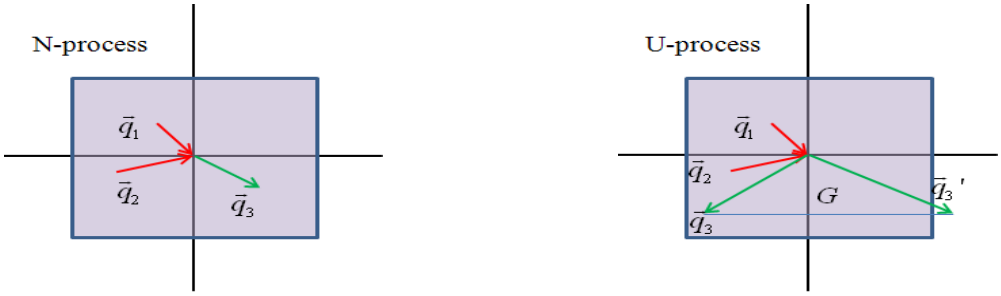

Fig.2.1. Illustrations of Normal and Umklapp phonon–phonon scattering mechanism.

N processes do not impact the heat transfer because they conserve the momentum. However, they can change the frequency distribution of phonons, and hence indirectly affect other scattering processes that depend on frequency. U scattering do not conserve the crystal momentum directly, but must satisfy Eq. 2.1c. U processes create a resistance to heat transfer and must be modeled carefully.

Some three-phonon interactions are listed in the Table 2.1 [Mittal10].

LA	LO	TA	TO
LA +TA↔LA LA+TA↔LO LA+TA↔TO LA+LA↔LO LA+TA↔TO	LO↔LA+TA LO↔LA+LA LO↔TA+LA	TA+TA↔LA TA+LA↔LA TA+LA↔LO TA+LA↔TO	TO↔LA+TA TO↔LA+LA TO↔TA+LA

Table 2.1. Main three-phonon scattering mechanism [Mittal10].

Using a perturbative approach in combination with calibration to experimental data, Holland [Holland63] developed frequency and temperature dependent expressions for the relaxation time of scattering for LA and TA phonons as

$$\tau_{NU} = B_L \omega^2 T^3 \left(\mathrm{LA}, Normal + Umklapp\right) \tag{2.2a}$$

$$\tau_N^{-1} = B_{TN} \omega T^4 \left(\mathrm{TA}, Normal\right) \tag{2.2b}$$

$$\tau_U^{-1} = \begin{cases} 0 & \left(\mathrm{TA},\ Normal\ for\ \omega < \omega_{1/2}\right) \\ B_{TU}\omega^2 / \sinh\left(\dfrac{\hbar\omega}{k_B T}\right) & \left(\mathrm{TA},\ Umklapp\ for\ \omega > \omega_{1/2}\right), \end{cases} \tag{2.2c}$$

where $\omega_{1/2}$ is the frequency corresponding to $q/q_{max} = 0.5$, and B_{L}, B_{TN} and B_{TU} are empirical parameters [Holland63], that need to be calibrated against experimental data. Holland made two important assumptions for calculating these time-scales: (1) only high frequency TA phonons undergo U processes and (2) LA phonons do not undergo U processes at all. Despite these strong assumptions, the expressions provided by Holland continue to be popular because of their simplicity and the ease of their implementation. It has been checked by A. Mittal [Mittal10] from detailed MC simulation that these parameters give reasonable results.

By using this model with a linear dispersion, Holland [Holland63] obtained the thermal conductivity of Si bulk in good agreement with the experimental one. The linear dispersion is expressed as [Holland63]

$$\omega_s(q) = v_{g,s} \cdot q \quad \text{if} \quad q \le \frac{G}{2} \tag{2.3a}$$

$$\omega_S(q) = v_{gs} \cdot \frac{G}{2} + v'_{g,s} \cdot \left(q - \frac{G}{2} \right) \quad \text{if} \quad \frac{G}{2} < q \le G\,. \tag{2.3b}$$

For $q = G/2$, the frequency values are called $\omega_{cut,S}$ (with s = LA,TA). The parameters of Holland's dispersion are reported in Table 2.2.

Model	v_T	v_L	v_S	ω_{cutT}	ω_{cutL}
Holland (a)	5860	8480	6400	2.375×10^{13}	4.618×10^{13}
(b)	2000	4240	6400	2.771×10^{13}	7.521×10^{13}

Table 2.2. Parameters of the dispersion model: (a) for $\omega \le \omega_{cutS}$, (b) for $\omega > \omega_{cutS}$. Velocity is in [ms^{-1}], frequency in [$rads^{-1}$]. [Holland63]

2.2. Relaxation time of optical phonon

The lifetime, as well as the relaxation time, of LO and TO (LTO) modes have been calculated and measured from the Raman spectra [Menéndez84] [Lang99]. The calculated and Raman linewidth which have been compared in [Menéndez84], [Lang99], are reported in Fig. 2.2.

The frequency at the half maximum is

$$\Gamma\left(cm^{-1}\right) = \frac{FWHM\left(cm^{-1}\right)}{2}\,. \tag{2.4}$$

The mean lifetime of optical phonons can be estimated as

$$\tau = \frac{1}{\Gamma\left(rad/s\right)} = \frac{1}{2\pi c \times \Gamma\left(cm^{-1}\right)}\,. \tag{2.5}$$

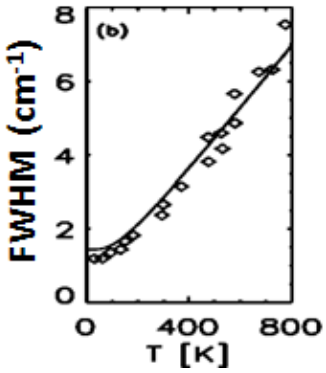

Fig. 2.2. Raman linewidth (full width at half maximum – FWHM) in Si, taken from [Lang99]. The diamond symbols are experimental data after [Menéndez84], the continuous curve is the calculated result.

At 300 K, the lifetime of optical phonon is estimated to be 3.5 ps, while at 400 K, its value drops to about 2.7 ps. By using molecular dynamic and lattice dynamic simulations, and taking into account the normal mode decay, A.S. Henry and G. Chen have found that the relaxation time of these phonon modes varies very weakly, in the order of some picoseconds. In addition, the group velocity of LTO modes is noticeably smaller than the one of acoustic phonons. Therefore, we use a relaxation time of 3.5 ps for the LTO modes in this work.

2.3. Phonon mode coupling - Optical phonon decay into acoustic phonon

The anharmonic decay of phonons into vibrations of lower frequency is a crucial mechanism for energy relaxation in semiconductors as it controls the formation and time evolution of non-equilibrium (hot) phonon populations, which are emitted by high-density hot carriers when they decay towards their ground state [Debernardi95]. Based on the simple lattice model consisting of a linear chain of atoms, lifetimes of optical phonons were first considered by Klemens[Klemens66]. Klemens assumed that the optical phonons decay into a pair of acoustic phonons on the same branch but with opposite momenta. In contrast to Klemens, based on DFT calculation, Debernardi et al [Debernardi95] showed that in silicon the zone-center optical phonons mainly decay into pairs of acoustic phonons involving one phonon of the longitudinal branch and another one of the transverse branch.

If only three-phonon processes are considered, energy and momentum must be conserved. That means $\vec{q}_0 = \vec{q}_1 + \vec{q}_2 + \vec{G}$ and $\omega_0 = \omega_1 + \omega_2$. The inverse lifetime Γ of the LO and TO modes (LTO) writes as [Klemens66] [Debernardi95]

$$\Gamma = \frac{\pi\hbar}{16N^2M^3} \sum_{\vec{q}_1,\vec{q}_2,s_1,s_2} \left(\frac{\partial^3 E}{\partial u_{LTO}(\vec{q}_0)\partial u_{s_1}(\vec{q}_1)\partial u_{s_2}(\vec{q}_2)} \right)^2 \times \frac{n_{s_1}(\vec{q}_1) + n_{s_2}(\vec{q}_2) + 1}{\omega_{s_1}(\vec{q}_1)\omega_{s_2}(\vec{q}_2)\omega_{LTO}(\vec{q})} \times \delta\left(\omega_{LTO}(\vec{q}) - \omega_{s_1}(\vec{q}_1) - \omega_{s_2}(\vec{q}_2)\right), \tag{2.6}$$

where N is the number of unit cells in the crystal, M is the atomic mass, ω_s are the phonon frequencies, n is the thermal occupation numbers, s indicates the phonon branch (s = LA and TA in bulk semiconductors), E is the crystal energy, and $u_s(\vec{q})$ is the amplitude of the s phonon of wave vector $\vec{q}$.

Rowlette *et al*. [Rowlette08] made the calculation by using the full phonon dispersion and assuming that the third-order matrix elements are equal to a constant deformation potential U_0 which is fitted to the Raman line width data of [Menendez84]. The expression for the transition rate in this case is given by

$$\Gamma \propto \sum_{\vec{q}_1,\vec{q}_2,s_1,s_2} \left(U_0 \begin{pmatrix} \vec{q}_0, & \vec{q}_1, & \vec{q}_2 \\ s_0, & s_1, & s_2 \end{pmatrix} \right)^2 \times \frac{n_{s_1}(\vec{q}_1) + n_{s_2}(\vec{q}_2) + 1}{\omega_{s_1}(\vec{q}_1)\omega_{s_2}(\vec{q}_2)\omega_{LTO}(\vec{q})} \times \delta\left(\omega_{LTO}(\vec{q}) - \omega_{s_1}(\vec{q}_1) - \omega_{s_2}(\vec{q}_2)\right). \tag{2.7}$$

To be consistent with the isotropic phonon dispersion considered in this work (Eq.1.35, chapter 1) which is more complex than that used by Klemens but simpler than those of Rowlette, Eq. 2.7 is computed with only two branches LA and TA. Only third-order processes in which the initial optical phonons decay into two lower energy modes are considered.

Thus, in this work, the density $g_2(\omega,\omega_{LTO}-\omega)$ of final states for pairs of phonons which conserve both energy ($\omega_{s_0}(\vec{q}_0) = \omega_{s_1}(\vec{q}_1) + \omega_{s_2}(\vec{q}_2)$) and crystal momenta ($\vec{q}_0 = \vec{q}_1 + \vec{q}_2 + \vec{G}$) for an optical phonon with initial wave vector $\vec{q}_0$ and branch index s_0 were calculated considering a parabolic dispersion. We restrict our calculations to normal process, i.e. $\vec{G} = 0$. The results for LO phonons with the initial wave vector $\vec{q}_0 = G \times [0, 0, \alpha]$, where α = 0, 0.3, 0.5, 0.7 and 1.0 are shown in Fig. 2.3. The TA+LA decay channel is illustrated by the green curve, the LA+LA one by the red curve.

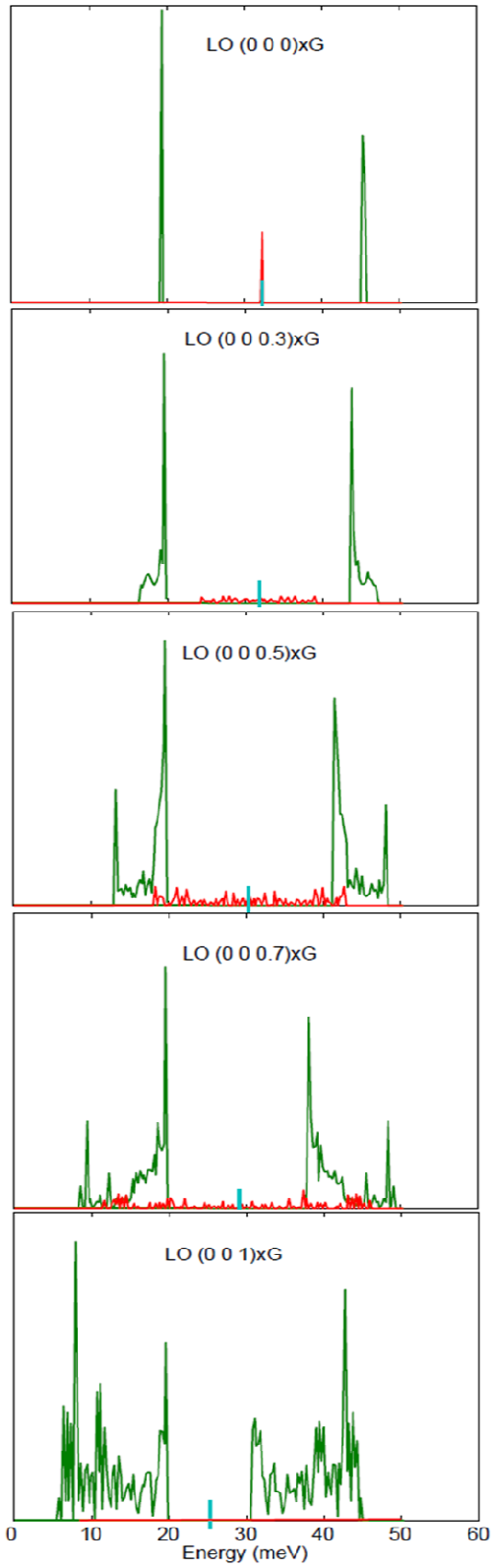

Fig. 2.3. $g_2(E,E_0\text{-}E)$ for an LO phonon of initial energy and wave vector at the point $G\times[0,0,\alpha]$, where $\alpha = 0$, 0.3, 0.5, 0.7 and 1, decaying into two lower energy phonons.

$g_2(\omega,\omega_{LTO}-\omega)$ spectra are always symmetric with respect to $\omega=\omega_{LTO}/2$ (in order to achieve energy conservation). The ω_0 value in each case is indicated by a straight line. As expected, the Klemens channel, presented by a central peak is relatively weak. These results are consistent with the DFT calculation of Debernardi et al. [Debernardi95] and the work of Rowlette et al. [Rowlette08].

Then, the total phonon density of the final state considering the anharmonic LTO-phonons decay is calculated by computing the decay of 3000 optical phonons uniformly distributed along the optical branches. The frequency final state spectrum, i.e. the probability per unit time that LTO phonon decays into one mode of given frequency ω and one of frequency $\omega_{LTO}-\omega$, is obtained by restricting the sum over branch s and $\vec{q}$ in Eq. 2.7 to those values for which $\omega_s(\vec{q})=\omega$, as defined in [Debernardi95]. The resulting normalized distribution of LA and TA modes generated by optical phonon decay are plotted in Fig. 2.4a. We see two peaks in Fig. 2.4a: one around 20 meV which belongs to the TA branch and one around 45 meV which belongs to the LA branch. This final state spectrum is in agreement with the DFT calculation in [Debernardi95] and [Aksamija10]. It should be noted that we do not considered phonons in the TA mode in the energy range from 20 meV to 30 meV. Thus, the probability of LA mode at 20 meV differs. However, this optical decay calculation considering a parabolic dispersion and a spherical Brillouin zone can be used to conserve energy in the phonon system.

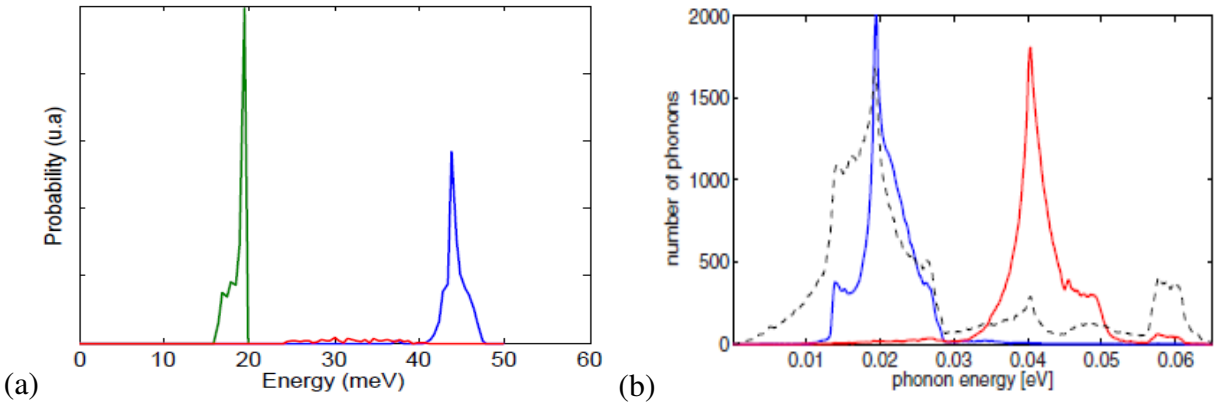

Fig. 2.4. Energy distribution of the phonons generated by the anharmonic decay of g-type longitudinal optical by using a) our calculation: LA-blue curve; TA green curves; LA+TA red curve b) results from [Aksamija10]: LA blue curve; TA red curve; dot full phonon dispersion.

2.4. Impurity scattering

The impact of impurity scattering on the thermal conductivity has been carefully studied by Fortier and Suzuki for low Phosphorus doping [Fortier76] and by Asheghi et al. [Asheghi02] for high doping. They measured the thermal conductivity of 3 μm-thick films in the temperature range of 15-300 K. By varying the doping concentration, the thermal conductivity of this film is reduced. This effect is more important at low temperature, in particular below 100 K.

The mass difference δM between an impurity and a crystal atom of mass M and the interatomic difference of distance δR between the defect-crystal atom distance and the atom-atom distance are involved in the impurity-phonon scattering mechanism. The imperfections and unintentional impurities are modeled in doped samples by a term $A_x\omega^4$ [Asheghi02]. The corresponding scattering rate is [Klemens55, Asheghi02]

$$\tau_{impurity}^{-1} = \left(A_{\delta M} + A_{\delta R} + A_x\right) \cdot \omega^4, \tag{2.8}$$

where ω is the angular frequency in *rad* s^{-1}.

The average sound velocity is defined as $\frac{1}{v_s} = \frac{1}{3} \cdot \left(\frac{1}{v_L} + \frac{2}{v_T} \right)$, where v_L and v_T are the velocities of longitudinal and transverse modes, respectively.

By evaluating the reduction in thermal conductivity near the maximum of conductivity, Asheghi *et al.* [Asheghi02] proposed the three parameters of doping scattering (see Eq. 2.8) for Boron (B) and Phosphorus (P) are reported in Table 2.3.

Doping concentration (cm^{-3})	A_x ($x10^{45}$ s^3)	$A_{\delta R}$ ($x10^{45}$ s^3)	$A_{\delta M}$ ($x10^{45}$ s^3)
$1.0x10^{17}$ (P)	0	0.0015	0.00014
$1.0x10^{18}$ (P)	1.17	0.015	0.0014
$3.0x10^{19}$ (P)	2.35	0.45	0.042
$1.0x10^{17}$ (B)	0	0.025	0.005
$1.0x10^{18}$ (B)	1.76	0.25	0.05
$1.0x10^{19}$ (B)	2.54	25.4	0.50
$1.0x10^{18}$ (P) bulk	11.17	0.015	0.0014

Table 2.3. Values of three parameters A_x, $A_{\delta R}$ and $A_{\delta M}$ obtained by Asheghi*et al.* [Asheghi02]

Here, we suppose that for each doping type (P or B) the A_x varies linearly with doping density, while $A_{\delta R}$ and $A_{\delta M}$ are proportional to the doping density as indicated in Table 2.4.

Doping type (cm^{-3})	A_x ($x10^{45}$ s^3)	$A_{\delta R}$ ($x10^{45}$ s^3)	$A_{\delta M}$ ($x10^{45}$ s^3)
P	$n_P < 10^{18}\ cm^{-3}:\ A_x^P = 0$ $n_P \geq 10^{18}\ cm^{-3}:\ A_x^P = 1.17 + \frac{n_P}{10^{18}} \times 0.118$	$A_{\delta R}^P = \frac{n_P}{10^{17}} \times 0.0015$	$A_{\delta M}^P = \frac{n_P}{10^{17}} \times 0.00014$
B	$n_B < 10^{18}\ cm^{-3}:\ A_x^B = 0$ $n_B \geq 10^{18}\ cm^{-3}:\ A_x^B = 1.76 + \frac{n_B}{10^{18}} \times 0.078$	$A_{\delta R}^B = \frac{n_B}{10^{17}} \times 0.025$	$A_{\delta R}^B = \frac{n_P}{10^{17}} \times 0.005$

Table 2.4. Doping density-dependence of impurity scattering parameters A_x, $A_{\delta R}$ and $A_{\delta M}$ assumed in this work.

2.5. Boundary and roughness scattering

2.5.1 Boundary scattering in Si bulk

Boundary scattering is important at low temperature due to the "freezing out" of three-phonon processes. The corresponding increase in the phonon mean free path implies that interaction with the boundaries becomes the dominant scattering mechanism at temperatures below 50 K for silicon [Ni09]. Holland modelled the relaxation time of this mechanism in the form [Holland63]

$$\frac{1}{\tau_b} = \frac{v_g}{LF},\ L = \frac{2}{\sqrt{\pi}}\sqrt{l_1 l_2}\ , \tag{2.9}$$

where $l_1 l_2$ is the sample cross section, F is a factor representing the correction due to both the smoothness of the surface and the finite length/thickness ratio of the sample.

2.5.2 Boundary and roughness scattering in nano-structure

It's well known that the roughness of interfaces is an important element which influences strongly the thermal conductivity in two- and one-dimensional structures. Generally, the surface of bulk materials is very rough and the boundary scattering is considered to be

completely diffusive. However, at other interfaces, as in nanostructures, the surface roughness may be much smaller, and specular scattering may take place [Baillis09].

Each boundary is assumed to be rough with a deviation from an ideal surface characterized by surface-roughness height $z(\vec{r})$. Goodnick *et al.* demonstrated experimentally by using high-resolution transmission electron microscopy that the surface roughness $z(\vec{r})$ is a random variable with a Gaussian distribution so that the average value $\langle z \rangle = 0$ and $\langle z^2 \rangle = \Delta^2$, where Δ is the root mean square height of the surface roughness. They showed that for the interface Si(100) –SiO_2, Δ ranges from 1.33 to 50 Å [Goodnick87]. Recently, Park et al. have measured the average roughness of single-crystal VLS-grown (vapor-liquid-solid) Si nanowires in the <111> direction, which is from 2Å to 36Å [Park11].

When a particle of wave vector $\vec{q}$ hits a rough surface with the incident angle θ_B, the reflected wave contains a specular component and a diffusive component. In the case of weak correlation of autocovariance function of Si surface, the surface roughness scattering can be effectively characterized by a specularity parameter $p(\vec{q})$ [Soffer67] with dependence as

$$p(\vec{q}) = \exp\left(-4q^2\Delta^2 \cos^2 \theta_B\right). \tag{2.10}$$

The specular parameter $p(\vec{q})$ is used to model the different values of the thermal conductivity measured experimentally. If the interface Si-SiO_2 is perfect (Δ=0), i.e. $p(\vec{q})$=1, each collision between phonon and boundary will be specular. Hence, the transport is the same as in bulk material. In the case of very rough Si-SiO_2 interface, $p(\vec{q})$ tends to 0, the phonon-boundary scattering is completely diffusive.

The phonon-boundary scattering rate can be written in the following form [Berman1953]

$$\tau_{s,B}(\vec{q}) = \min\left\{\frac{L_i}{v_{s,i}(\vec{q})}.\frac{1}{F(\vec{q})}\right\}, \tag{2.11}$$

where *i* refers to the direction (*x*, *y* or *z*) and the form factor $F(\vec{q})$ is

$$\frac{1}{F(\vec{q})} = \frac{1+p(\vec{q})}{1-p(\vec{q})} \tag{2.12}$$

We calculate the specular parameter p for LA and TA modes in a typical film of 20 nm thickness and roughness of $\Delta = 5$ Å. The evolution of this parameter as a function of the frequency ω is shown in Fig. 2.5.

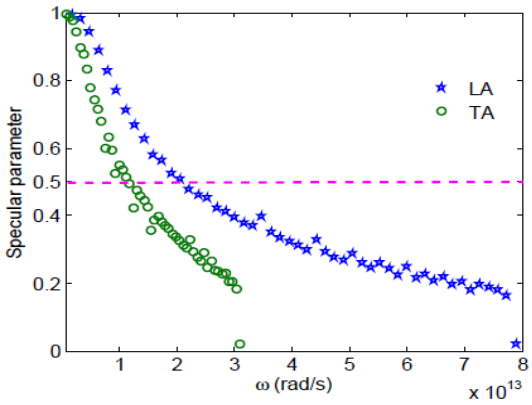

Fig.2.5. Specular parameter vs. angular frequency for LA and TA modes in an Si film of thickness 20 nm and roughness 5 Å.

For both modes, the phonon-boundary scattering part is rather specular for $|\vec{q}|<2.5\times10^{9}\ \mathrm{m}^{-1}$. This corresponds to ω_{TA} ; $1.17\times10^{13}\ rad/s$ and ω_{LA} ; $2.05\times10^{13}\ rad/s$). At high $\vec{q}$, diffusive scattering is dominant for both LA and TA modes.

The specular parameter $\overline{p}_s$ for the LA and TA branches with various Δ value, is averaged over all phonon wave vectors as

$$\overline{p}_s = \frac{\int p(\vec{q})\,N\left(\omega_s(\vec{q})\right)d\vec{q}^{\,3}}{\int N\left(\omega_s(\vec{q})\right)d\vec{q}^{\,3}}, \tag{2.13}$$

where N is the equilibrium Bose-Einstein phonon distribution function. $\overline{p}_s$ depends on the temperature and Δ. Some results are plotted as a function of the temperature in Fig. 2.6a and as a function of Δ in Fig. 2.6b.

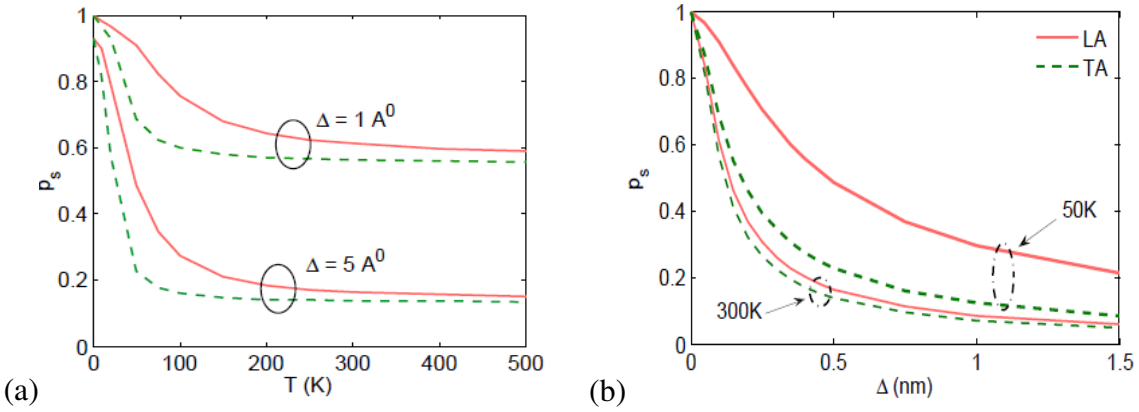

Fig. 2.6. Average specular parameter for LA (solid red line) and TA (dashed green line). (a) Temperature dependence of the parameters $\overline{p}_s$ for surface roughness Δ of 1 A and 5 A. (b) Roughness surface dependence of $\overline{p}_s$ at 300 K and 50 K.

The TA phonon scattering is more diffusive than the LA scattering. As expected, the diffusive scattering probability is more important in rough films, i.e. when Δ is greater. In addition, the specular-to-diffusive transition occurs at lower temperature for TA modes than for the LA branch. The temperature dependence of the phonon population explains this phenomenon. The frequency of TA modes is almost constant at large *q*, where the diffusive scattering occurs; in contrast, for LA modes, the frequency increases with *q* (see Fig. 1.7-chapter I). In addition, as seen in Fig. 2.6a, the higher the temperature is, the more diffusive is the phonon-boundary scattering. Above discussed average specular parameters are in good agreement with the work of Aksamija and Knezevic [Aksamija10-1] and that of Duda *et al.* [Duda00].

3. ANALYTIC MODEL OF THERMAL CONDUCTIVITY

In the relaxation time approximation (RTA), the stationary Boltzmann Transport equation (BTE) for the mode *s* (Eq. 2.23) in direction *x* can be reduced to

$$v_x \frac{\partial n_s(\omega)}{\partial x} = \frac{n_s(\omega) - n_{s,T_{scatt}}(\omega)}{\tau_s(\omega)}, \tag{2.14}$$

where τ_s is the overall scattering time of the phonon due to all scattering processes and is calculated by the Mathiessen's rule

$$\frac{1}{\tau_s}=\frac{1}{\tau_{s,N}}+\frac{1}{\tau_{s,U}}+\frac{1}{\tau_{s,I}}+\frac{1}{\tau_{s,B}}. \tag{2.15}$$

Where $\tau_{s,I}$ is the phonon-impurity interaction frequency and $\tau_{s,B}$ is the phonon-boundary interaction one.

At equilibrium, the number of phonon is

$$n(\omega)d\omega=\frac{1}{\exp\left(\frac{\hbar\omega}{k_BT}\right)}\cdot DOS(\omega)d\omega=\iiint_{\omega<\omega(\vec{q})<\omega+d\omega}\frac{1}{\exp\left(\frac{\hbar\omega(\vec{q})}{k_BT}\right)}\cdot\frac{d\vec{q}^3}{(2\pi)^3}. \tag{2.16}$$

In spherical coordinates, the thermal conductivity formula can be written as

$$K_s=\sum_{s=LA,TA}\frac{1}{3}\cdot\int_0^G\frac{\hbar\omega_s^2(q)}{k_BT^2}.v_s^2(q).\tau_s(q)\cdot\frac{\exp(X_s)}{(\exp(X_s)-1)^2}q^2\frac{dq}{2\pi^2}. \tag{2.17}$$

3.1. Adjustment of scattering rate for bulk Si

The Holland's model [Holland63] gives thermal conductivities of bulk Si in a good agreement with experimental data. However this model was developed for a linear phonon dispersion. When using a quadratic dispersion, the resulting conductivity is significantly shifted relatively to the experimental curve. Terris *et al.* [Terris09] have modified the Holland's scattering parameter, B_L and B_{TU} to fit better the experimental conductivity as shown in Fig. 2.7, but they still over-estimate the conductivity [Lacroix09]. In our scattering model, we take the same B_L, B_{TU} as in Terris's model (see Table 2.5, in green); the parameter B_T and the geometric factor F are modified (see Table 2.5, in red).

Model	τ_B	τ_I	$\tau_{N,T}$ (B_T)	$\tau_{U,T}$ (B_{TU})	$\tau_{NU,L}$ (B_L)
Holland (a)	$L=7.16\times10^{-3}$m	A = 1.32 $\times10^{-45}$s^3	9.3×10^{-13}K^{-3}	0	2×10^{-24}sK^{-3}
(b)	$F=0.8$		0	5.5×10^{-18}s	-
Terris (a)	$L=7.16\times10^{-3}$m		9.3×10^{-13}K^{-3}	0	1.18×10^{-24}sK^{-3}
(b)	F = 0.8		0	2.89×10^{-18}s	-
Our model (a)	$L=7.16\times10^{-3}$m		10.5×10^{-13}K^{-3}	0	1.18×10^{-24}sK^{-3}
(b)	F=0.68		0	2.89×10^{-18}s	-

Table 2.5. Relaxation time parameters: (a) for $\omega\le\omega_{cutS}$, (b) for $\omega>\omega_{cutS}$. (F is defined in Eq. 2.6)

We compared the thermal conductivity obtained by combining different sets of scattering parameters with the quadratic dispersion. The results are shown in Fig. 2.7. The thermal conductivity calculated using our set of scattering parameters and the quadratic dispersion fits very well the experimental curve, not only at high temperature, but also at very low temperature. In this study, we use this set of parameters for Si.

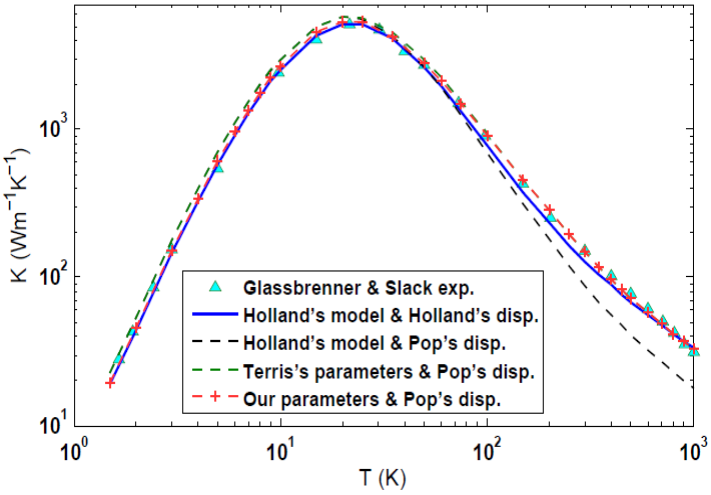

Fig. 2.7. Influence of the dispersion and time relaxation on the silicon bulk thermal conductivity calculation. Triangles are experimental data after [Glassbrenner64] full blue line is for Holland's scattering model with Holland's dispersion, black dashed line for Holland's scattering model with Pop's dispersion, green dashed line for Terris's scattering model with Pop's dispersion, red dashed line for our scattering model with Pop's dispersion.

Finally, the intrinsic (phonon-phonon) and total relaxation time in this work, and the intrinsic and total mean free path corresponding to the new set of scattering parameters are displayed in Fig. 2.8.

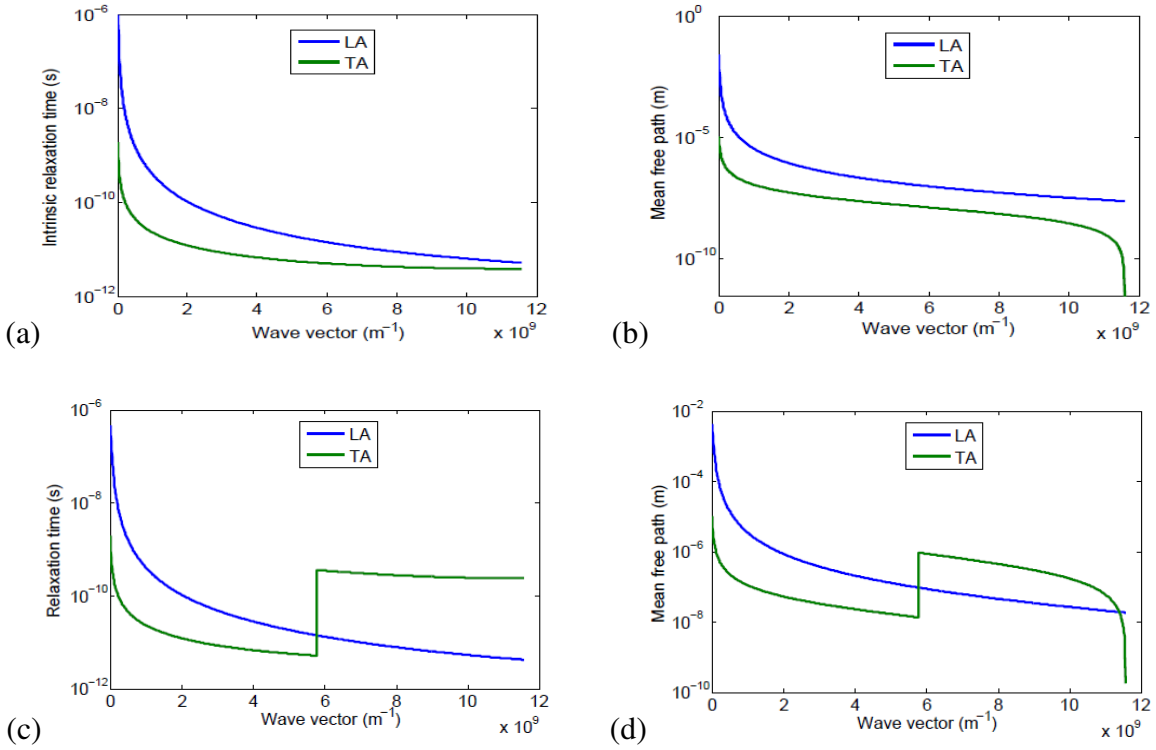

Fig. 2.8. (a) Phonon-phonon (intrinsic) relaxation time used in this work for LA and TA modes as a function of the wave vector. (b) Intrinsic mean free path of LA and TA modes. (c) Relaxation time of LA & TA modes. (d) The mean free path of LA & TA modes.

Cartesian coordinates:

If we use the discretization in the ensemble of Cartesian coordinates, the elementary volume $d\vec{q}^3$ takes the form $d\vec{q}^3 = dq_x dq_y dq_z$. Then, the thermal conductivity is:

$$K = \sum_{s=LA,TA} \frac{1}{3} \int_{-G}^{G} \int_{-G}^{G} \int_{-G}^{G} \frac{\hbar \omega_s^2 \left(q_x, q_y, q_z\right)}{k_B T^2} . v_{g,s}^2 \left(q_x, q_y, q_z\right) . \tau_s \left(q_x, q_y, q_z\right) \cdot \frac{\exp\left(X_s\right)}{\left(\exp\left(X_s\right)-1\right)^2} \frac{dq_x dq_y dq_z}{8\pi^3} . \quad (2.18)$$

Here we consider a spherical Brillouin zone, so a wave vector of this zone satisfies the condition $q_x^2 + q_y^2 + q_z^2 \leq G^2$, where $G = 2\times\pi/a$ is the reciprocal vector and a is the crystal parameter.

The important parameter to check is the minimum number of discretization steps N_q on each axis q_x, q_y, q_z to have a good physical description. The cell number in the Brillouin zone

is proportional to N_q^3. If N_q = 50, the Brillouin zone is divided in about 125.000 cells. In Fig. 2.9a, we plot the bulk conductivity as a function of the number of discretization cells at 300 K and 400 K. We see that the conductivity reaches quickly the expected value when increasing the number of cells. When the cell number is high enough, i.e. the cells are sufficiently small, the bulk conductivity reaches the value of 149 $Wm^{-1}K^{-1}$. In what follows, we discretize the q-space with N_q = 120 (~10^6 cells).

The calculated thermal conductivity is plotted as a function of the temperature in Fig. 2.9b. It's seen that the conductivity obtained varying Eq. 2.18 is close enough to that obtained using Eq. 2.17, and also to the experimental ones [Glassbrenner64]; this validates our approach.

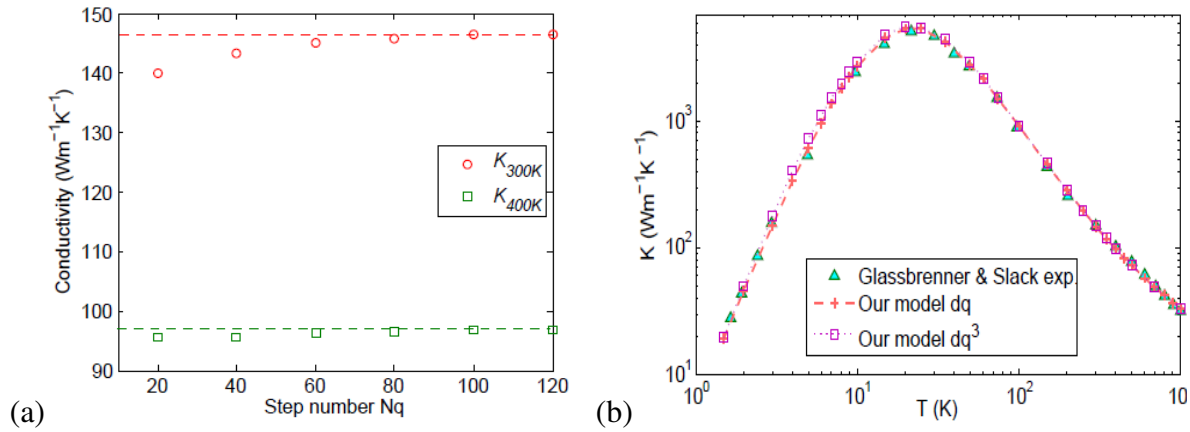

Fig.2.9. (a) Thermal conductivity of bulk silicon as a function of step number in our calculation for 300 K and 400 K. (b) The thermal conductivity from Glassbrenner & Slack's experience [Glassbrenner64] (triangle), from Eq. 2.16 (dashed red line) and from Eq. 2.17 (dotted square line).

3.2. Thermal conductivity in nanostructure (Analytical approach)

In this sub-section, a model of thermal conductivity, derived from simple physical considerations, is developed to include easily the influence of the sample geometry and of the interface roughness with the scattering parameters validated above.

While at 300 K optical phonons can contribute up to 20 % to the thermal conductivity in nanostructures (10-20 nm film-thicknesses or wire diameters) [Tian11], but only up to 4 % in bulk materials [Broido05], therefore we will ignore them here to preserve the simplicity of the model.

We intend to calculate the conductivity for films and wires schematized in Fig. 2.15. L_x is the length, $L_z$is the thickness and the L_y is the width.

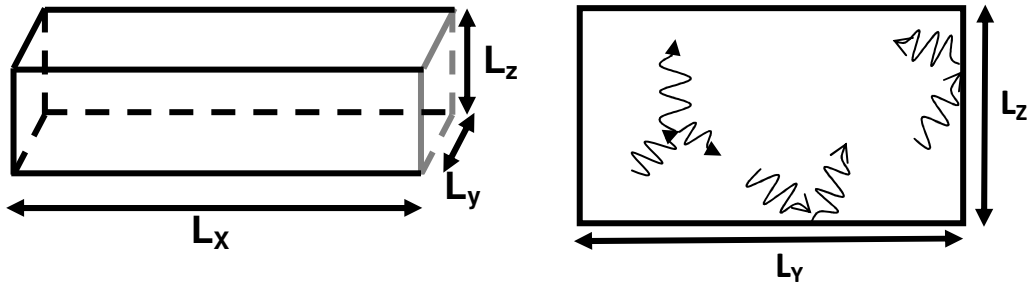

Fig.2.10. The 3D-schematic and 2D-side view of the device geometry considered in this sub-section.

The scattering rate takes into account all the previously mentioned scattering via the Matthiessen's rule

$$\frac{1}{\tau_s}=\frac{1}{\tau_{s,bulk}}+\frac{1}{\tau_{s,B}}, \tag{2.19}$$

where $\tau_{s,\mathrm{B}}$ is the boundary scattering of mode s (s = LA, TA), defined as in Eq. 2.11.

3.2.1 Thermal conductivity in Si films

For the film (2D structure), L_x and L_y are equal to 10 m, and the film thickness L_z is much smaller than L_x and L_y. The phonon-boundary scattering time in the purely diffusive case (specular parameter $\vec{p}=0$) is

$$\tau_b=\frac{L_Z}{\left|V_{gz}\right|}. \tag{2.20}$$

In Fig. 2.11, we plot the thermal conductivity as a function of the film thickness L_z. The thermal conductivity approaches K_{bulk} for $L_z \geq 10\,\mu\mathrm{m}$. Available experimental thermal conductivity data for silicon films at 300 K are reported for comparison.

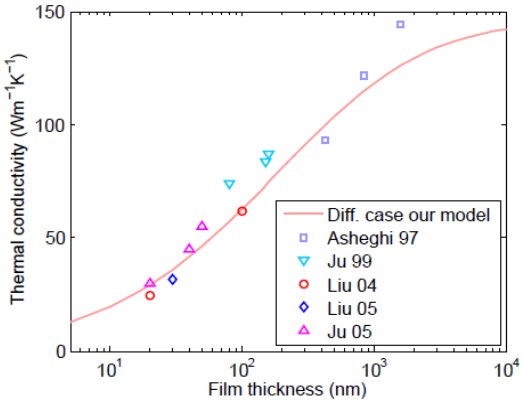

Fig.2.11. Comparison of our thermal conductivity model w/o specular parameter and experimental data for Si films.

The model prediction is in good agreement with experimental data of five independent studies, in particular in the thin-film thickness zone from 20 nm to 100 nm. We obtain a conductivity value of 29.1 $Wm^{-1}K^{-1}$ for 20 nm-film thickness – the minimum measured film thickness available in the literature, for which the experimental value is about 24.6 $Wm^{-1}K^{-1}$ in Liu et al. [Liu04] and about 29.7 $Wm^{-1}K^{-1}$ [Ju05]. For 100 nm-thickness films, the conductivity obtained from our model is 62.5 $Wm^{-1}K^{-1}$, which is very close to the experimental data of Liu *et al.* [Liu05]. Above this zone, there are some discrepancies between our model predictions and measured values, but the model captures the experimental trend. The highest error at 1.6 µm-thickness film is about 12 $Wm^{-1}K^{-1}$, which is about 8 % of error in comparison with the measured data.

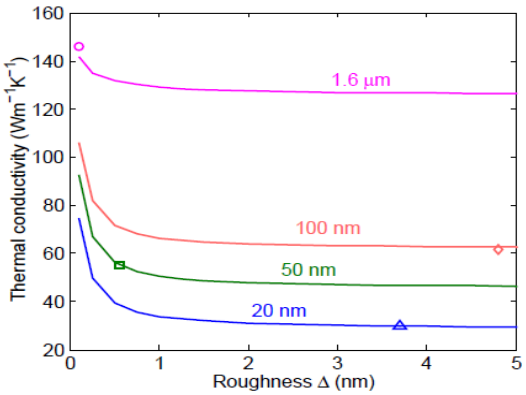

Fig.2.12. Thermal conductivity as a function of the roughness Δ for film of 20 nm, 50 nm, 100 nm and 1.6 µm thickness; symbols with same colours are the experimental data. (20 nm from [Ju05], 50 nm from [Ju05], 100 nm from [Liu04] and 1.6 µm from [Asheghi97]).

In Fig. 2.12, we plot the thermal conductivity as a function of the roughness height Δ at the Si-SiO_2 interface for various thicknesses. Our simple approach predicts a strong impact of Δ on thermal conductivity.

3.2.2. Thermal conductivity in Si wires

3.2.2a. Circular and square cross-section wires

In this section, we compare the thermal conductivity between circular cross-section and square cross-section Si wires.

For a circular-section wire, the in-plane group velocity is defined as

$$v_{in\ plane} = \sqrt{v_y^2 + v_z^2}\ . \tag{2.21}$$

Then, in the purely diffusive case, the related lifetime is

$$\tau_b\left(q_x, q_y, q_z\right) = \frac{D}{\left|v_{in\ plane}\right|}. \tag{2.22}$$

Where D is the wire diameter.

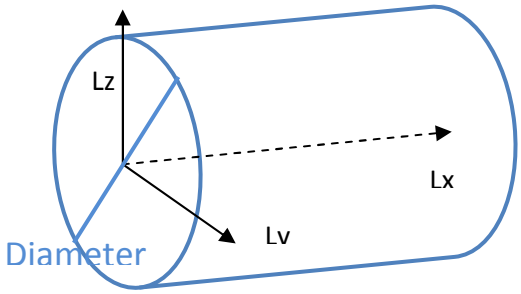

Fig.2.13. Circular section wire structure and coordinates used in this work.

The phonon-boundary lifetime in the square wire is extracted from Eq.2.32, as

$$\tau_b\left(q_x, q_y, q_z\right) = \min\left\{\frac{A}{\left|V_{gy}\right|}, \frac{A}{\left|V_{gz}\right|}\right\}. \tag{2.23}$$

In Fig. 2.20, we compare the different kinds of wires with the same cross-sectional area, so we have

$$S = \pi \times \frac{D^2}{4} = A^2\ . \tag{2.24}$$

Our model captures the experimental trend. As expected, it is close to the experimental data for large wires. It should be mentioned that there is a large spreading among available experimental data. For 50 nm-diameter wires, the calculated conductivity is 47.3 $Wm^{-1}K^{-1}$, while the experimental values are 41.3 $Wm^{-1}K^{-1}$ [Li03] and 8.75 $Wm^{-1}K^{-1}$ [Hochbaum08].

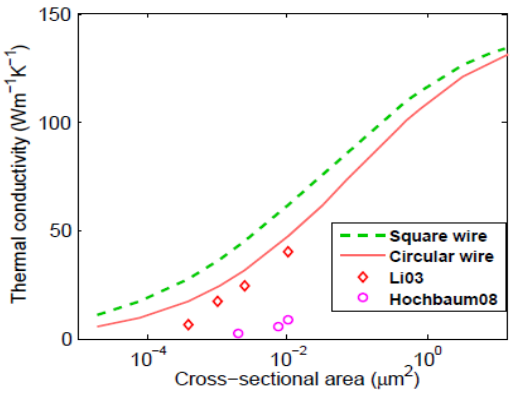

Fig. 2.14. Comparison of the calculated thermal conductivity with experimental data for circular and square cross-section Si wires.

At the same wire size, the measured conductivity of Hochbaum is much lower than that of Li, due to the fact that the surface roughness in Hochbaum's wires (~ 3 nm) is greater than in Li's wires (~0.3 nm) [Martin09]. In these wires, the full phonon dispersion and the phonon confinement should be included. The discrepancy for small diameters may be due to the phonon dispersion confinement and the surface roughness [Balandin98, Chen08, Martin09]. If the two effects were included, the lattice thermal conductivity would decrease.

3.2.2b. Rectangular cross-section wire

In this sub-section, we investigate the dependence of the thermal conductivity on the geometry of rectangular cross-section Si wire. Using the 3ω method, the experimental measurements have been performed by P. Allain (MicroNanoBio research group, IEF) [Allain12] to determine the thermal conductivity of several rectangular wires. The wires have the same thickness of 160 nm, while the widths are 80 nm, 140 nm, 200 nm and 260 nm.

The measured and calculated results in the temperature range from 200 K to 450 K are put together in Fig. 2.15. The calculation was made for several cases: roughness of 0.5Å, 1 Å, 2 Å, 5 Å and purely diffusive phonon – boundary collisions. The measured values are in circles, with error bars representing an error of 25 %.

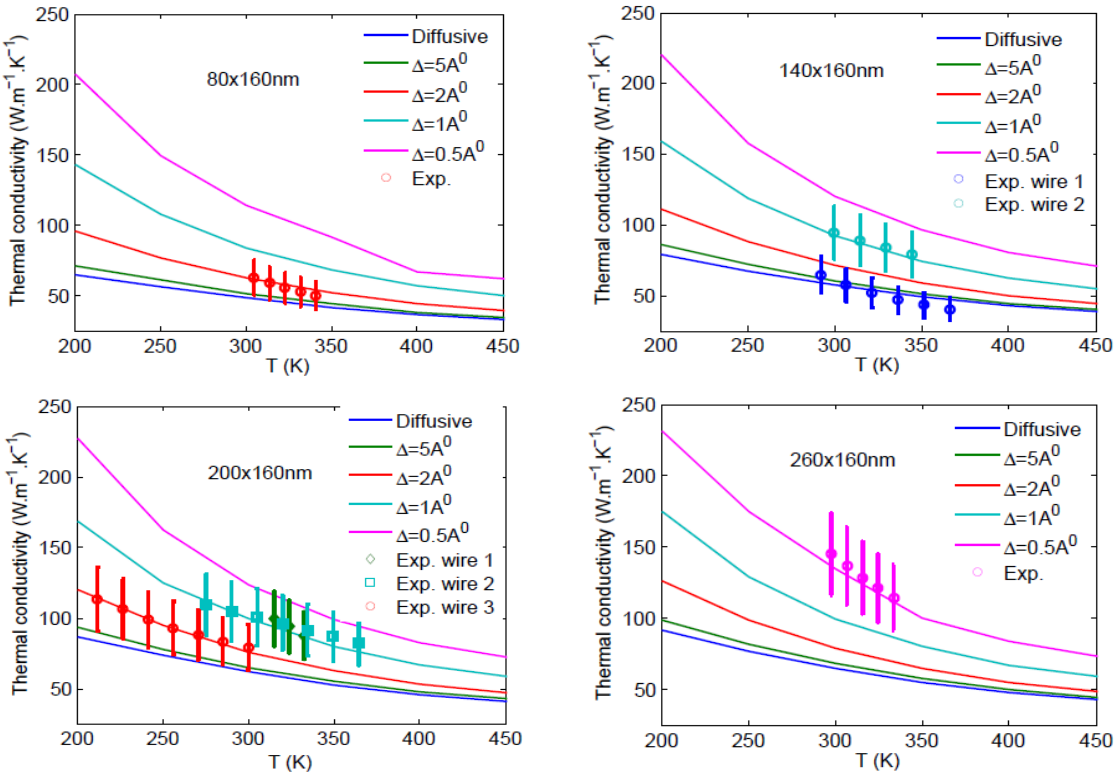

Fig.2.15. Thermal conductivity of four rectangular wires: 80 nm×160 nm, 140 nm×160 nm, 200 nm× 160 nm and 260 nm×160 nm in the temperature range from 200 K to 450 K. Δ is the roughness standard deviation.

Taking into account this measurement error, a roughness value in each wire can be quite well estimated. The slopes of calibrated conductivities as a function of the temperature are in good agreement with those obtained experimentally. The values of the roughness are in the range of what was expected as regard to the technological process.

3.2.2c. Transition between wires and films

Here we analyze the transition between wires and films. The wire thickness L_z is fixed to be 100 nm, while the width L_y varies from 0.05 L_z to 100 L_z.

In Fig. 2.16, the thermal conductivity is plotted as a function of the width/thickness ratio for different thicknesses. The dashed lines are the values for the film of the same thicknesses. There is no longer any size effect of the width (film-like behavior) when the width is about ten times greater than the thickness.

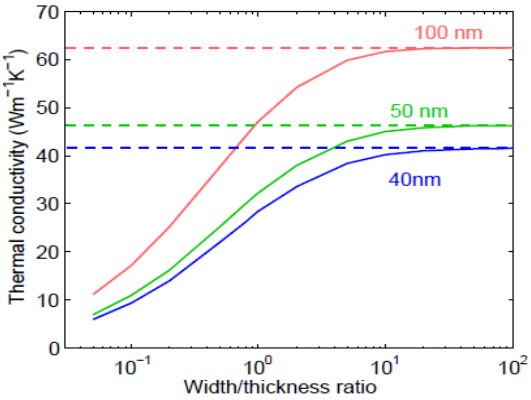

Fig.2.16. Thermal conductivity as a function of the width/thickness ratio for thickness of 40 nm (blue line), 50 nm (green line) and 100 nm (red line). The related film values for each thickness are in dashed lines, respectively.

3.3. Conclusion

In conclusion, we have presented a new set of scattering parameters for bulk silicon with a quadratic dispersion relation for phonons in the direction [100]. We have obtained thermal conductivities for bulk silicon in good agreement with experimental data.

For 3D (bulk), 2D (film) and 1D (wire) Si structures, the results capture well the experimental trends of thermal conductivity as a function of film thickness or of wire size expected. The accuracy of results for nanowires of small diameters (below 50 nm) could be improved by taking into account the phonon confinement effect. Then, by tuning the values of the roughness, we have found an excellent agreement between the calculated and the measured [Allain12] thermal conductivity as a function of temperature for various rectangular cross-section nanowires of different dimensions. Fitting the experimental data with the model allows us to predict realistic values of the roughness of these wires.

4. NUMERICAL SOLUTION OF BTE

Until now we have considered the set of scattering parameters and the phonon dispersion in bulk Si, and also the phonon-boundary scattering and the roughness effects in Si nanostructures. This set of parameters is used to solve numerically the stationary BTE for phonons under the relaxation time approximation (RTA).

In this section, we will describe the algorithm, the discretization and initialization processes, and the boundary conditions used to solve the BTE. The validation will be carried out via the thermal conductivity in bulk Si and in Si films. Then, we will study the heat transport in Si bars from diffusive to ballistic transport regimes.

4.1. General algorithm

We propose to solve numerically the stationary BTE under the RTA which writes

$$\vec{v}_{g,s} \cdot \vec{\nabla}_{\vec{r}} N_s(\vec{r},\vec{q}) = -\frac{dN_s(\vec{r},\vec{q})}{dt}\Big|_{scatt} + G(\vec{r},\vec{q}), \tag{2.25a}$$

where

$$\frac{dN_s(\vec{r},\vec{q})}{dt}\Big|_{scatt} \approx -\frac{N_s(\vec{r},\vec{q}) - N_{s,Tscatt}(\vec{r},\vec{q})}{\tau_s\left(T_{scatt}(\vec{r}),q\right)} \tag{2.25b}$$

is the scattering term in the RTA approximation and $G(\vec{r},\vec{q})$ is the phonon generation term.

4.1.1. Fourier equation

The first step of the algorithm is to find a good approximation of the scattering term. Indeed, the RTA requires the knowledge of the temperature T_{scatt} which characterizes the quasi equilibrium phonon distribution $N_{s,Tscatt}$. Unfortunately, the ambient temperature T_{amb} is not a good approximation for T_{scatt} in the presence of high temperature gradients.

Thus, the scattering temperature T_{scatt} is evaluated by solving the macroscopic Fourier heat equation by considering a uniform thermal conductivity $K_T = K_T(T_{amb})$

$$K\,\Delta T + G(\vec{r}) = 0 \tag{2.26}$$

In the following, T_{scatt} will be referred as $T_{Fourier}$. Next, if the temperature differences in the device are higher than 10 K, the dependence of the thermal conductivity on the temperature (K_T-T relation) is taken into account. Then, the heat equation (Eq. 2.27) with non-uniform K_T is solved iteratively to the temperature $T_{Fourier}$ (particular analytical solutions of this equation are described in appendix A.):

$$\nabla\left(K_T \nabla T\right) + G(\vec{r}) = 0 \tag{2.27}$$

4.1.2. BTE for each phonon mode

For optical phonons, the BTE becomes:

$$\vec{v}_{g,s}(\vec{q})\cdot\tau_{LTO}(\vec{q})\cdot\vec{\nabla}_{\vec{q}}N_s(\vec{r},\vec{q}) = -\left[N_s(\vec{r},\vec{q}) - N_{s,TFourier}(\vec{r},\vec{q})\right] + G_s^{e-LTO}(\vec{q},\vec{r})\cdot\tau_{LTO}(\vec{q}) \quad , \tag{2.28}$$

where the average lifetime τ_{LTO} takes the value of 3.5 ps [Menéndez84], $G_s^{e\to LTO}(\vec{q},\vec{r})$ is the generation term of LTO phonons resulting from electron-phonon scattering. $\vec{v}_{g,s}(\vec{q})$ is the group velocity of the mode *s* for the wave vector $\vec{q}$.

For acoustic phonons, considering electron-phonon scattering and the decay of LTO modes as a source of acoustic phonons, the BTE can be written as

$$\vec{v}_{g,s}\cdot\tau_s(\vec{q})\cdot\vec{\nabla}_{\vec{q}}N_s(\vec{r},\vec{q}) = -\left[N_s(\vec{r},\vec{q}) - N_{s,TFourier}(\vec{r},\vec{q})\right] + G_s^{e-LTA}(\vec{q},\vec{r})\cdot\tau_s(\vec{q}) + G_s^{LTO\to LTA}(\vec{q},\vec{r})\cdot\tau_s(\vec{q}), \tag{2.29}$$

where the generation terms includes the contribution of electron-phonon scattering $G_s^{e-LTA}(\vec{q},\vec{r})$ and of LTO decay $G_s^{LTO\to LTA}(\vec{q},\vec{r})$ that is supposed to depend on electron-LTO generation rate and on the probability $P_s^{LTO\to LTA}(\omega_s(\vec{q}))$ to have a LTA phonon resulting from LTO decay as presented in sub-section 2.3 (cf. Fig. 2.4).

$$G_s^{LTO\to LTA}(\vec{q},\vec{r}) = \left(\sum_{\vec{q}_{LTO}} G^{e-LTO}(\vec{q}_{LTO},\vec{r})\right)\cdot\frac{P_s^{LTO\to LTA}(\omega_s(\vec{q}))}{N_{\vec{q}'}\big|_{\omega_s(\vec{q}')=\omega_s(\vec{q})}}, \tag{2.30}$$

where $\sum_{\vec{q}_{LTO}} G^{e-LTO}(\vec{q}_{LTO},\vec{r})$ is the total generation rate of LTO modes extracted from MC simulation (which, in stationary regime is exactly the number of optical phonons that decay to generate acoustic phonons). The probability of final states for each acoustic mode is normalized to ensure that the total probability is unity. $N_{\vec{q}'}\big|_{\omega_s(\vec{q}')=\omega_s(\vec{q})}$ is the number of wave vectors $\vec{q}'$ satisfying the condition $\omega_s(\vec{q}') = \omega_s(\vec{q})$. Indeed, the optical phonons are generated by hot electrons, so they can have various wave vectors. Since one optical phonon mode with

a given wave vector can decay into LTA modes with large spreading in wave vectors, we assume that at a given frequency ω, LTA phonons due to the LTO decay can have any wave vector $\vec{q}'$ that satisfies the condition $\omega_s(\vec{q}') = \omega_s(\vec{q})$. The probability to have an acoustic phonon with wave vector $\vec{q}$, which satisfies this condition, is then $\frac{1}{N_{\vec{q}'}\big|_{\omega_s(\vec{q}')=\omega}}$. The scattering rate τ_s includes the phonon-phonon, phonon-impurity and phonon-boundary (as in Eq. 2.15).

4.2. Discretization and initialization

4.2.1. Discretization

Consider a film oriented so that the cross-plane direction and the thermal gradient are along the z-direction. For this one-dimensional (space coordinates) system, the Eq. 2.25a can be written as

$$\left(\tau_s\left(T(\vec{r}),q\right)\cdot v_{z,s}(\vec{q})\cdot\frac{\partial}{\partial z}+1\right)N_s(z,\vec{q}) = N_{s,Tscatt}(z,\vec{q}) + G(z,\vec{q}). \tag{2.31}$$

The group velocity $\vec{v}$ and its projection v_z are defined by the following expressions:

$$v_s = \frac{\partial\omega_s}{\partial q}, v_{z,s} = \frac{q_z}{|\vec{q}|}\cdot|\vec{v}_s|. \tag{2.32}$$

The derivative term $\partial N_s / \partial z$ at point j is approximated by using the finite difference method. The positive direction (along the z axis) is from left to right. Phonons which have a positive group velocity can only travel from the left to the right and the others can only go from the right to the left. So, this derivative term is considered differently in the two cases.

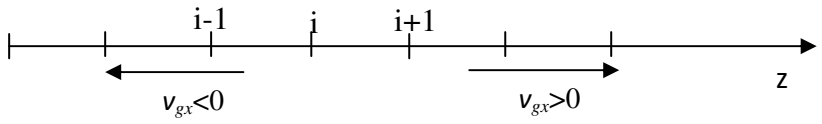

Fig. 2.17. Diagram of discretization.

- If the group velocity is positive: $\frac{\partial N_s^i}{\partial z_i} = \frac{N_s^{i+1} - N_s^i}{\Delta z_i}$

- If the group velocity is negative: $\frac{\partial N_s^i}{\partial z_i} = \frac{N_s^i - N_s^{i-1}}{\Delta z_i}$.

The interval Δz must be equal to or smaller than the mean free path to ensure that the solution is exact.

4.2.2. Discretization in reciprocal space

The first step of the simulation procedure is the choice of geometry and mesh.

The choice of the step number N_q along q_x, q_y and q_z axes is important. After having investigated the effect of the step number and therefore of the number of bins in the first Brillouin zone, we have chosen a discretization by 100 steps along each axis, i. e. about 5×10^5 bins in ω.

The density of phonon at the boundaries is fixed at equilibrium as:

$$N_s(\vec{r},\vec{q})\,d\vec{q}^3 = \frac{1}{\exp\left(\frac{\hbar\omega_s(\vec{q})}{k_B T_{Fourier}(\vec{r})}\right)-1} \times g_s \times \frac{d\vec{q}^3}{8\pi^3}. \quad \text{(Rewritten from Eq. 2.16)}$$

The first cell is raised to the hot temperature T_h, the last one to the cold temperature T_c.

At a given position, it is required that the distribution of initialized phonon obeys the occupation in energy at a given temperature, which can be calculated from the following expression:

$$N_s(\vec{r},\omega) = \frac{1}{\exp\left(\frac{\hbar\omega_s}{k_B T(\vec{r})}\right)-1} \cdot D(\omega_s)\, g_s d\omega = \frac{1}{\exp\left(\frac{\hbar\omega_s}{k_B T(\vec{r})}\right)-1} \cdot \frac{K^2}{2\pi^2 v_s} g_s d\omega. \quad (2.33)$$

The LA and TA phonon occupation densities are plotted in Fig. 2.18a as a function of ω at 300 K and 500 K and compared with the theoretical curves, showing an excellent agreement. Phonon occupations in a wave vector projection (for example, q_z) that are meaning with the theoretical calculations are shown in Fig. 2.18b.

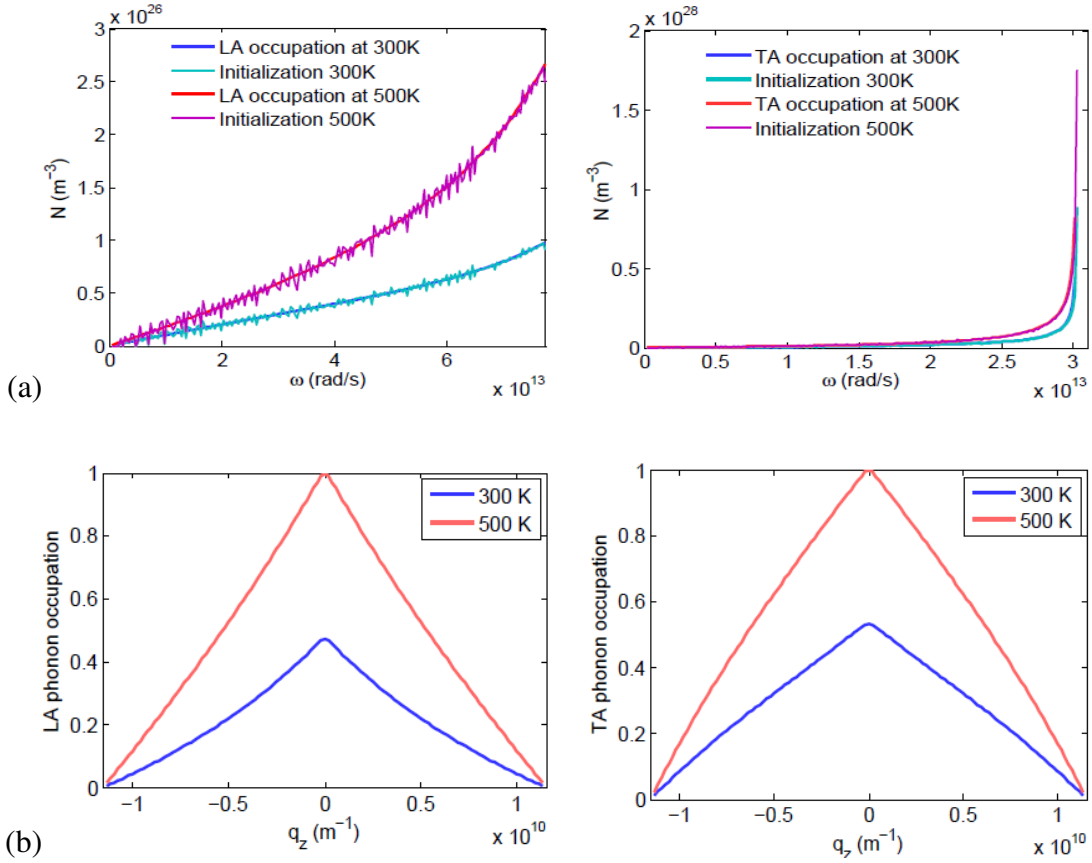

Fig. 2.18. (a) Theoretical and sampled frequency phonon distribution at 300K and 500K for silicon. (b) Normalized LA and TA occupations at 300K and 500K as a function of wave vector projection.

4.3. Boundary condition

At the two contacts, the boundary condition consists in fixing the temperature and thus in fixing the phonon number according to the corresponding Bose-Einstein distribution. This boundary condition ensures that all phonons scatter diffusively when they interact with the system boundaries [Sellan10].

4.4. Matrix form

As seen previously, the derivative in the left-hand-side is discretized differently in two cases of v_{gz}.

+ If the group velocity projection v_{gz} is positive: $\frac{\partial N_s^i}{\partial z_i} = \frac{N_s^{i+1} - N_s^i}{\Delta z_i}$.

So, we obtain the following numerical scheme:

$$\left(\tau_s\left(T_{scatt}\left(\vec{r}\right),q\right)\cdot v_{z_i,s}\left(\vec{q}\right)\cdot\frac{\partial}{\partial z_i}+1\right)N_s\left(z_i,\vec{q}\right)\quad\rightarrow\quad A_1^i\cdot N_i+B_1^i\cdot N_{i+1}\ , \tag{2.34}$$

where $A_1^i=1+\dfrac{\tau_s\left(T_{scatt}\left(z_i\right),q\right)\cdot v_{z_i,s}}{\Delta z_i}$ and $B_1^i=-\dfrac{\tau_s\left(T_{scatt}\left(z_i\right),q\right)\cdot v_{z_i,s}}{\Delta z_i}$.

By fixing the temperature at the two contacts, we can write the transport equation under the following matrix form:

$$\begin{pmatrix}1&0&0&0&0&0\\0&A_1^i&B_1^i&0&0&0\\\ddots&\ddots&\ddots&\ddots&\ddots&\ddots\\0&0&0&A_1^i&B_1^i&0\\0&0&0&0&0&1\end{pmatrix}\begin{pmatrix}N_1\\N_2\\\vdots\\N_{Nz-1}\\N_{Nz}\end{pmatrix}=\begin{pmatrix}N_{T_1^{scatt}}+G\cdot\tau_s\left(T_{scatt}\left(z_i\right),q\right)\\N_{T_2^{scatt}}+G\cdot\tau_s\left(T_{scatt}\left(z_i\right),q\right)\\\vdots\\N_{T_{Nz-1}^{scatt}}+G\cdot\tau_s\left(T_{scatt}\left(z_i\right),q\right)\\N_{T_{Nz}^{scatt}}+G\cdot\tau_s\left(T_{scatt}\left(z_i\right),q\right)\end{pmatrix}. \tag{2.35}$$

+ If the group velocity projection v_{gz} is negative: $\dfrac{\partial N_s^i}{\partial z_i}=\dfrac{N_s^{i-1}-N_s^i}{\Delta z_i}$.

$$\left(\tau_s\left(T_{scatt}\left(\vec{r}\right),q\right)\cdot v_{z,s}\left(\vec{q}\right)\cdot\frac{\partial}{\partial z}+1\right)N_s\left(z,\vec{q}\right)\quad\rightarrow\quad A_2^i\cdot N_{i-1}+B_2^i\cdot N_i\ , \tag{2.36}$$

where $A_2^i=\dfrac{\tau_s\left(T_{scatt}\left(z_i\right),q\right)\cdot v_{z_i,s}}{\Delta z_i}$ and $B_2^i=1-\dfrac{\tau_s\left(T_{scatt}\left(z_i\right)q\right)\cdot v_{z_i,s}}{\Delta z_{i-1}}$.

Similarly, this schema under the matrix form is

$$\begin{pmatrix}1&0&0&0&0&0\\B_2^i&A_2^i&0&0&0&0\\\ddots&\ddots&\ddots&\ddots&\ddots&\ddots\\0&0&0&0&B_2^i&A_2^i\\0&0&0&0&0&1\end{pmatrix}\begin{pmatrix}N_1\\N_2\\\vdots\\N_{Nz-1}\\N_{Nz}\end{pmatrix}=\begin{pmatrix}N_{T_1^{Fourier}}+G\cdot\tau_s\left(T_{Fourier}\left(z_i\right),q\right)\\N_{T_2^{Fourier}}+G\cdot\tau_s\left(T_{Fourier}\left(z_i\right),q\right)\\\vdots\\N_{T_{Nz-1}^{Fourier}}+\ G\cdot\tau_s\left(T_{Fourier}\left(z_i\right),q\right)\\N_{T_{Nz}^{Fourier}}+G\cdot\tau_s\left(T_{Fourier}\left(z_i\right),q\right)\end{pmatrix}. \tag{2.37}$$

4.5. Effective temperature

At the nanoscale and/or for non-equilibrium phonon distribution, the concept of temperature is meaningless. Considering the phonon distribution, a "phonon distribution field" is more relevant than using a temperature field. Nevertheless, the information on distribution of phonons can be reduced to an "equivalent temperature" field by using the local phonon energy resulting from the actual phonon distribution (which may be out of equilibrium). Thus, an equilibrium phonon distribution following the Bose–Einstein distribution thermalized at the effective temperature provides the same local energy density [Pop06].

The equilibrium local phonon energy density is obtained by

$$E_s(\vec{r}) = \iiint E_s(\vec{r},\vec{q})\, d\vec{q}^3 = \iiint \hbar\omega_s(\vec{r},\vec{q}) \frac{1}{\exp\left(\dfrac{\hbar\omega_s(\vec{r},\vec{q})}{k_B T(\vec{r})}\right)-1} \cdot g_s \cdot \frac{d\vec{q}^3}{8\pi^3}. \qquad (2.38)$$

The temperature evolution of the energy density is plotted in Fig. 2.19 for each mode of bulk Si.

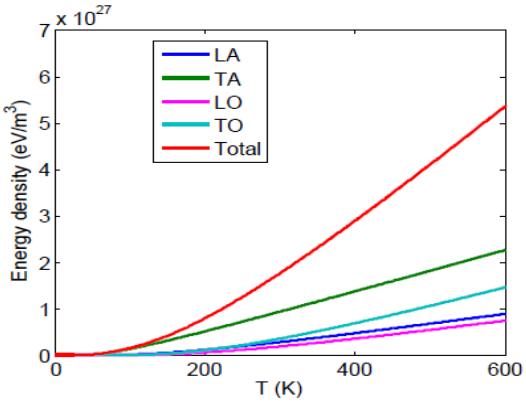

Fig. 2.19. Phonon energy density as a function of the temperature for each phonon mode. .

By using this definition of the effective temperature four mode temperatures (T_{LA}, T_{TA}, T_{LO} and T_{TO}) and the total temperature (T_{eff}) can be defined.

4.6. Validation - Thermal conductivity

In this sub-section, we validate the algorithm implemented to solve the steady-state BTE for phonons by calculating the thermal conductivity in bulk Si and Si films and comparing our simulation results with the experimental ones. Only the LA and TA modes are considered here. We solve Eq. 2.56 in a Si bar at quasi-equilibrium state with a small gradient of temperature, and without the generation term.

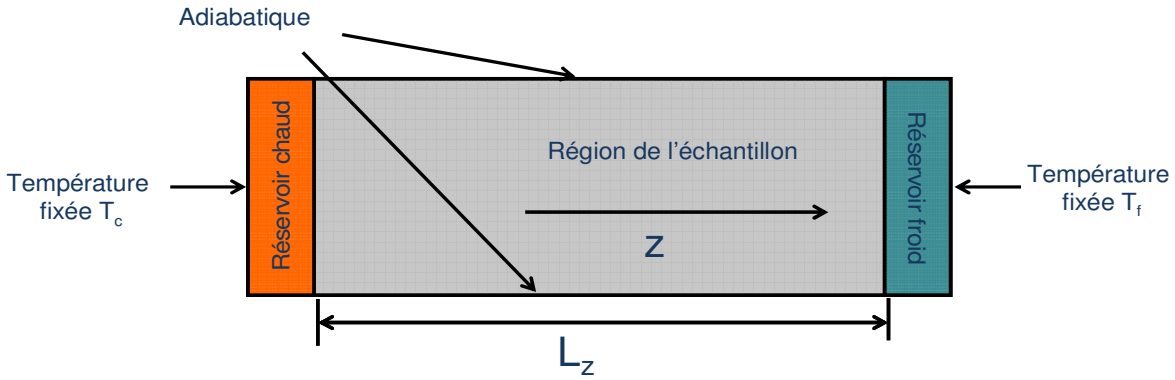

Fig. 2.20. Schema of the simulated Si bar.

The cold temperature along the bars and also at the right contact is T_c, while at left contact, the temperature is raised to T_h ($T_h > T_c$). The thermal conductivity is extracted from the phonon heat flux along the sample, according to

$$J_z(\vec{r}) = \sum_s \sum_{\vec{q}} \hbar\omega(\vec{q},\vec{r}) \times v_{s,z}(\vec{q},\vec{r}) \times N_{s,z}(\vec{q},\vec{r}) \,, \tag{2.39}$$

where J_z is the z component of the heat flux in the structure. $v_{s,z}(\vec{q})$ is the z component group velocity of s-mode phonons.

From Eq.1.41 (Chapter I), if the thermal conductance K is constant, it can be deduced from the slope of flux J as a function of the temperature difference ΔT for a sample of length L_z as

$$K = L_z \cdot \left. \frac{dJ_z}{d(\Delta T)} \right|_{\Delta T \simeq 0} . \tag{2.40}$$

4.6.1. Thermal conductivity in bulk Si

As described in section 4.1, we solve the Fourier equation (Eq. 2.26) by assuming that the thermal conductivity is uniform (small gradient of temperature ΔT).

We plot in Fig. 2.21a the heat flux for different Si bar lengths. Heat fluxes in *z*-direction are maintained by a temperature difference of 2 K, centered at 300K.

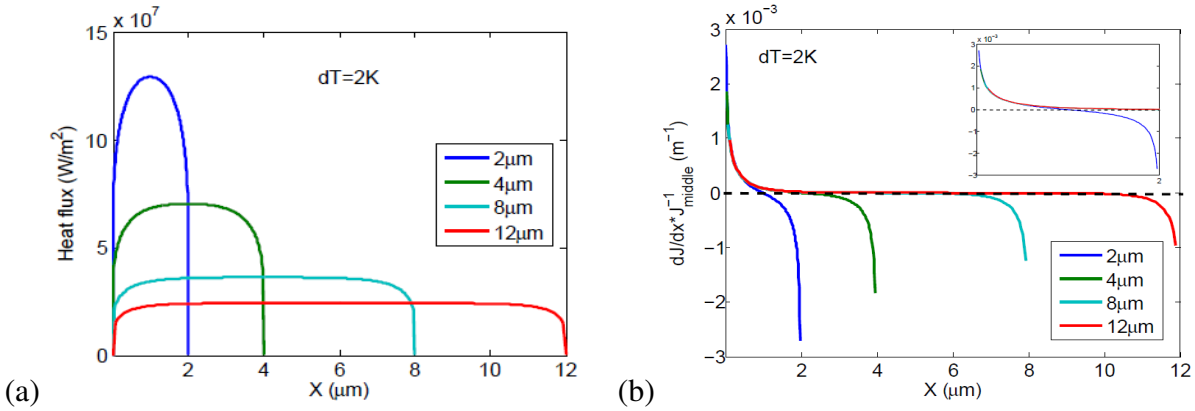

Fig. 2.21. (a) Heat flux along Si bars of different lengths with a temperature difference of 2K, centered at 300K. (b) Derivative of the heat flux divided by the corresponding flux at the middle of Si bars of different lengths with the same conditions. Inset: zoom in the range 0-2 μm

Because the two ends are fixed at 300 K as the boundary condition, there is no heat which flows inside these contacts. Therefore, for the continuity condition, the values of heat flux near the contacts are close to zero. The shorter the length is, the stronger the heat flux is. That is due to the fact that the flux is proportional to the gradient of temperature *dT/dx* (see Eq. 2.14) which is higher in the short bars than in the long bars. For a Si-bar of 2μm length, the heat flux does not attain a constant value. When the bars are longer (4 μm, 8 μm, 12 μm), constant values are obtained. We can say that the equilibrium heat transport is established in these cases.

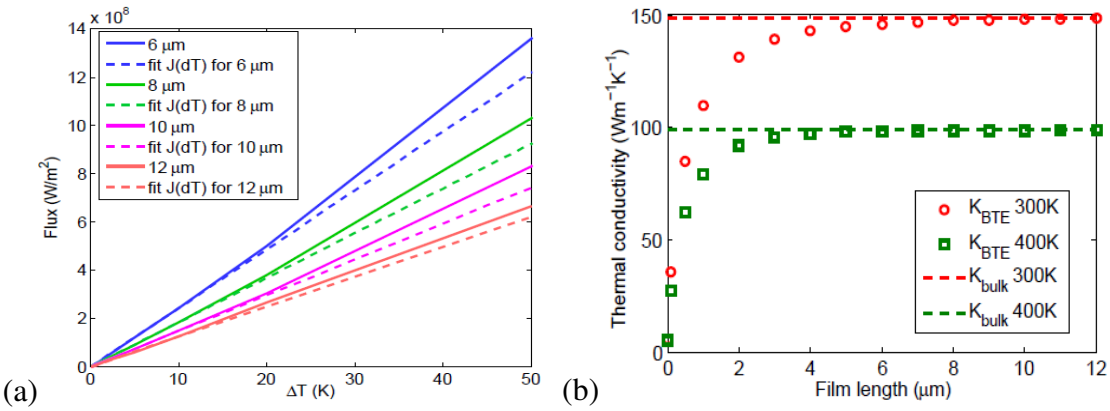

Fig. 2.22. (a) The heat flux at 300 K as a function of temperature difference *ΔT* in 6μm, 8μm, 10μm and 12 length samples and the correspondent linear fit curves, respectively. (b) The thermal conductivity inside silicon films as a function of film length.

To evaluate the length over which the flux can reach its equilibrium value, the derivation of the heat flux is calculated and divided by the value of flux in the middle of the structure. These quantities along the bar for different lengths are displayed in Fig. 2.21b. For all the considered bar, except the 2 µm-bar, the curves haves a flat shape in the centre of the structure, at about 2 µm, which is about 2 times greater than the mean free path of acoustic phonons (see Fig. 2.8d). We assume that the heat transport in Si reaches the equilibrium regime when phonons undergo a sufficient amount of collisions through the distance as long as about two times the average mean free path or more, from the contacts.

The heat flux is plotted in Fig. 2.22a as a function of temperature difference in 6 µm, 8 µm, 10 µm and 12 µm-length films together with the linear fitting-curves. This fitting-curves are obtained with two constraints: they must pass through the zero point and fit well the slope of $J_x(dT)$ near the zero point (ΔT from 0 to 5 K). Fig. 2.22b shows the thermal conductivity of silicon at 300 K and 400 K for a film length ranging from 10 nm to 12 µm. It is observed that for a length smaller than 4 µm, the thermal conductivity of silicon deviates significantly from (its bulk value, which is 148.8 $Wm^{-1}K^{-1}$ at 300K) in our model. That is coherent with the above analysis for the flux profiles in different lengths.

Further, simulations have been carried out in the temperature range from 100 K to 600 K on 12 µm-thick samples. The comparison of the thermal conductivities obtained from our numerical method for BTE with our analytic model and the experimental data of Glassbrenner & Black [Grassbrenner64] is shown in Fig. 2.23.

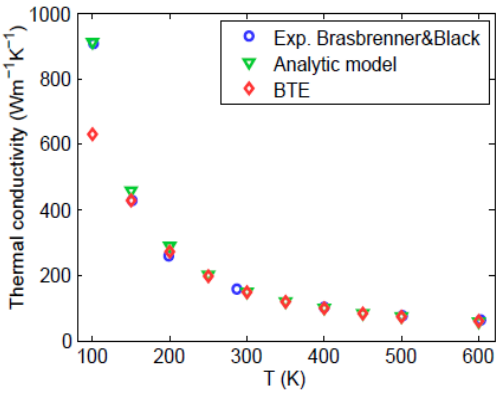

Fig. 2.23. Comparison of the thermal conductivity obtained from the numerical method, our analytic model and experimental data from [Grassbrenner64].

As shown in this figure, conductivities obtained from BTE are in agreement with the experimental data at high temperature ($T \geq 150\,\mathrm{K}$). For low temperature (lower than 150 K), the discrepancies between experimental data and numerical calculation increase. This difference can be explained by the fact that when the temperature decreases the mean free path of phonons rises strongly, and it becomes larger than the length of the structure.

We fit the evolution of the experimental conductivity as a function of temperature with an expression form $C \times T^{\alpha}$, i. e.

$$K_T = \frac{3.0 \times 10^5}{T^{1.33}}. \tag{2.41}$$

By using the Monte Carlo method to solve the BTE, Lacroix *et al*. found: [Lacroix05]

$$K_T = \frac{\exp(12.570)}{T^{1.326}} \approx \frac{2.88 \times 10^5}{T^{1.326}}. \tag{2.42}$$

In our work, the relation between thermal conductivities K and temperature is

$$K_T = \frac{3.09 \times 10^5}{T^{1.34}}, \tag{2.43}$$

This is very close to Eq. 2.41 for experimental data. This expression will be used in the next section to solve the non-linear conductivity effect when the temperature difference is high.

4.6.2. Thermal conductivity in Si films

In this sub-section, the phonon-boundary scattering is taken into account in the BTE to evaluate the in-plane (diffusive regime occurring in long bar) and cross-plane (ballistic regime in ultra-short bar) thermal conductivities in silicon thin-films at 300 K.

4.6.2a. In-plane conductivity

The same procedure of thermal conductivity calculation as in sub-section 4.6.1 is used but including roughness. Our results are plotted in Fig. 2.24 and compared to results from Discrete Ordinate Method (DOM) [Terris09] and to experimental data.

It is seen that the thermal conductivity achieved by our model is in very good agreement with that of the conductivity model (it was described in the previous chapter). Even if both

theoretical results match quite well the experimental results for all film thicknesses ranging from 20nm to 10µm. The predictions of our model are more accurate than that of the DOM that underestimates the thermal conductivity by at least 20% [Terris09].

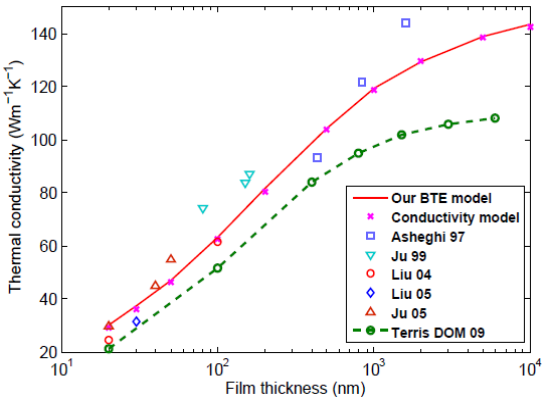

Fig. 2.24. Thermal conductivity of silicon thin-films at 300 K: our model of BTE (full line), our model of thermal conductivity calculation (crosses), DOM model (dashed line and circles), and experimental data by : Asheghi et al.[Asheghi97] (squares), Ju and Goodson[Ju99] [Ju05] (blue triangle and red triangles), Liu and Asheghi [Liu04] [Liu05](red circles and blue quadrangle)

4.6.2b. Cross-plane conductivity

To measure the cross-plane conductivity, a gradient of temperature is applied between the two surfaces of a short (but large) bar. The heat transport in this cross-plane direction is ballistic. Until now, there is only one experimental cross-plane value for 500 nm-thick silicon film obtained by Hopkins and co-workers in 2012 [Hopkins12]. The analytical model of McGaughey et al. [McGaughey11] predicts better the experimental trends than the models of Flik [Flik90] and Majumdar [Majumdar93]. However, this analytical model over-estimates by more than 2 times the experimental data. More recently, in 2012, Jeong, Datta and Lundstrom [Jeong12] used the Landauer approach and took into account a surface roughness of 0.5 nm. Their results, which are reported in Fig. 2.25a, are quite close to the experimental values.

Our model considers the phonon-boundary diffusive scattering in the cross-plane direction which is defined as the time needed for a phonon to hit one of two sides, so that

$$\begin{cases} \tau_B = \dfrac{L-z}{|v_{gz}|} \text{ if } v_{gz} > 0 \\ \tau_B = \dfrac{z}{|v_{gz}|} \text{ if } v_{gz} < 0 \end{cases} \tag{2.44}$$

The cross-plane conductivity results at 300 K are plotted in Fig. 2.25a as a function of the film thickness. The measured data are also indicated.

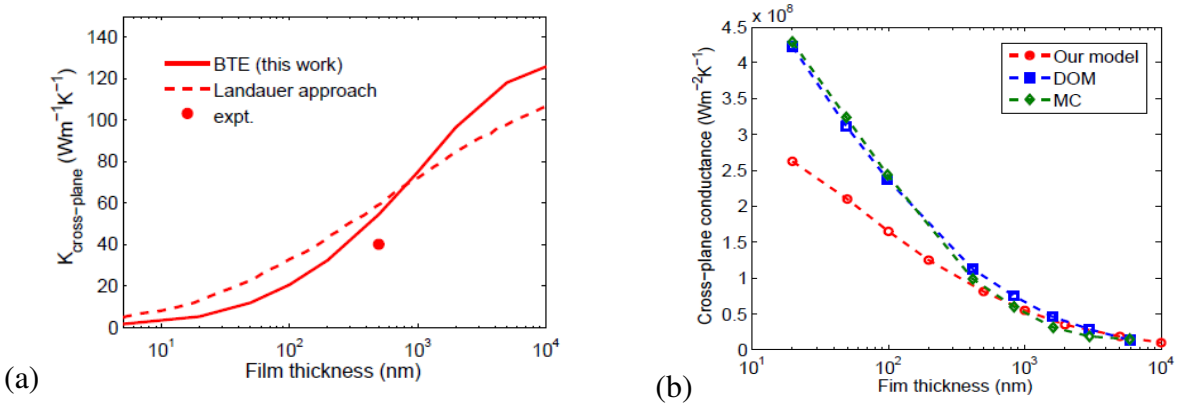

Fig. 2.25. (a) Cross-plane conductivity versus film thickness at 300K: this work (continued curve) and the experimental data [Hopkins11]. (b) Cross-plane thermal conductance of Si film for various thicknesses at 400K: our work (red curve), DOM (blue curve) and MC method (green curve) [Terris09].

For a 500 nm-thick film, our calculated result is 54.3 $Wm^{-1}K^{-1}$, while the measured value is 39.2±4.8 $Wm^{-1}K^{-1}$ [Hopkins12]. The Monte Carlo method and DOM calculations of Terris and coworkers [Terris09] for the cross-plane conductance at 400 K are shown in Fig. 2.31b. For film thicknesses at the micro scale, the results of the three models are quite close. At smaller sizes, our results are smaller than that of DOM and MC methods.

4.7 Study of heat transport in Si bars

By solving BTE for phonons in a Si bar of different lengths, we can study different transport regimes and also the transition from the diffusive to the ballistic regime. The non-linear conductivity effect observed when we apply high gradients of temperature is also discussed.

4.7.1. Heat transport regimes

We solve the BTE for various 1D-sample lengths, from 2 nm to 4 µm with different temperatures on both sides: $T_h = 310$ K and $T_c = 290$ K. The temperature in these samples is plotted in Fig. 2.26 and compared with diffusive equation results and with the ballistic temperature which is derived from the Stefan-Boltzmann law [Heaslet65].

$$T_{bal} = \left(\frac{T_h^4 + T_c^4}{2} \right)^{1/4} . \tag{2.45}$$

With the above temperatures T_h and T_c, the ballistic one is 300.5 K.

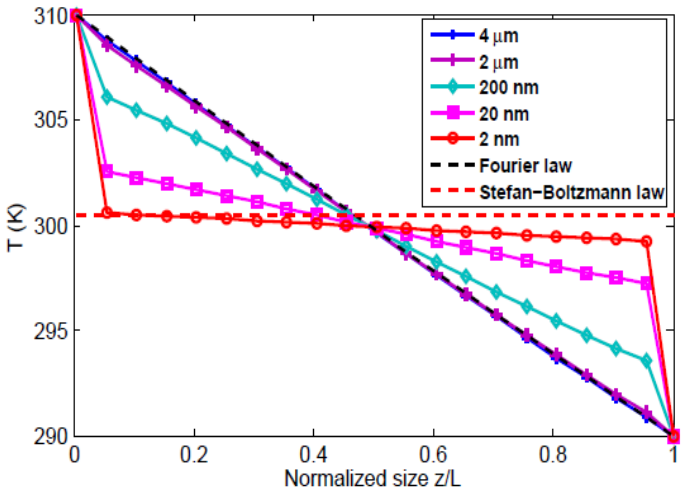

Fig. 2.26. Effective temperature profile for different sample lengths and for diffusive and ballistic limits.

The heat transport is very different for different bar lengths. For a quite long bar, the diffusive regime is obtained at ambient temperature and the temperature profile is quite linear and consistent with the Fourier law. While in very short bars, as for the 2 nm-length are, the transport is very close to the ballistic case (see Fig. 2.26). The transition between both regimes – referred as the intermediate regime- can be seen in the 20 nm and 200 nm-long Si bars.

To analyze the phonon transport, we will calculate the phonon occupation of the phonon as a function of the wave vector $\vec{q}$ by the following expression:

$$N_s(\vec{r}, q_z) = \sum_{q_x} \sum_{q_y} \frac{1}{\exp\left(\frac{\hbar\omega(\vec{q})}{k_B T} \right) - 1} \cdot g_s \cdot \frac{dq_z}{8\pi^3} \tag{2.46}$$

This expression can be deduced from the Eq. 2.16.

The distribution obtained from Eq. 2.45 is called phonon occupation in wave vector $\vec{q}$, and is displayed in Fig. 2.27 for various bar lengths.

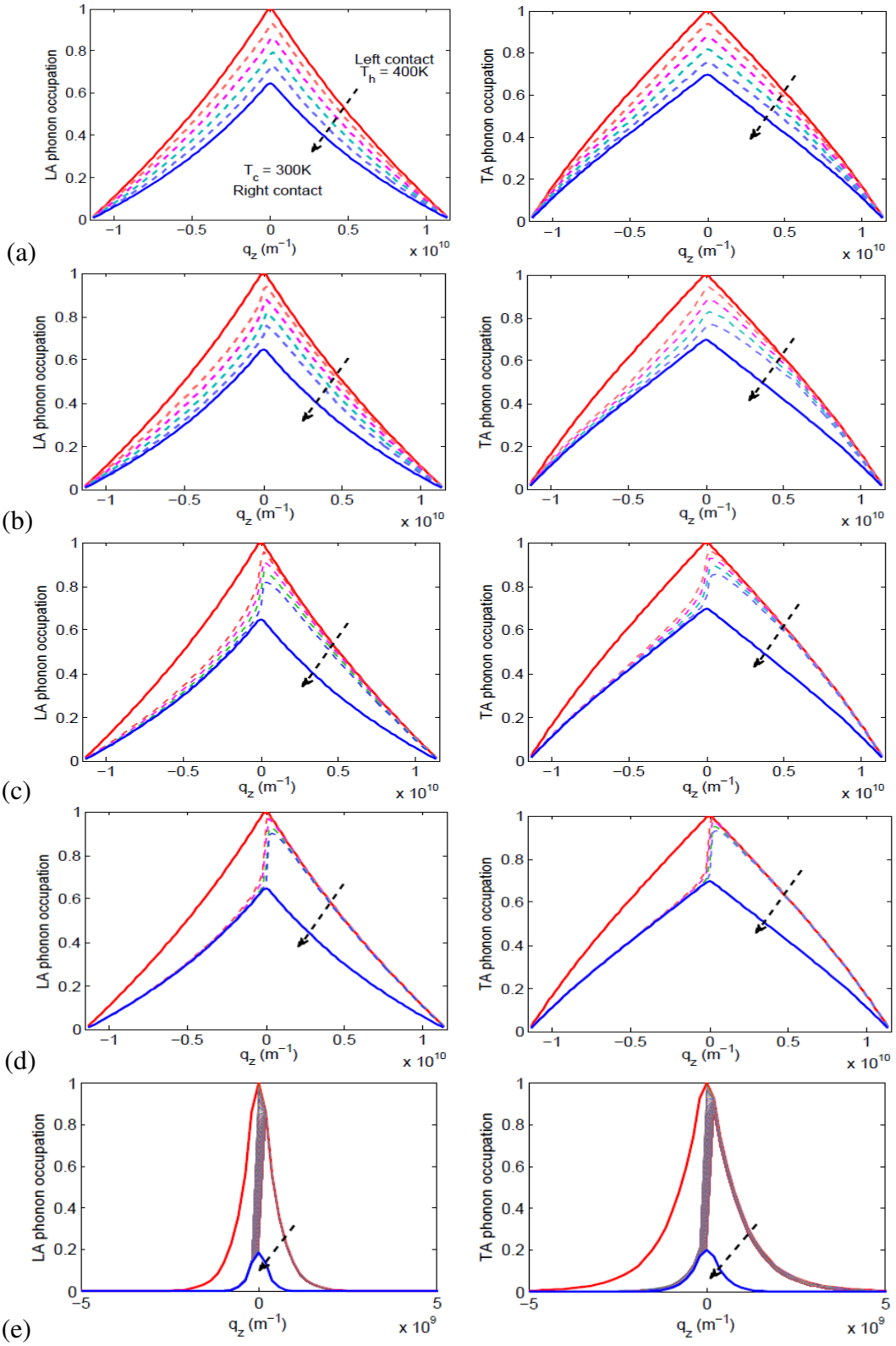

Fig. 2.27. LA (left) and TA (right) phonon occupations at different positions for different sample lengths 2 μm(a), 200 nm(b), 20 nm(c) and 2 nm(d) with T_h = 400 K and T_c = 300 K. The occupations in a 10 μm long sample of with T_h = 20 K and T_c = 10 K are in (e). The arrow is to indicate the position from left contact ($T = T_h$) to right contact ($T = T_c$).

4.7.1a. Diffusive regime

The normalized phonon occupations at 400K along the sample are shown in Fig. 2.27a for a 2µm-long sample with $T_h = 400$ K and $T_c = 300$ K. The arrow is to show the direction from left (400 K – red continuous line) to right (300 K- blue continuous line). The occupations for both LA and TA phonons are symmetric, as a function of wave vector projection q_z, which is proportional to the group velocity projection v_{gz} (see Eq. 2.32). It's well known that the phonon occupation depends on temperature: the higher the temperature is, the more phonon states are occupied. In this case of quasi-diffusive regime, the local thermodynamic equilibrium is established for both LA and TA.

4.7.1b. Ballistic regime

The ballistic transport regime occurs in small size samples or/and at low temperature. In this sub-section, to examine the size effect, we focus on the case of a 2 nm-long sample. The effective temperature profile has been plotted in Fig. 2.26.

The evolution of phonon occupations along the sample in this case is plotted. In Fig. 2. 26d, we can clearly see that the LA and TA occupations are strongly dissymmetric. Indeed, if these phonons travel without scattering, the distribution of these positive-velocity phonons remains unchanged along the device. The same mechanism explains the result for phonons flowing from the right to the left. Therefore, the phonon occupation is divided in two separated populations: phonons with positive velocity coming from the left contact at 400 K and phonons with negative velocity coming from the right contact at 300 K.

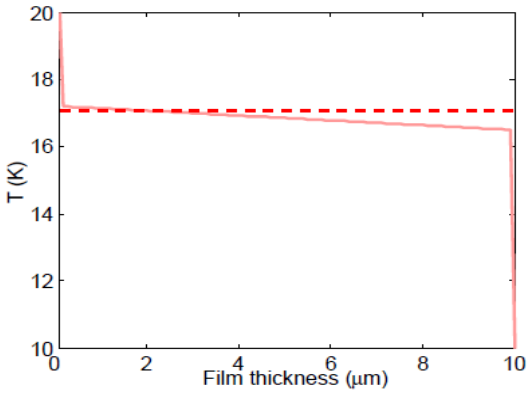

Fig. 2.28. Temperature profile in 10 µm sample with T_h= 20 K and T_c = 10 K (full line) and the ballistic temperature (dashed line) given by the Stefan-Boltzmann law (Eq. 2.68).

This ballistic regime can also be reached in a long sample at very low temperature. We solve the BTE in a sample of 10 µm with T_h = 20 K and T_c = 10 K. The temperature profile is plotted in Fig. 2.28. The phonon distributions in this case are shown in Fig. 2.27e. The temperature obtained at very low temperature follows the Stefan-Boltzmann law.

4.7.1c. Intermediate regime

When the sample thickness increases, the intermediate regime dominates - see the case of 20 nm and 200 nm-long Si bar in Fig. 2.26. In this regime, the mixture of diffusive and ballistic transport is observed also in the phonon occupation in Fig. 2.27a and Fig. 2.27c, due to the increasing influence of phonon scattering.

4.7.2. Non-linear conductivity effect

As seen previously, the thermal conductivity depends on temperature according to Eq. 2.42. If the temperature gradient ΔT is high, the spatial evolution of temperature can differ from the linear shape to show this effect.

Temperatures T_h = 500 K and T_c = 250 K are applied at the two contacts of a 5 µm-long Si bar. The temperature profiles obtained using our method and solving of the Fourier heat equation (considering a non-uniform conductivity) are plotted in Fig. 2.29.

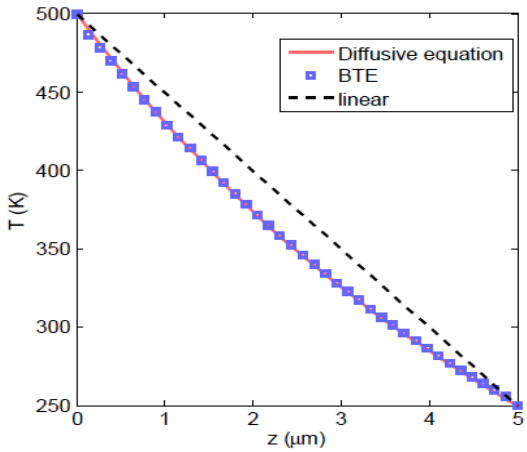

Fig. 2.29. Space distribution temperatures obtained from numerical BTE and from the analytical solution of the heat equation (temperature dependent conductivity).

There are a slight differences between the numerical method (BTE) and the analytical result (Fourier law) at the two contacts, in particular at the cold side (see Fig. 2.29). That is

observed also by using the Monte Carlo method [Lacroix05, Wong11]. This could be due to boundary effects since the mean free path at 250K is quite significant. This can be seen in Fig.2.30, in which the LA and TA occupations are shown.

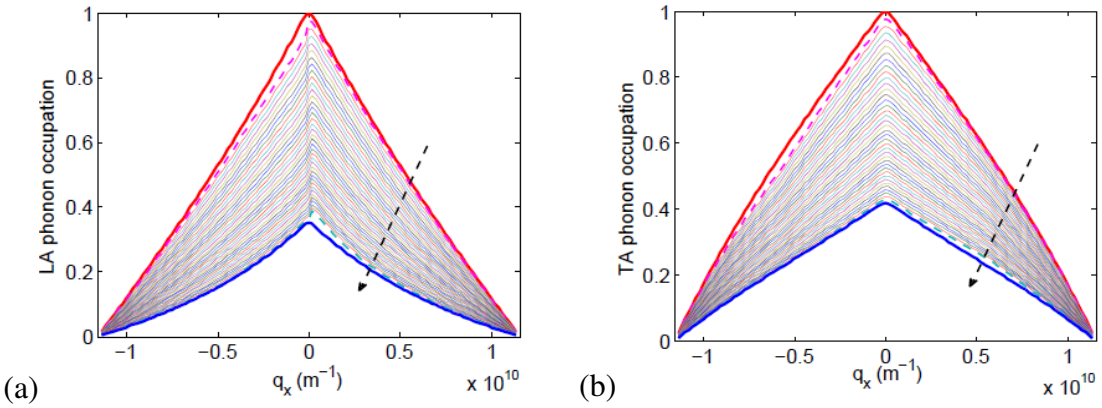

Fig. 2.30. LA and TA phonon occupations along the same sample as in Fig. 2.29 from left to right (as direction of arrow).

4.7.3. Doping effect

We use the three parameters of scattering by doping impurities (see Eq. 2.30-2.32) for Boron (B) and Phosphorus (P) doping (see Tables 2.3 & 2.4) proposed by Asheghi *et al*.

100 nm-long Si samples with different doping level, have been biased with $T_h = 20$ K and $T_c = 10$ K. The results are shown in Fig. 2.30.

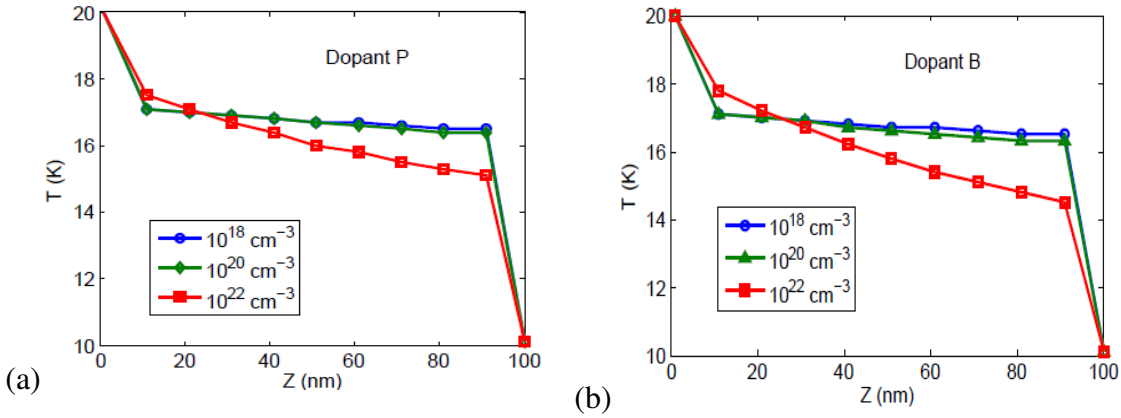

Fig. 2.30. Temperature profiles in 100 nm-thick film with different the doping concentration. (a) Phosphorus. (b) Boron.

When the numbers of impurities increase with the same temperature difference, the phonon transport becomes more diffusive: as expected, the temperature dropping across the film increases. This dropping temperature changes significantly when the doping concentration is 10^{22} cm^{-3} and above, both with B and P doping atoms. For GaAs films of 400 nm-thickness, the doping concentration which influences the phonon transport are above 10^{20} cm^{-3} [Mazumder01].

Normally, the doping in a device is not as high as 10^{22} cm^{-3}. In addition, it is seen experimentally that this effect is smaller at high temperatures (room temperature and above) [Ashghi02]. In the transport of phonons in devices that will be described in the following chapter, this effect will not be included.

4.8 Conclusion

An original numerical method to solve the stationary Boltzmann equation for phonons has been presented. This model includes the LA and TA phonons with a quadratic dispersion relation and modified Holland's model for scattering in the RTA approximation. A solution of the Fourier heat equation is coupled to estimate the scattering terms.

The model is used to compute the thermal conductivity in silicon films in the temperature range of [100 K – 600 K]. Numerical results are in very close agreement with experimental data for pure silicon until 150 K. Then, the phonon-boundary scattering is taken into account to predict in-plane and cross-plane conductivity. In-plane thermal conductivities match very well the experimental data. In addition, the cross-plane conductivity which is until now difficult to measure experimentally is investigated with our BTE model. The resulting conductivity is closer to experiment than the one obtained by other theoretical approaches.

Our numerical model has been successfully assessed in different heat transfer regimes, from diffusive to ballistic. Our method's results agree with the Stefan-Boltzmann law at the ballistic limit and with the Fourier law in the diffusive limit. The LA and TA phonon occupations are obtained by our method clarify the physics in each regime.

5. ANALYSIS OF THERMAL CONDUCTANCE OF BALLISTIC POINT CONTACT OF GA-AS

In Section 3, we have presented the algorithm and the results of the steady state BTE for phonons in silicon to studying the heat transport. In this section, we will follow the same procedure to analyze the thermal conductance in ballistic point contacts of GaAs which are short enough to achieve quasi-ballistic or even ballistic heat transport.

Recently, in 2011, Bartsch et al. [Bartsch11] demonstrated the fabrication of air-gap heterostructures for GaAs ultra short pillars with a diameter of 100 nm. The lengths of these pillars, between GaAs substrate and the capping layers, are 4 nm and 6 nm. They measured a thermal conductance reduced by several orders of magnitude with respect to the bulk value in GaAs. They explained these results by assuming that the phonon current through the pillars is not influenced by phonon scattering, as in perfect ballistic point contacts.

In this section, by solving numerically the BTE we will compare the results obtained depending on whether scattering mechanisms are included or not. Realistic acoustic phonon dispersion in GaAs is included. The scattering parameters are tuned to fit the thermal conductivity in bulk GaAs. In order to investigate the thermal conductance of nanometer long pillars, LA and TA phonon occupations at different temperatures are considered. We show that at ambient temperature, some scattering events occur even in 4 nm long pillars. This reduces the thermal conductance of pillar as measured in the ref. [Bartsch12], which over-estimates the ballistic prediction at high temperature.

5.1. Dispersion relation and scattering parameters

In this work, we use the sine type approximation for acoustic phonon dispersion in bulk GaAs cf. ref. [Strauch90]. The considered dispersion is:

$$\omega_s(q) = \omega_s^{\max} \sin\left(\frac{qa}{4}\right), \tag{2.47}$$

where ω is the pulsation, q is wave vector norm, a is the lattice constant and the maximum phonon frequency is ω_s^{max}. The values of ω_s^{max} are taken from ref. [Blackemore82]. The

optical phonons are neglected because of their low velocities and high activation energies [Chen98] as in Bartsch *et al.*

For bulk GaAs samples, the RTA is employed. Using the same scattering model proposed by Holland as in the Si case, we describe scattering mechanisms as [Holland63]:

- For LA: $\tau_{NU} = B_L \omega^2 T^3$ $\left(\text{LA, Umklapp} + \text{Umklappp processes}\right)$
- For TA:
  - $\tau_N^{-1} = B_{TN} \omega T^4$ $\left(\text{TA, Normal process}\right)$
  - $\tau_U^{-1} = B_{TU} \omega^2 / \sinh\left(\frac{\hbar\omega}{k_B T}\right)$ $\left(\text{TA, Umklapp process for } \omega > \omega_{1/2}\right)$
- Point defect scattering: $\tau_i^{-1} = A\omega^4$.
- Crystalline boundary scattering: $\tau_B^{-1} = v_g / \left(L \times F\right)$

B_L, B_{TN}, B_{TU}, A, L and F are adjusted to match the measured data for bulk samples in ref. [Holland64]. Here, the parameter set is: $B_L = 6.8\times10^{-24}$ sK^{-3}, $B_T = 1.98\times10^{-11}$ K^{-4}, $B_{TU} = 4.58\times10^{-18}$ s, $A = 1.25\times10^{-44}$ s^{-3}, $L = 0.51\times10^{-2}$ m and $F = 0.68$. As seen in Fig. 2.32, the fit matches very well the experimental data from 2 K to 300 K.

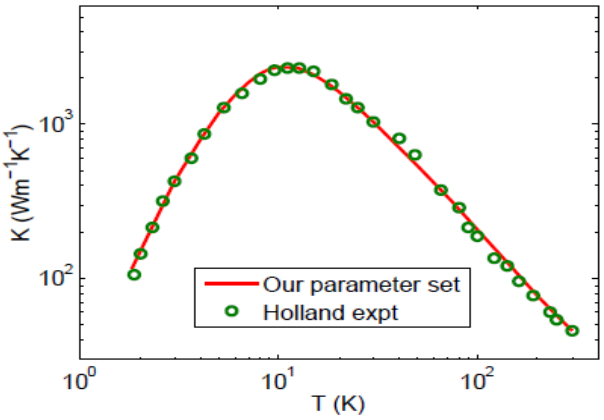

Fig. 2.32. Thermal conductivity as a function of the temperature in bulk GaAs. Our scattering parameters (continued curve). Measurement from ref. [Holland64].

The nanopillar is illustrated in Fig. 2.33. The cross-plane phonon-boundary scattering is considered diffusive and should be added. Its relaxation time is given by

$$\tau_b = \frac{D_{pillar}}{v_{cross-plane}}, \tag{2.48}$$

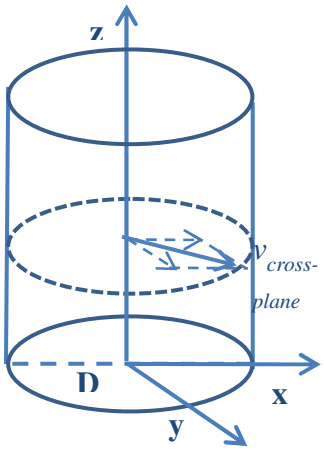

Fig. 2.33. Studied pillar structure and the used coordinates.

Where the pillar diameter D_{pillar} = 100 nm [Bartsch12] and $v_{cross\text{-}plane}$ is the in-plane group velocity defined as $v_{cross-plane} = \sqrt{v_{gx}^2 + v_{gy}^2}$. The total relaxation time is given by the Matthiessen's rule.

5.2 Results and discussion

To discuss the hypotheses of purely ballistic thermal conductance at point contacts in ref. [Bartsch12], the thermal conductance per unit area is calculated for several cases: (i) fully ballistic and (ii) ballistic in the in-plane direction with cross-plane boundary scattering because D_{pillar} is much longer than L_{pillar}. Both 4 nm- and 6 nm-long nanopillars are investigated. It is clear that the area conductance in the pure ballistic case is the highest and the cross-plane boundary scattering in these quite large diameter pillars (D = 100 nm) slightly influences the heat conduction. In all cases below 100K all models are equivalent in terms of conductance, see Fig. 2.34 (with the same cross section) as the transport is quasi-ballistic and length-independent. At higher temperature, the difference can be explained by difference in phonon transport regime (diffusive effects rise). The corresponding thermal conductivities (normalized by length) are shown in Fig. 2.34b for these pillars. These conductivities are much smaller than the GaAs bulk value of 46 $Wm^{-1}K^{-1}$.

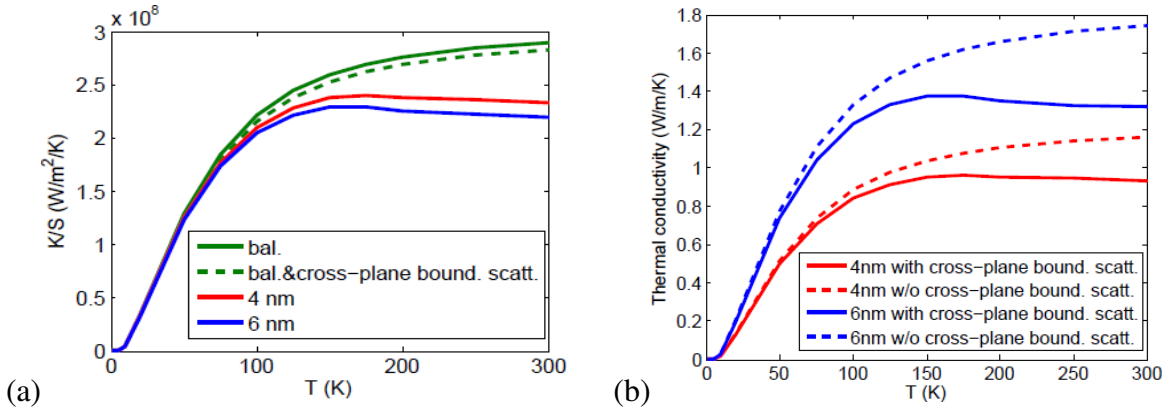

Fig. 2.34. (a) Thermal conductance per area in various cases: pure ballistic, ballistic in the in-plane direction with the cross-plane boundary scattering and for 4 nm- and 6 nm long pillars with realistic scattering for LA and TA. (b) Thermal conductivities in 4nm- and 6nm-long with and without the cross-plane boundary scattering.

To illustrate the ballistic phonon transport, the strongly asymmetric LA and TA phonon distribution in 6 nm-long pillars with a temperature difference $\Delta T = T_h - T_c = 20$ K are shown in Fig. 2.35.

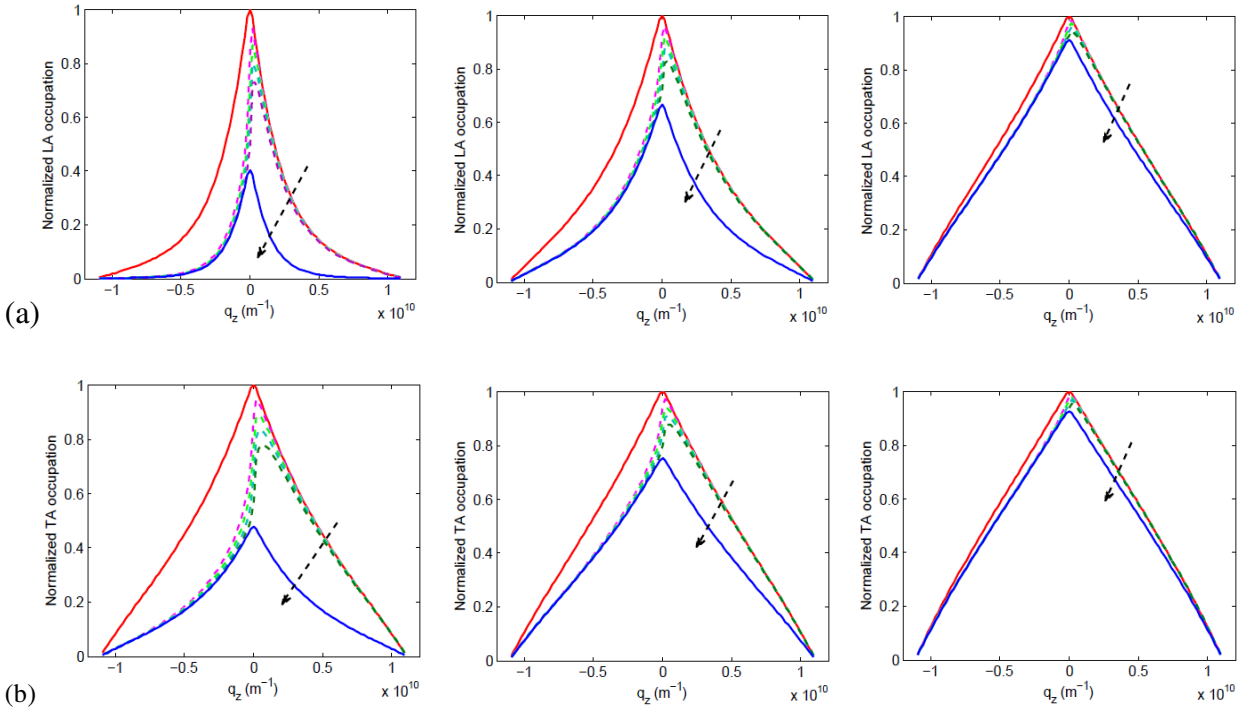

Fig. 2.35. Phonon distribution in the 6 nm long pillar with T_h and T_c = [60 K, 40 K], [110 K, 90 K] and [310 K, 290 K], from left to right respectively. The normalization is done with respect to the phonon occupation at the hot temperature T_h. (a) LA phonon and (b) TA phonon. The arrow is to indicate from hot to cold side.

Fig. 2.36 shows the simulated thermal conductance of a single pillar and the data from Ref. [Bartsch12]. For a 4 nm-long pillar, the calculated conductance matches very well the experimental one. Even at ambient temperature, the ballistic regime is dominant.

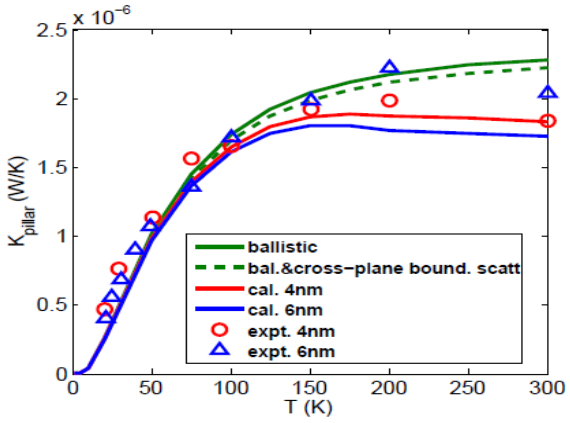

Fig. 2.36. Thermal conductance of single pillar: pure ballistic (continued green line), only with cross-plane boundary scattering (dashed green line), with scattering in 4 nm (red line) and 6 nm (blue line) long pillars in comparing with the experimental data for 4 nm (red circles) and 6 nm (blue triangles) long pillars.

At ambient temperature [310 K, 290 K], some diffusive effects take place, but the conductance remains very close to the ballistic one.

The experimental data are extracted by adjusting the pillar density to match the computed conductance of one single pillar. With the sine-type phonon dispersion and purely ballistic model, Bartsch *et al.* found a pillar density of 6.4 μm^2 for 4 nm-long pillars and 3.75 μm^2 for 6 nm-long pillars. Those obtained by using the sine-type phonon dispersion and the quasi-ballistic model in ref. [Jeong12] give respectively the densities of 3.7 μm^2 and 2.5 μm^2. In our work, in the model with all scattering mechanisms, the extracted densities are 6.4 μm^2 for 4 nm-long pillars and 4.2 μm^2 for 6 nm-long pillars. The slight difference is due to the non-negligible presence of scattering over the distance of 6 nm.

5.3 Conclusion

In this section, we showed that our BTE solver using the RTA approximation with sine type phonon dispersion and relevant set of scattering parameters could be used successfully to predict the thermal conductance in ultrashort GaAs nano-pillars. The ballistic phonon transport dominates clearly the thermal conductivity in nanometer-long pillars, additionally the thermal conductivity is slightly affected by scattering at temperatures higher than 100 K.

6. CONCLUSIONS OF CHAPTER

In this chapter, a relevant set of scattering parameters and phonon dispersions have been introduced to reproduce the thermal conductivity of Si and GaAs bulk material. Normal and Umklapp phonon-phonon, impurity and boundary scatterings have been described. Our own model of optical phonon's decay into acoustic phonons was established.

Besides, an analytic model has been used to fit the thermal conductivity and tune the scattering parameters. The phonon-boundary scattering in various device geometries can be easily included in our model. Our results capture well the trend of thermal conductivity in films and in square and circular cross-section wires. Finally, our analytical model was successfully used to fit experimental thermal conductivities in square wires by using realistic roughness.

Next, an original numerical method to solve the stationary BTE for phonons under RTA has been presented. All heat transport regimes can be investigated with our versatile numerical solver: diffusive, quasi-ballistic and ballistic regimes. Numerical predictions of heat conduction coefficient exhibit a very close match with experimental data for silicon and GaAs. The in-plane and cross-plane conductivities in Si thin films are also calculated. The results are in good agreement with the experimental measurements and other theoretical approaches.

Chapter III: PHONON GENERATION AND SELF-HEATING IN NANODEVICE

1. GENERATION OF PHONON

To simulate the electronic transport in Silicon, an analytic band approximation is used for the electron dispersion in this version of our simulator MONACO, as described in chapter 1.

1.1. Electron – phonon scattering

The electron-phonon scattering is separated into two of type interactions: intra-valley and inter-valley. In this work, we assume intra-valley scattering to be elastic (i.e. without energy exchange), while inter-valley phonon scattering is considered to be inelastic, i.e. electrons gain or loss the energy of the phonon exchanged at each event depending on whether the phonon is absorbed or emitted.

1.1.1. Intra-valley scattering

If the final and initial states, electrons are in the same band minimum and the energy exchange between two electron states Δε is very small in comparison with the mean electron energy $\overline{\varepsilon}_k$ at room temperature, we can neglect this energy exchange and consider this scattering mechanism to be elastic.

We take the isotropic approximation for the deformation potential D_{ac} [Conwell67] and the average longitudinal velocity u_l corresponding to the spherical symmetry. The scattering rate writes [HDRDollfus99]:

$$\lambda_{ac}(\varepsilon) = \frac{q^{7/2}}{\pi\sqrt{2}} \frac{k_B T m_D^{3/2} D_{ac}^2}{\hbar^4 \rho v_p^2} \sqrt{\varepsilon} \,. \tag{3.1}$$

where is k_B the Boltzmann constant, $m_D = m_0 \sqrt[3]{m_t^2 m_l}$ is the effective mass in the final valley, v_p is the longitudinal (or transverse) wave velocity, ρ is the mass density, ε is the electron kinetic energy.

1.1.2. Inter-valley scattering

Because of the location of the conduction-band minima in the Brillouin zone, there are two types of inter-valley transitions: scattering between valleys of axes perpendicular to each other (*f*-process) and between valleys on the same axis (*g*-process). The full spectrum of intervalley phonons has been established by Asche et Sarbei [Asche81]. Since $\vec{k}_0 = 0.855 \times \vec{G}^{\langle 100 \rangle}$, both processes lead to a final $\vec{k}$ outside the initial Brillouin zone, i.e. they are Umklapp processes. Taking the Umklapp reciprocal lattice vectors $\vec{k}_g = 2\pi / a \langle 2\ 0\ 0 \rangle$ and $\vec{k}_f = 2\pi / a \langle 1\ 1\ 1 \rangle$ yields $\vec{q}_g = 2\pi / a \langle 0.29\ 0\ 0 \rangle$ and $\vec{q}_f = 2\pi / a \langle 0.145\ 0.145\ 1 \rangle$, respectively. The phonon involved in *g*-scattering has its wave vector $\vec{q}_g$ along a direction [100] and the phonon involved in *f*-scattering has its wave vector $\vec{k}_f$ about 11° off the direction [100] [Long60].

1.1.2a. Zero-order scattering

In most cases the transition matrix element is proportional to $D_{iv} = D_0$, where D_0 has the dimension of energy per unit of length and is independent of the phonon wave vector. The corresponding zero-order scattering rate writes [HDRDollfus99]:

$$\lambda_{iv0}(\varepsilon) = \frac{q^{3/2}}{\sqrt{2}\pi} \frac{Z_{iv}}{\hbar^2} \frac{m_D^{3/2} D_0^2}{\rho \hbar \omega_{iv}} \left[N_p + \frac{1}{2} - \frac{i}{2} \right] \sqrt{\varepsilon + i\hbar\omega_{iv} + \Delta\varepsilon_{iv}} \times \sqrt{1 + \alpha(\varepsilon + i\hbar\omega + \Delta\varepsilon_{iv})} \left[1 + 2\alpha(\varepsilon + i\hbar\omega + \Delta\varepsilon_{iv}) \right] , \quad (3.2)$$

where i =1 for one absorption, i = -1 for one emission, and N_p is the phonon occupation. Under equilibrium conditions, this term is governed by the Bose-Einstein statistic. Z_{iv} is the number of available final valleys (4 for *f*-type and 1 for *g*-type scattering). ε is the energy of final state and $\Delta\varepsilon_{iv}$ is the energy difference between initial and final valleys.

Some zero-order intervalley processes with low-energy phonons are forbidden by selections rules [Streitwolf70] [Lax72]. However, many works have shown that such intervalley processes with these phonons actually occur [Long60] [Canali75] [Ferry76] [Jørgensen78]. To reconcile these points, it has been suggested that these processes may be described by a transition matrix element in first order of the phonon wave vector [Ferry76]. We follow this approach in MONACO.

In this case, the transition matrix element is proportional to $D_{iv} = D_1 \times q$, where D_1 has energy unit and q is the phonon wave vector. The first-order scattering writes [HDRPhi99]:

$$\lambda_{iv1}(\varepsilon) = \frac{\sqrt{2}q^{5/2}}{\pi}\frac{Z_{iv}}{\hbar^4}\frac{m_D^{5/2}D_1^2}{\rho\hbar\omega_{iv}}\left[N_p + \frac{1}{2} - \frac{i}{2}\right]\times(1+2\alpha\varepsilon')\sqrt{\varepsilon'(1+\alpha\varepsilon')}\left[\varepsilon'(1+\alpha\varepsilon') + \varepsilon(1+\alpha\varepsilon)\right], \quad (3.3)$$

where $\varepsilon' = \varepsilon + i\hbar\omega_{iv} + \Delta\varepsilon_{iv}$. ($i$=1 for an absorption, i=-1 for an emission).

All points of the iso-energy surface in the final ellipsoid are equally probable.

Finally, the six Δ-Δ intervalley phonons identified in [Asche81] are taken into account [HDRDollfus99]. The energy of these phonons is listed in Table 3.1 together with the corresponding deformation potentials [HDRDollfus99]. Note that the set of deformation potentials is empirically determined to fit experimental results and is not unique: a wide range of values have been reported over the past four decades.

Transition	*Symbol*	*Value*	*Units*
g_1 (g-TA)	$\hbar\omega$	11.4	meV
	D_1	3.0	eV
g_2 (g-LA)	$\hbar\omega$	18.8	meV
	D_1	3.0	eV
g_3 (g-LO)	$\hbar\omega$	63.2	meV
	D_0	3.4	10^8 eV/cm
f_1 (f-TA)	$\hbar\omega$	21.9	meV
	D_1	3.0	eV
f_2 (f-LA)	$\hbar\omega$	46.3	meV
	D_0	3.4	10^8 eV/cm
f_3 (f-TO)	$\hbar\omega$	59.1	meV
	D_0	3.4	10^8 eV/cm

Table 3.1. Characteristics of electrons intervalley Δ-Δ transitions in Si used in this work [HDRPhi99].

Our phonon energies set is illustrated in Fig. 3.1a. In the simulation, when the type of inter-valley scattering mechanism is selected, the state of the electron in the final valley is chosen randomly.

1.1.2b. Phonon dispersion

As in traditional MC model, the phonon dispersions used to efficiently compute the scattering rates are wave vector independent as seen in Fig. 3.1a and are reported in Table 3.1. The phonon wave vector involved in the transition can be calculated as $\vec{q}=\vec{k}'-\vec{k}$, where $\vec{k}$ and $\vec{k}'$ are the electron wave vector in the initial and final states, respectively.

In this work, the phonon energy is afterward computed by using the previous wave vector $\vec{q}=\vec{k}'-\vec{k}$ but by considering in the first Brillouin zone the quadratic dispersion $\hbar\omega(q)$ plotted in Fig. 3.1b (cf. Eq. 2.8). This procedure is applied for both acoustic and optical phonons. The resulting phonon energies are spread around the phonon energy implemented in the MC code. This approach does not intrinsically ensure energy conservation between electrons and phonons; this point must be checked later.

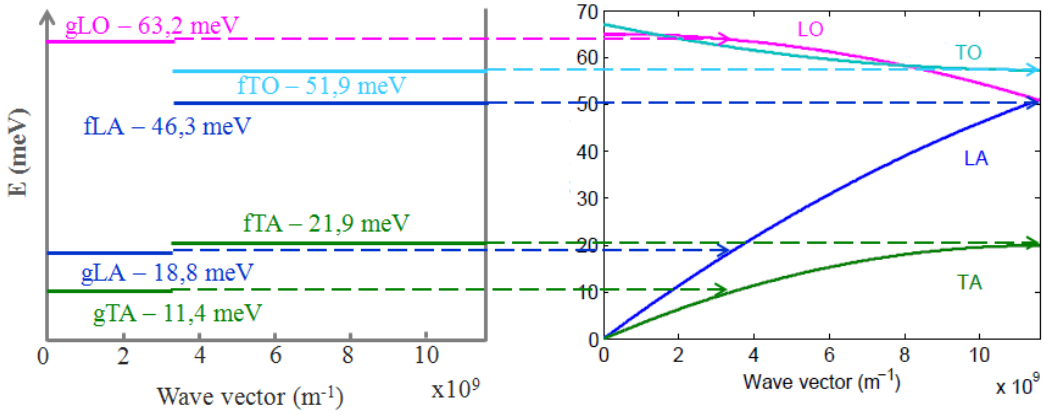

Fig.3.1. (a) Intervalley phonon energies used in MONACO. (b) Quadratic and isotropic phonon dispersion proposed by Pop *et al.* [PopJAP04]. Dashed lines indicate the energy and wave vector of the 6 types of scattering.

1.2. Phonon generation in bulk material

1.2.1. Monte Carlo generation vs. Joule effect

Here, simulations of electron transport in Silicon bulk material under uniform field are performed to compute the heat dissipation. During the simulation, all absorbed and emitted phonons are recorded. The net emitted phonon number is the difference between the numbers of emitted and absorbed phonons.

The heat generation rate per unit volume for each mode can be expressed as

$$G_{\vec{q},s}(\vec{r}) = \frac{\hbar\omega_{e-p}}{N_{sim}dt}\left(n^{em}_{\vec{q},s} - n^{ab}_{\vec{q},s}\right)\Big|_{\vec{r}} \ (\mathrm{W/cm^3}), \tag{3.4}$$

where $\hbar\omega_{e-p}$ is the energy of the phonon involved in the scattering process, N_{sim} is the number of simulated time steps, dt is the time step duration and $n^{em}_{\vec{q},s}$ and $n^{ab}_{\vec{q},s}$ correspond to the density of emitted and absorbed phonons of mode s and wave vector $\vec{q}$, respectively. Then, the total heat generation rate is obtained by summing the contribution of all modes as

$$G(\vec{r}) = \sum_{\vec{q},s} G_{\vec{q},s}(\vec{r}). \tag{3.5}$$

Fig. 3.2 illustrates the generated phonon spectra under low field (5 kV/cm) and high field (50 kV/cm).

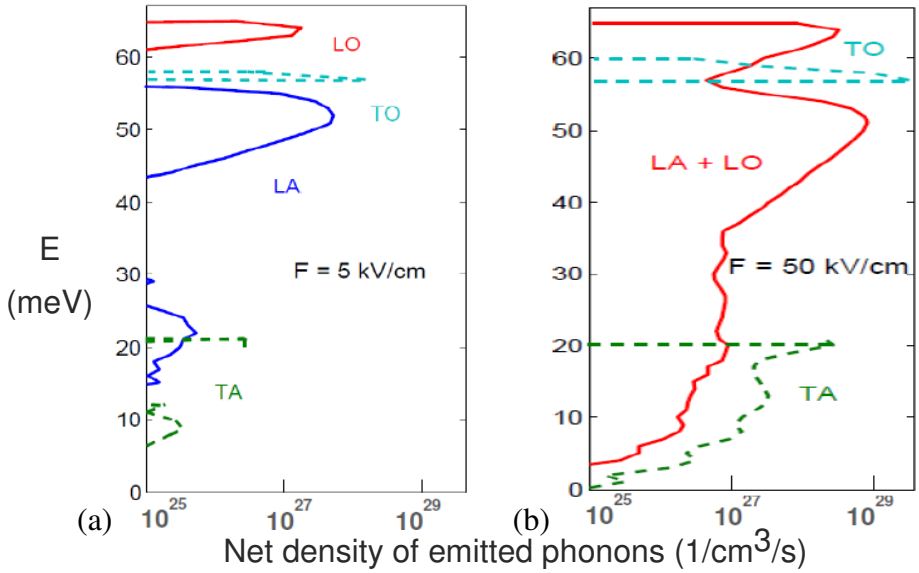

Fig. 3.2. Net density of emitted phonon in Si bulk under uniform field of (a) 5kV/cm and (b) 50kV/cm.

The number of acoustic phonons generated at low energy via intravalley process is small because the density of state of these phonons vanishes near the centre of Brillouin zone. Obviously, the strongest peaks of these spectra occur due to the *g*-type intervalley phonons at 30% of the BZ edge and to the f-type phonons at BZ edge. The relative magnitude of these peaks depends obviously on the choice of deformation potentials.

Fig. 3.3 shows the integrated net energy dissipations of each branch at various electric fields. With the set of deformation potential used here, the most important modes involved in

the dissipation process are LA and TO, up to more than 40% for all electric field. In addition, in steady-state regime, the sum of the four phonon mode contributions corresponds exactly to the Joule heating calculated as the scalar product of the current density $\vec{J}$ and the electric field $\vec{E}$ within the drift-diffusion approach. Thus, energy conservation is conserved in spite of our non-rigorous approach of the phonon dispersion.

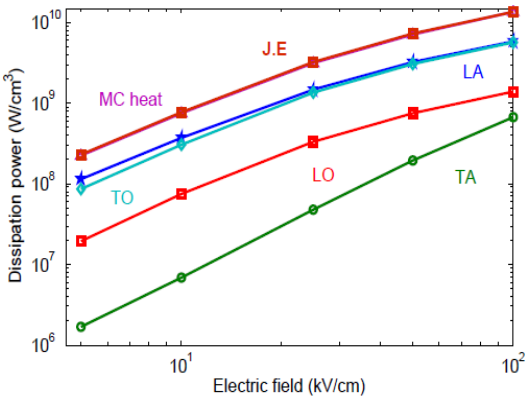

Fig. 3.3. Heat dissipation per mode as a function of electric field (TA: green line and circles, LA: blue line and stars, LO: red purple line and triangles, and TO: light blue line and diamonds) and comparison of total MC heat (purple symbols) with Joule effect (top red line).

1.2.2. Heat generation in DG-MOSFETs

Fig. 3.4 shows a 2D cross-section of a Si DG-MOSFET that has been used extensively in previous works based on the e-MC method [StMartin06, StMartin-Thesis05]. The device consists of three regions: the two access regions (source/channel) and the channel one. The source and drain extensions are doped to 5×10^{19} cm^{-3}. The source length is 50 nm, while the drain length is 150 nm. They are separated by a 20 nm lightly-doped (10^{15} cm^{-3}) channel region. The thickness of the Si-film is 20 nm. The dissymmetry of the device will be explained afterward.

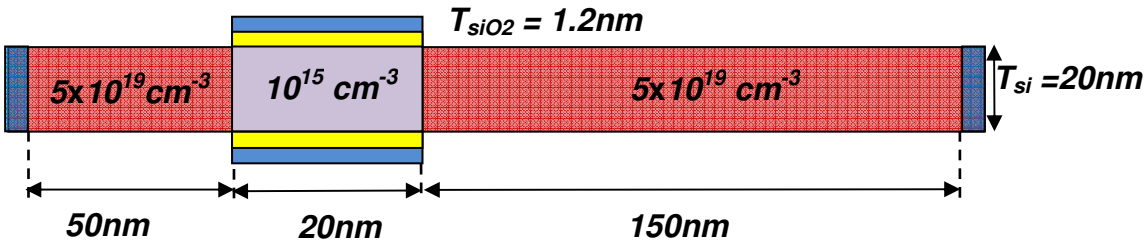

Fig. 3.4. Simulated device with three regions: source-channel-drain, which are doped uniformly of 5×1019cm-3, 1015cm-3 and 5×1019cm-3, respectively.

The electrical characteristics as potential energy (bottom of conduction-band) and effective electron temperature of electrons along this device at the steady-state for $V_{ds} = 0.5$ V are shown in Fig. 3.5.

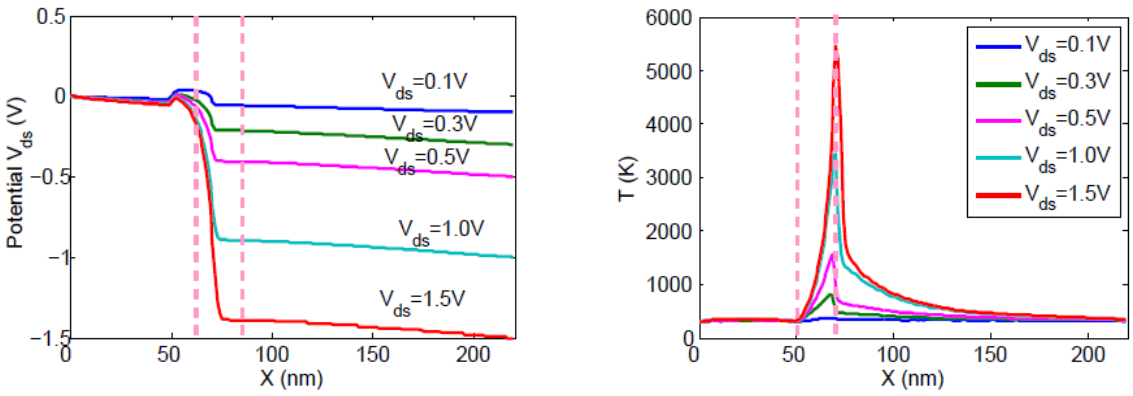

Fig. 3.5. Electrical characteristics in DG-MOSFET. (a) Potential energy (b) Effective electron temperature for various V_{ds} at $V_{gs} = 0.5$ V.

The net phonon generation rates in this device for each phonon mode can be extracted from MONACO simulations. To extract the net number of generated phonons during the electron transport, simulations of 1 picosecond are made for various bias conditions V_{gs} and V_{ds}. The phonon scattering rate for each phonon branch obviously depends on these two external bias that control the distribution of the electric field in the device.

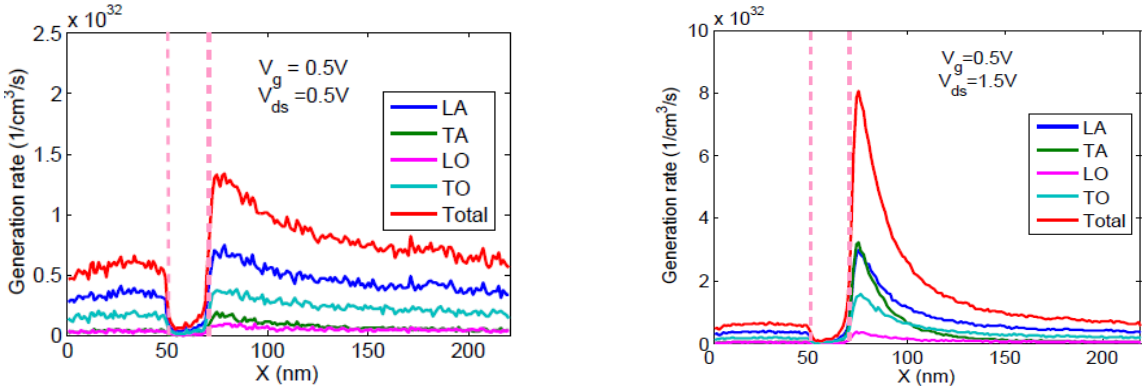

Fig. 3.6. Electron-phonon scattering-induced phonon generation rate per mode along the device for $V_{gs} = 0.5$ V and $V_{ds} = 0.5$ V (left) and $V_{ds} = 1.5$ V (right).

As seen in Fig. 3.6, the stronger electric field is (V_{ds} or/and V_g are more important), the more phonons are generated and the more is noticeably the "hot spot" point. For all biases, LA is the most frequently generated phonon, followed by TO. At low field ($V_{ds} = 0.5$ *V*), the TA and LO scattering rates are close, while under higher field ($V_{ds} = 1.5$ *V*), at the hotspot, TA scattering is more frequent than LO.

Obviously, for a given gate potential V_{gs}, the power density resulting from the total electron-phonon scattering rate depends on V_{ds}. In Fig. 3.7, with $V_{gs} = 0.5$ V, nearly all the power generation in this device structure occurs within the drain access, which is a common characteristic for transistor operating in the quasi-ballistic transport. In order to ensure the energy conservation in the device, the drain has been extended to allow the full electron energy relaxation within the drain, before reaching the contact. That is the reason behind the structure dissymmetry.

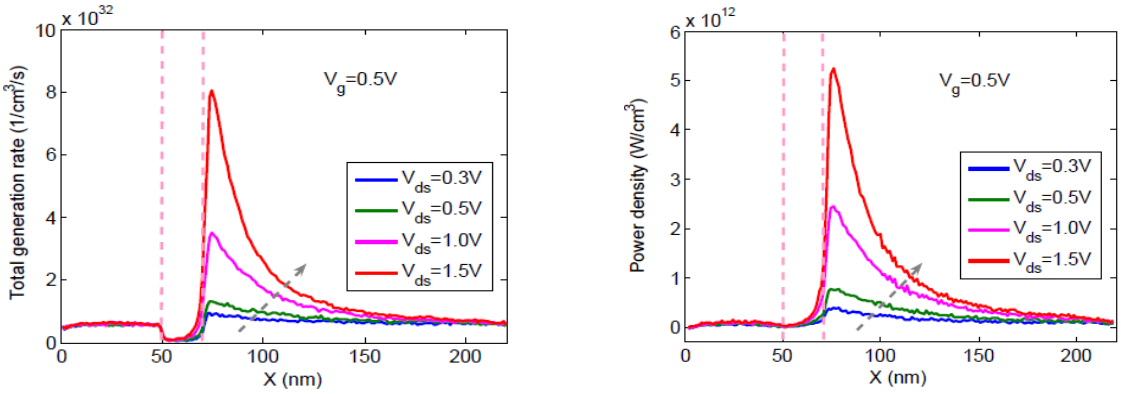

Fig. 3.7. (a) Total phonon generation rate vs. V_{ds} for $V_{gs} = 0.5$ V. (b) Power density for various V_{ds} at $V_{gs} = 0.5$ V.

Fig. 3.8 shows the spectrum of the energy distribution of the net phonon energy generation rate along the device with the bias conditions of $V_{gs} = 0.5$ V and $V_{ds} = 1.5$ V. Under high field, electrons can reach high energy and, then experience intervalley scattering. The phonon wave vectors resulting are in quite large range. As described above, the phonon energy is obtained here by using the quadratic dispersion, so the phonon are extended over a quite large range energy in the hot spot region.

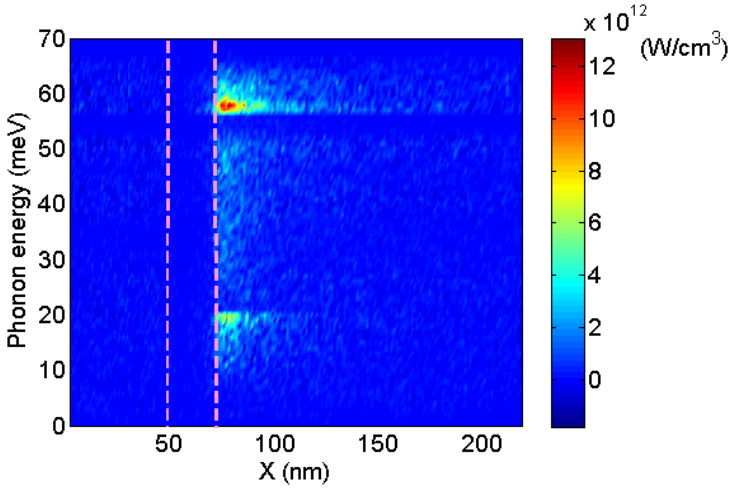

Fig. 3.8. Energy distribution of phonon energy generation rate along the device with $V_{gs} = 0.5$ V and $V_{ds} = 1.5$ V.

Now, we compare the heat dissipation obtained in this short device with the Joule heating extracted from the conventional macroscopic law $\vec{J}\cdot\vec{E}$. In what follows, Joule heating or Joule effect will refer to the macroscopic quantities calculated through the product $\vec{J}\cdot\vec{E}$, as opposed to the quantities calculated from the MC generation of phonons. The comparison of these power densities is shown in Fig. 3.9a for V_{gs} = 0.5 V and V_{ds} = 0.5 V, V_{ds} = 1.5 V.

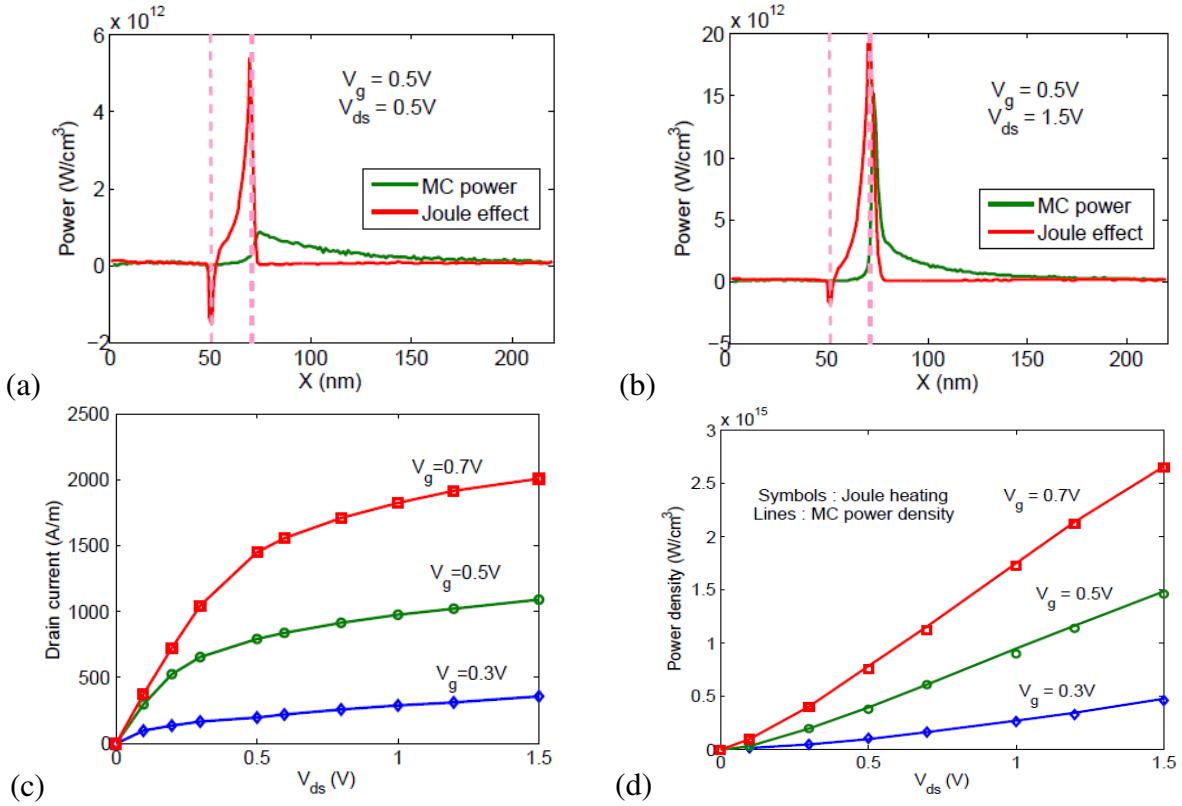

Fig. 3.9. (a,b) MC power density and Joule effect at V_{gs} = 0.5 V, V_{ds} = 0.5 V (a) and V_{ds} = 1.5 V (b). (c) Drain current as a function of V_{ds} for V_{gs} = 0.3 V (blue line), V_{gs} = 0.5 V (green line) and V_{gs} = 0.7 V. (d) Comparison between total MC power density (lines) and integrated Joule heating (symbols) at various bias conditions.

The discrepancy between the macroscopic and MC heat generation profiles is clear. While the macroscopic calculation leads to a maximum of dissipated heat at the drain-end of the channel where the field is high, the MC simulation shows that electrons lose their energies gradually in the drain extension after having been accelerated by the electric field in the channel. Therefore, the peak heating rate predicted by MC simulation occurs far into the drain extension, in contrast with the macroscopic prediction. For the sake of information, some drain current characteristics are shown in Fig. 3.9c, while the corresponding total generated

power density is plotted in Fig. 3.9d. Interestingly, Fig. 3.9d shows that even when non-equilibrium transport is strong the total MC heating and Joule heating are very close, i.e. the total electronic energy given gained in the electric field during the transport and transformed into phononic energy is the same in both cases. This means that the total energy in the system under simulation by our simulator is conserved. However, the MC heat generation model is clearly essential for accurate prediction of the mixture of electrons and phonons inside the drain "hot spot," which will be used in the next section as an input to a phonon transport model (p-BTE) at the sub-micron scale.

2. PHONON TRANSPORT IN 20NM-THICKNESS FILM DG-MOSFETs

In this Section, by using inputs from e-MC simulation, we investigate the thermal transport in the DG-MOSFET with the specific thickness of 20 nm as illustrated in Fig. 3.4 by solving the steady-state BTE described in Chapter 2 (Section 3).

This section is organized as follows: First, the evolution of the thermal conductivity of 20 nm-thickness films is extracted thanks to the p-BTE. Second, using this thermal conductivity evolution (for the evaluation of T_{scatt}, see chapter 2) and including the power dissipation and the LTO decay in the steady-state BTE, the temperature of the four phonon modes and also the effective temperature are obtained. Next, by comparing these temperatures and the diffusion temperature, we point out the limit of the macroscopic model, particularly at the hotspot. Additionally, we investigate the impact of Si-SiO_2 interface roughness on thermal transport in the device. Finally, the non-equilibrium phonon transport is evidenced.

2.1. Thermal conductivity of 20 nm-thick Si films

To inject consistent thermal conductivities as a function of temperature in the BTE model (evaluation of T_{scatt}, see Chapter 2, Section 3), the in-plane thermal conductivity of 20 nm-thick film is calculated preliminary by solving the pBTE including the roughness of the interface Si-SiO_2, as described in Chapter 2. In Fig. 3.10, the evolutions of the thermal conductivity with temperature from 300K to 800K for several roughness parameters are shown.

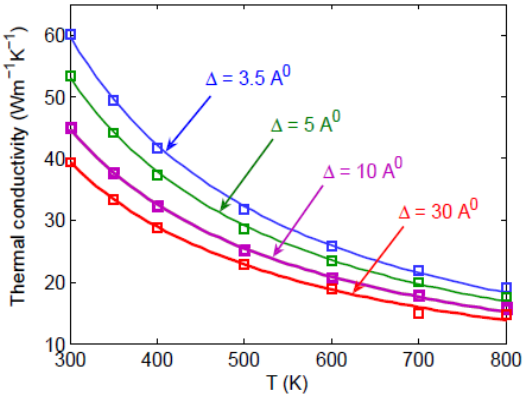

Fig. 3.10. Evolution of the thermal conductivity as a function of temperature in Si films of thickness 20 nm. The calculated conductivities are in symbols of the same colors as fitting curves $C \times T^{\alpha}$ for several roughness parameters: Δ = 3.5 Å (blue), 5 Å (green), 10 Å (purple) and 30 Å (red).

As expected, when increasing the temperature and the roughness, the thermal conductivity decreases. We suppose that the conductivity variation as a function of temperature is in the form $C \times T^{\alpha}$, like in the bulk case (see numerical BTE results of chapter 2). These evolution curves are illustrated in Fig. 3.10 with the calculated thermal conductivities in symbols. The values of C and α for each roughness are reported in table 3.2.

Parameters\Roughness	3.5Å	5Å	10Å	20Å	30Å
C (x10^4)	5.7693	4.1645	2.3766	1.6253	1.7432
α	-1.2053	-1.1689	-1.1006	-1.0511	-1.0684

Table 3.2. Parameters of the function $C \times T^{\alpha}$ used to fit the conductivity-temperature pBTE results for different roughness parameters.

2.2. Heat transport: Results and discussions

In this sub-section, we investigate the heat transport in the above DG-MOSFET structure at various bias conditions and with different roughness parameters. As shown in sub-Section 2.1, the thermal conductivity depends not only on the temperature but also on the roughness at the oxide-semiconductor interface that generates an additional component to the phonon-boundary scattering rate to be used to solve the pBTE in thin devices (see chapter 2, section 2.4.5). To solve the diffusive equation, the conductivity - temperature relations in the form $C \times T^{\alpha}$ determined in the previous sub-section for different roughness parameters are used.

First, we analyze the behavior of the effective temperature and of the temperature of four phonon modes (as defined in chapter 2, section 3.5). The temperature profiles in the DG-MOSFET under the bias condition $V_{gs} = 0.5$ V, $V_{ds} = 1.2$ V with the roughness $\Delta = 30$ Å are displayed in Fig. 3.11. Let us to point out the difference between phonon modes and also between the effective and diffusive (Fourier) temperatures, a zoom of the hotspot is also presented in Fig. 3.11b.

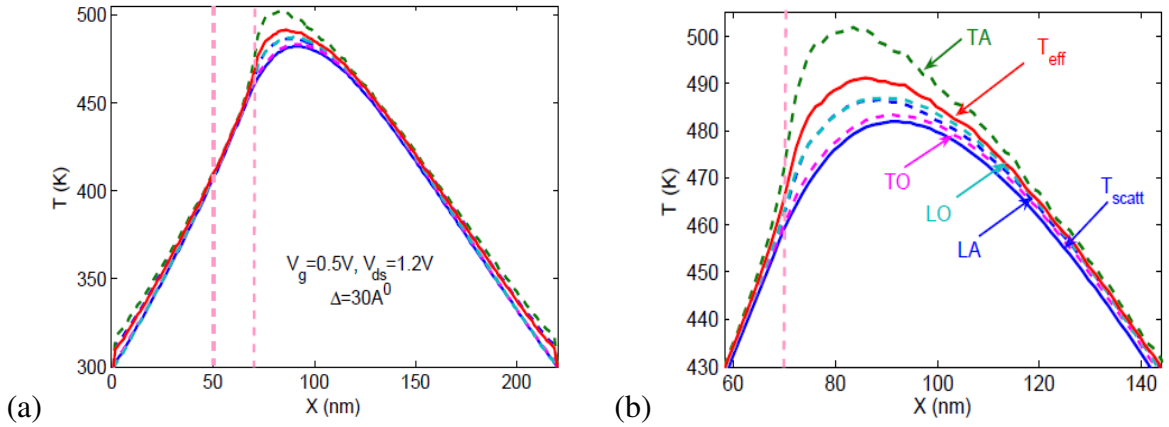

Fig. 3.11. (a)Temperature profiles along the DG-MOSFET under the bias condition $V_{gs} = 0.5$ V, $V_{ds} = 1.2$ V with roughness $\Delta = 30$ A°. (b) Zoom to point out the phonon-mode-temperature in the hotspot: LA (blue dashed line), TA (green dashed line), LO (azure dashed line), TO (purple dashed line); diffusion (scattering) temperature $T_{Fourier}$ (blue solid line) and effective temperature T_{eff} (red solid line). The same colors are used in the two graphs.

The phonon-modes and effective temperatures in this out of equilibrium regime are different in the channel-drain region where many phonons are generated by hot electrons. The LTO temperatures are slightly higher than the diffusion temperature in this region. However, the LTA phonon temperatures are very high because these phonons are generated simultaneously by electron – phonon scattering and by optical phonon decay, the latter mechanism being an important source of LTA phonons. Note that with our set of deformation potentials, the power density of LTO is up to about 50% of the total one (see Fig. 3.3). With the hypothesis that at steady-state, all LTO phonons decay into LA and TA phonons, the density of LA and TA phonons produced by this process is comparable to the density of LTO phonons (see Chapter 2, sub-section 2.3). In addition, the number of LTA phonons generated by LTO phonon decay is equally distributed between LA modes and TA modes, but at a given temperature the equilibrium phonon occupation number of TA modes is smaller than that of LA modes. Hence, the impact of LTO decay is stronger for TA phonons than for LA phonons,

which manifests through the TA temperature that is much higher than the LA temperature. This is the origin of the strong enhancement of the TA temperature in the hot spot region. The diffusive model underestimates the temperature (482.0 K at X = 91 nm) in the hotspot region compared to the effective temperature obtained by the BTE model (491.3 K at X = 86 nm). Along the transistor, this difference is visible in the zone from 70 nm (drain-end of the channel) to 95 nm where most of the power dissipation is produced (see Fig. 3.9).

Discontinuities of temperature near the isothermal boundaries are visible in Fig. 3.11a. These discontinuities were also seen in the Si bars (see Chapter 2, Section 4.7). The shorter the device is, the stronger the discontinuities at the boundaries are. This is in agreement with the work of Wong et al [Wong11]. They used Monte Carlo simulation for the phonon transport in silicon structures with heat generation in Gaussian form for films of length ranging from 10 nm to 5 µm and with a constant temperature of 300 K applied at both ends. They showed that the discontinuity was increased when the film was reduced below 100 nm due to the decreasing of thermal conductance.

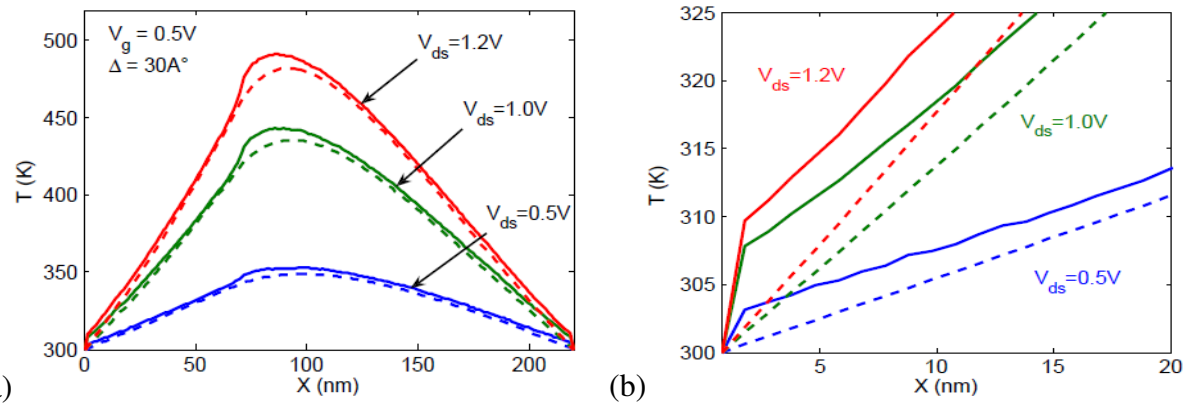

Fig. 3.12. (a) Bias dependence of temperature discontinuities at two ends and of temperature profiles with roughness $\Delta = 30$ Å and $V_g = 0.5$ V. Temperatures $T_{Fourier}$ and T_{eff} are plotted in dashed and solid lines, respectively at $V_{ds} = 0.5$ V (blue curves), $V_{ds} = 1.0$ V (green curves) and $V_{ds} = 1.2$ V (red curves). (b) Zoom at the right contact.

Fig. 3.12 shows that these discontinuities are increased when increasing the drain bias, i.e when increasing the power dissipation. At the source contact, the discontinuity of the effective temperature reaches 3.1 K at $V_{ds} = 0.5$ V, 7.8 K at $V_{ds} = 1.0$ V and 9.7 K at $V_{ds} = 1.2$ V. In addition, at high V_{ds}, the shift between the two temperatures increases in the hotspot.

Second, we analyze the heat flux which is expressed by Eq. 2.38 (see chapter 2, section 4.6). Here, we rewrite the flux expression in the form:

$$J_s(\vec{r}) = \sum_{\vec{q}} \hbar\omega(\vec{q},\vec{r}) \times v_{s,x}(\vec{q},\vec{r}) \times N_{s,x}(\vec{q},\vec{r}) \qquad \text{(2.38-chapter2)}$$

Where $v_{s,x}(\vec{q},\vec{r})$ and $N_{s,x}(\vec{q})$ are, respectively, the group velocity and the phonon density of the mode s with angular frequency ω at position x. $\hbar$ is the reduced Planck constant. The convention of group velocity sign is as follows: if the phonon travels from source (left side) to drain (right side), $v_{s,x}(\vec{q})$ takes the positive sign, and it takes the negative sign if the phonon comes from drain to source. The heat flux profile which corresponds to the above case (V_{gs} = 0.5 V, V_{ds} = 1.2 V and Δ = 30 Å) is shown in Fig. 3.13.

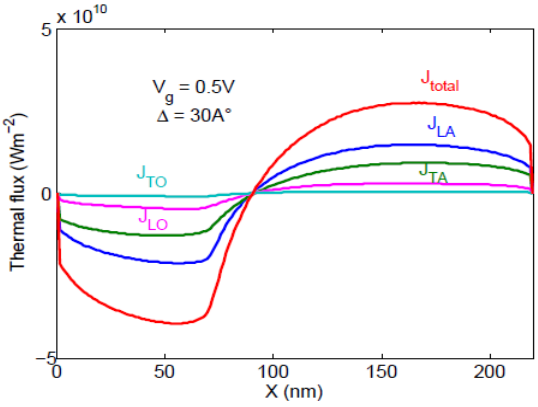

Fig. 3.13. Heat flux along the DG-MOSFET of each phonon mode (LA: blue line, TA: green line, LO : pink line and TO: azure line) and the heat flux total (red line).

According to the expression (Eq. 1.41) of the thermal flux, these curves behaves like the gradient of the temperature *(-dT/dx)*. Due to the fixed temperature of 300K at two ends and the isotropic hypothesis of phonon distribution, the heat fluxes at these points are zeros. When phonons reach the boundaries, they take immediately the velocity values at 300K. Therefore, the thermal flux falls very quickly to the zero value. In our model, the contribution of LO and TO modes to the heat transport is included by taking into account their group velocity. Hence, their fluxes are much smaller than that of the acoustic modes. Since the group velocity of LA mode is the highest, the heat carried by this mode is the most important.

Third, we investigate the impact of roughness on thermal transport. In Fig. 3.14, the power density is represented to highlight the relation between this quantity and the effective temperature. The total power density extracted from MC is shown (same as Fig. 3.9d). Three

roughnesses of 3.5 Å, 10 Å and 30 Å are compared. When increasing the roughness, the heat conduction is reduced, so that the highest hotspot temperature is observed in the roughest Si-SiO_2 interface case. For $V_{gs} = 0.3$ V (power density of about 10^{14} W/cm^3), the difference between the maximal values of effective temperature (position X_{max}) between the two cases of roughness 30 Å and 3.5 Å is 14.3 K (346 K vs. 332 K, respectively). For higher V_{gs} values of 0.5 V and 0.7 V (power density in the order of 10^{15} W/cm^3), the difference between 3.5 Å and 30 Å cases reaches 47.9 K and 97.2 K, respectively. Hence, the roughness effect plays a significant role at high power densities.

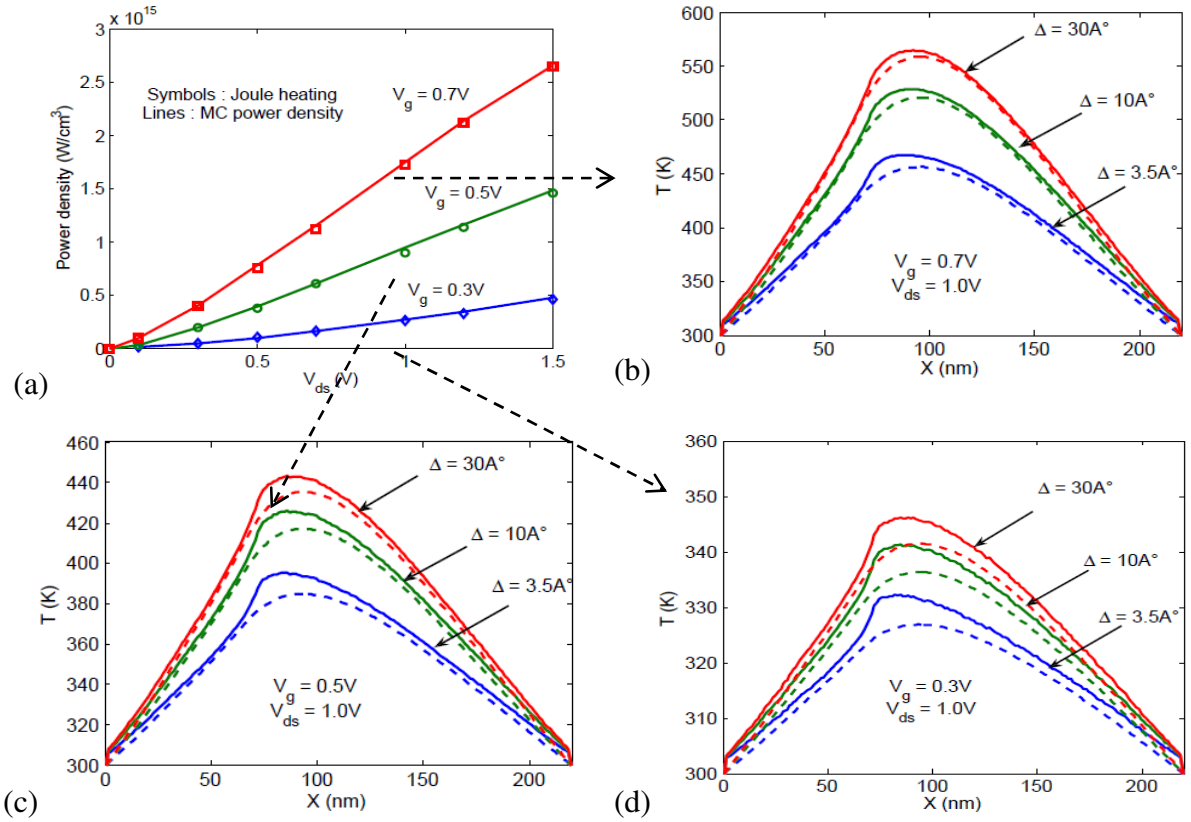

Fig. 3.14. Impact of roughness on the heat transport in the 20-nm-thick-Si-DG-MOSFET. (a) Total power density extracted from MC simulation (same as Fig. 3.9.d). (b,c,d) Effective temperature T_{eff} in solid lines, and "Fourier" temperatures $T_{Fourier}$ for different roughness parameters Δ and bias conditions.

Finally, we discuss the non-equilibrium aspects of phonon transport by investigating the non-symmetric phonon density distributions at the position $X_{max} = 86$ nm, i.e. in the hot spot, for $V_{gs} = 0.5$ V, $V_{ds} = 1.2$ V and $\Delta = 30$Å. We consider, successively, the cases of LA phonons, TA phonons, LO phonons and TO phonons in Fig. 3.15, Fig. 3.16, Fig. 3.17 and Fig. 3.18, respectively.

Here, to have the distribution as a function of energy, we have defined the phonon density distribution. As the phonon distribution in an interval of frequency [ω, ω+dω] depends on the width of this interval, following the Eq. 2.16 in chapter 2:

$$n(\omega)d\omega = \frac{1}{\exp\left(\frac{\hbar\omega}{k_B T}\right)} \cdot DOS(\omega)d\omega = \iiint_{\omega<\omega(\vec{q})<\omega+d\omega} \frac{1}{\exp\left(\frac{\hbar\omega(\vec{q})}{k_B T}\right)} \cdot \frac{d\vec{q}^3}{(2\pi)^3} \qquad \text{(Eq. 2.16)}$$

The phonon density distribution is defined as:

$$n(\omega) = \frac{n(\omega)d\omega}{d\omega} = \frac{\iiint_{\omega<\omega(\vec{q})<\omega+d\omega} \frac{1}{\exp\left(\frac{\hbar\omega(\vec{q})}{k_B T}\right)} \cdot \frac{d\vec{q}^3}{(2\pi)^3}}{d\omega} \qquad (3.6)$$

Hence, this density distribution is unchanged with the interval dω.

In Fig. 3.15a we plot the density excess of LA phonon density distribution deduced from the eMC results.

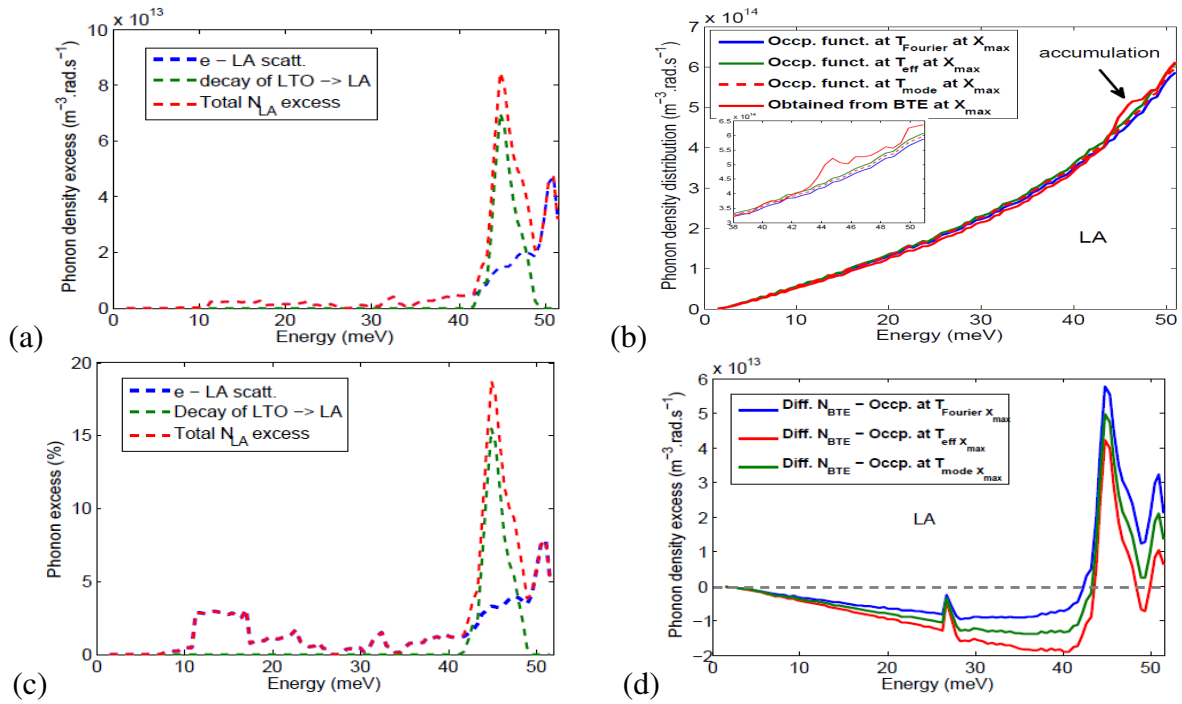

Fig. 3.15. Density distributions of LA phonons at the maximal temperature position X_{max} for $V_{gs} = 0.5$ V, $V_{ds} = 1.2$ V. (a) Distributions deduced from the eMC results with both contributions of e-ph scattering and optical phonon decay. The inset is the zoom from 38meV to 51meV. (b) Distribution obtained after solving the pBTE (red solid line), compared to the equilibrium density distribution at Fourier, effective and LA mode temperature. (c) Fraction (in %) of excess phonon distribution (from eMC) with respect to the equilibrium distribution at $T = T_{eff}$. (d) Difference between the pBTE distribution and the equilibrium distributions previously mentioned in (b).

We separate the distribution in two parts, one corresponding to the LA phonons due to electron-phonon scattering, and the other are corresponding to LA phonons resulting from LTO phonon decay (see sub-Section 2.3). The latter takes the form of a peak at $E = 43$ meV (see also Fig. 2.4, chapter II) while the former is characterized by a peak at $E = 50$ meV (see also Fig. 3.2). It appears that the contribution of LTO decay to the excess density distribution of LA phonons is more important than that of electron-LA phonon scattering. The relative excess due to these two mechanisms are about 15% and 8%, respectively (Fig. 3.15c) with respect to the equilibrium distribution at $T = T_{eff}$ determined after solving the pBTE (plotted in Fig. 3.15b). The total phonon density distribution of LA phonons obtained after solving the pBTE is plotted in Fig. 3.15b (red line). It is compared to the equilibrium distributions at the Fourier temperature ($T_{diff} = 480.7$ K), at the effective temperature ($T_{eff} = 491.3$ K) and at the LA mode temperature ($T_{LA} = 501.5$ K). The accumulation of LA phonons around 43 meV and 50 meV is again visible, and is even clearer in Fig. 3.15d in which we plot the difference between the pBTE result and the one of all these equilibrium distributions. Due to the fitting procedure used to extract the temperature, the integration of the phonon density distribution obtained from the BTE is equal to the equilibrium distribution at temperature T_{LA}. Hence, to compensate the excess for energy higher than 43 meV, the BTE distribution at low energy is lower than the equilibrium one.

The same quantities are plotted in Fig. 3.16 for the TA mode. There are two sources of TA phonon generation: the electron-TA phonon scattering which creates phonons mainly in the range 15 meV-20 meV, and the LTO decay (see Eq. 2.54 in chapter 2) which generates TA phonons between 17 meV and 20 meV (see Figs. 3.16a and 3.16c). Both resulting phonon distributions have a main peak at 20 meV. The total TA phonon excesses reaches to 35% at 20 meV. It explains the strong enhancement of the TA mode temperature in the hot spot (see Fig. 3.11).

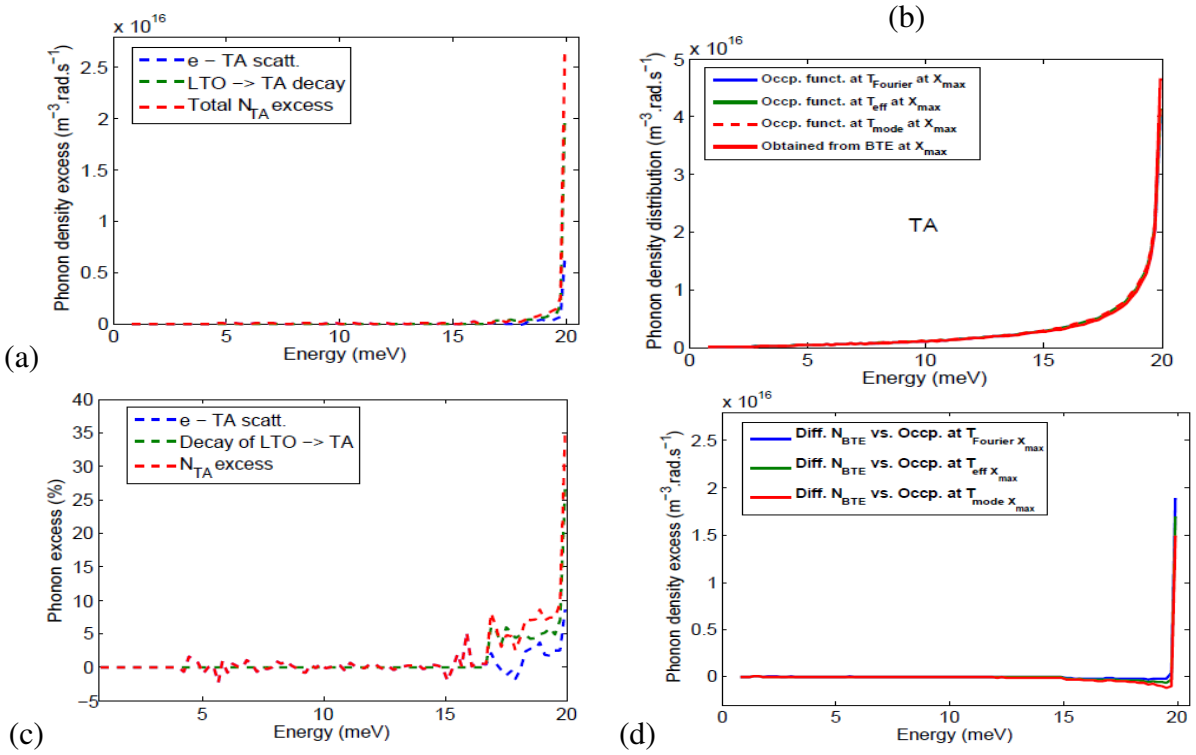

Fig. 3.16. Density distributions of TA phonons at the maximal temperature position X_{max} for $V_{gs} = 0.5$ V, $V_{ds} = 1.2$ V. (a) Distributions deduced from the eMC results with both contributions of e-ph scattering and optical phonon decay. (b) Distribution obtained after solving the pBTE (red solid line), compared to the equilibrium density distribution at Fourier, effective and TA mode temperature. (c) Fraction (in %) of excess phonon distribution (from eMC) with respect to the equilibrium distribution at $T = T_{eff}$. (d) Difference between the pBTE distribution and the equilibrium distributions previously mentioned in (b).

For LO and TO modes, there is only one generation term resulting from electron-phonon scattering (see Eq. 2.53-chapter 2). The LO mode generation and transport are analyzed in Fig. 3.17. As previously seen in Fig. 3.3, the excess of LO phonons contributes only to about 10% of the total dissipated power. Additionally, most of LO phonons are generated in the energy range 60 meV – 65 meV, where the equilibrium phonon distribution is small (see Fig. 3.17b). Therefore, though the LO phonon excess reaches about 15%, the LO mode temperature remains close to the Fourier temperature.

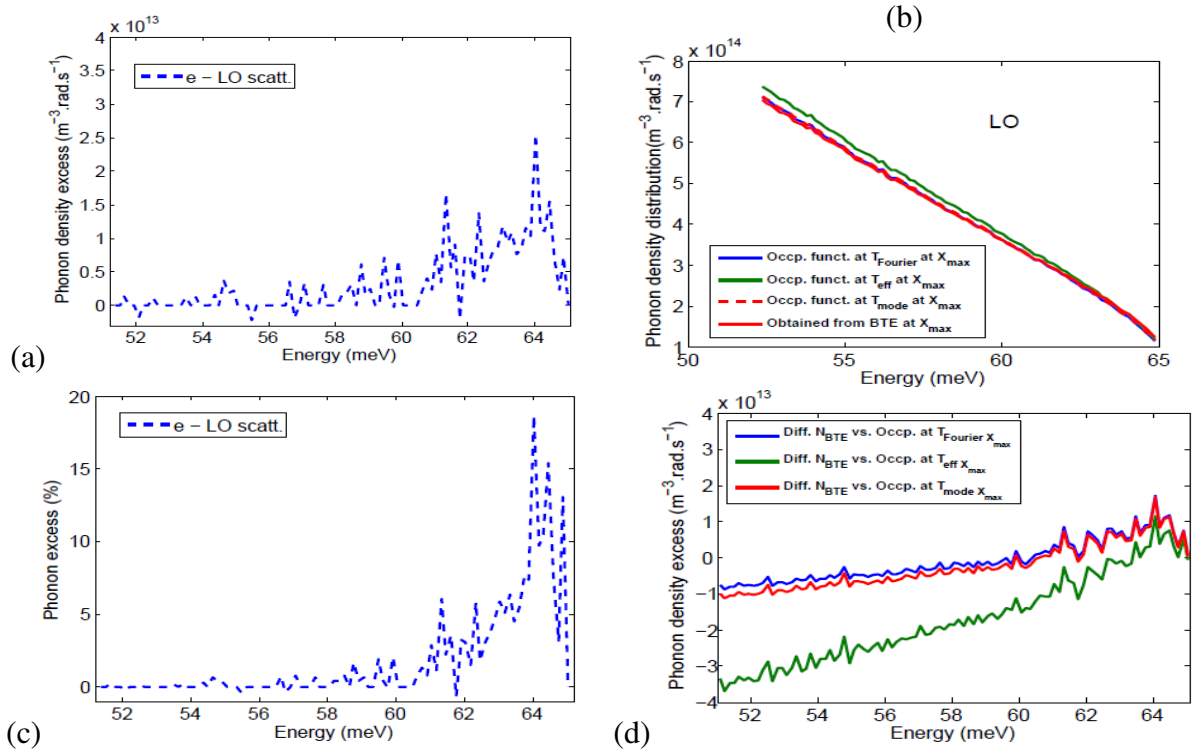

Fig. 3.17. Density distributions of LO phonons at the maximal temperature position X_{max} for $V_{gs} = 0.5$ V, $V_{ds} = 1.2$ V. (a) Distributions deduced from the eMC simulation via e-ph scattering. (b) Distribution obtained after solving the pBTE (red solid line), compared to the equilibrium density distribution at Fourier, effective and LO mode temperature. (c) Fraction (in %) of excess phonon distribution (from eMC) with respect to the equilibrium distribution at $T = T_{eff}$. (d) Difference between the pBTE distribution and the equilibrium distributions previously mentioned in (b).

The TO mode transport is analyzed in Fig. 3.18. Regarding the TO mode, it is worth noting that the excess generated phonon distribution is limited to 4%. Hence, though this f-type generation occurs around 57 meV, at which the TO phonon distribution is high, its effect on the temperature is small and the TO mode temperature remains close to the Fourier temperature T_{diff}, as we have seen previously in Fig. 3.11.

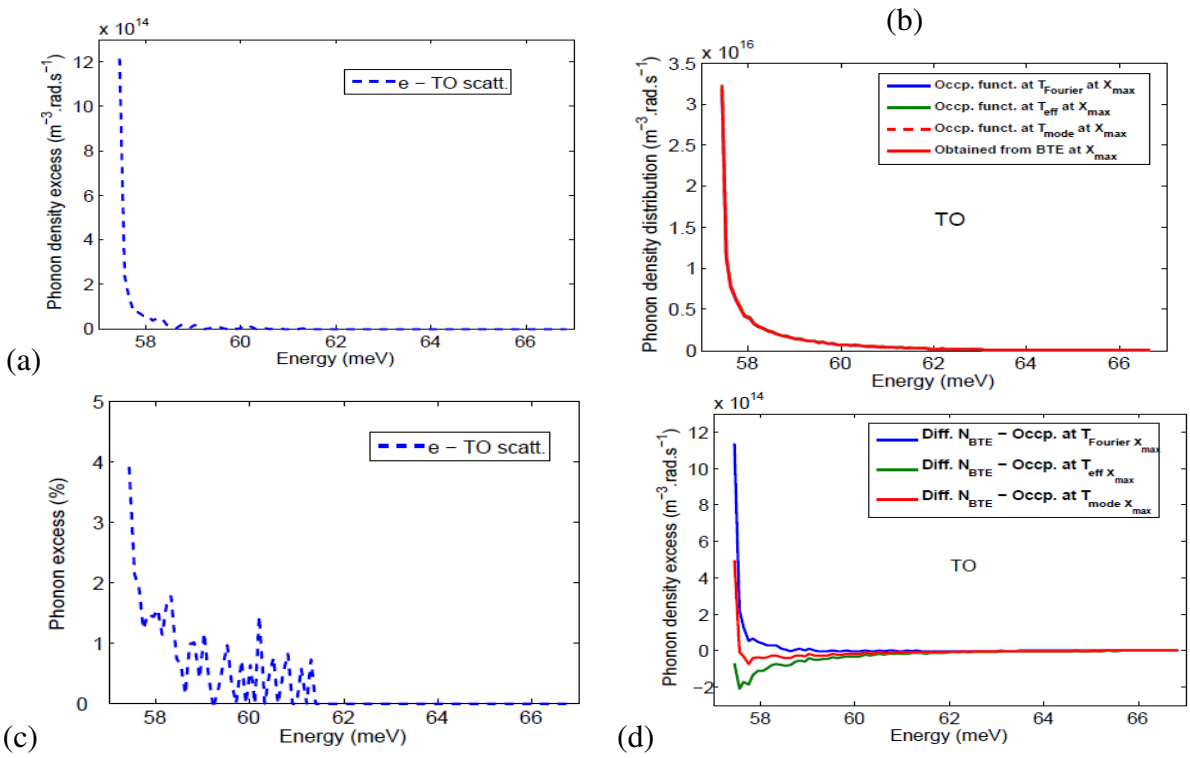

Fig. 3.18. Density distributions of TO phonons at the maximal temperature position X_{max} for $V_{gs} = 0.5$ V, $V_{ds} = 1.2$ V. (a) Distributions deduced from the eMC simulation via e-ph scattering. (b) Distribution obtained after solving the pBTE (red solid line), compared to the equilibrium density distribution at Fourier, effective and TO mode temperature. (c) Fraction (in %) of excess phonon distribution (from eMC) with respect to the equilibrium distribution at $T = T_{eff}$. (d) Difference between the pBTE distribution and the equilibrium distributions previously mentioned in (b).

3. SELF-HEATING IN DG-MOSFET WITH COUPLED NON-EQUILIBRIUM ELECTRON-PHONON TRANSPORT

3.1. Description of coupled electron-phonon transport simulation

To model the effects of self-heating in transistors, the electron and phonon transport must be coupled together. The coupled non-equilibrium electron-phonon transport in the studied DG-MOSFETs and its effects on the transport of each type of particle will be described in this section.

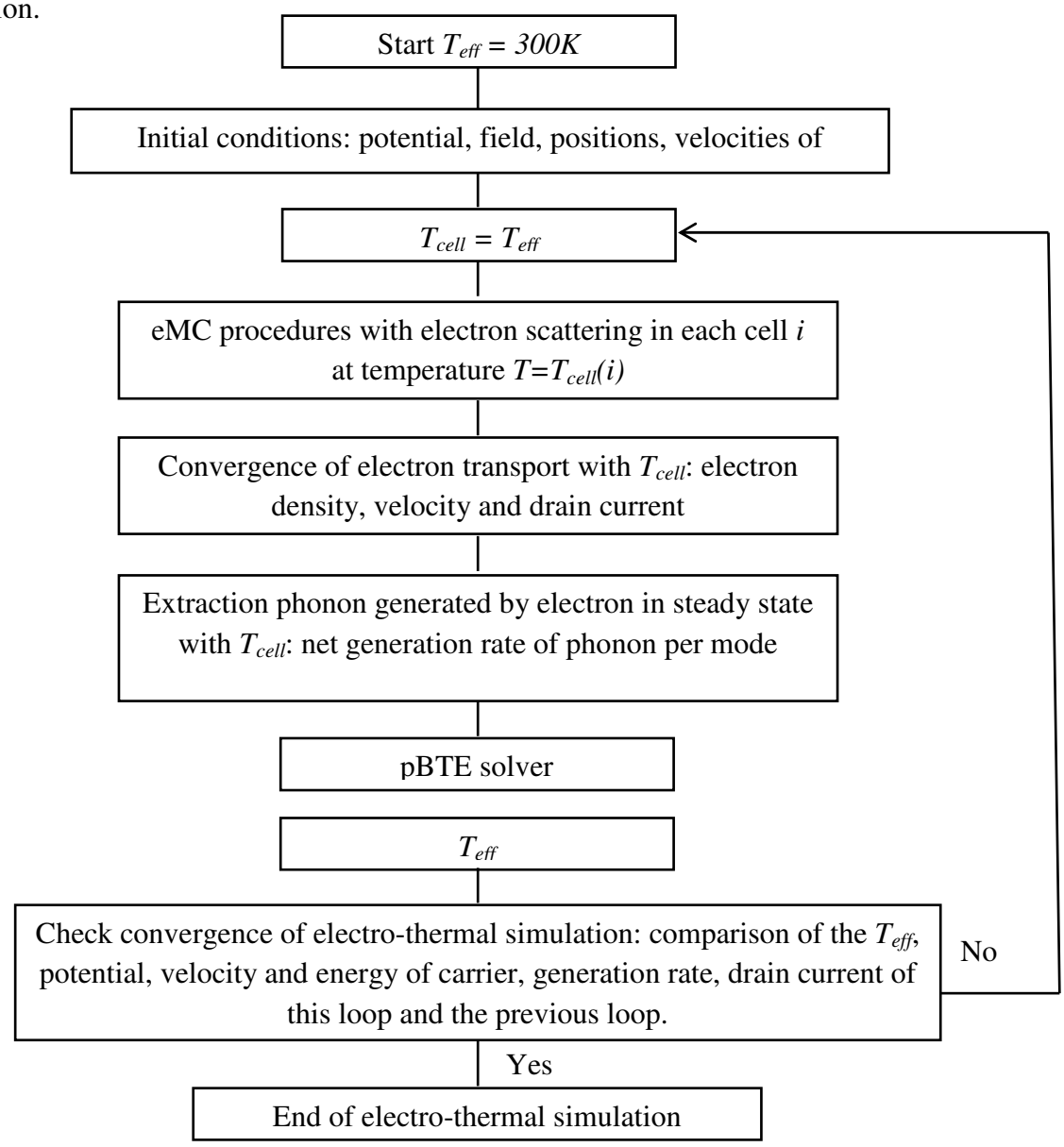

Fig. 3.19. Schema of the coupled electro-thermal simulation.

The schema of the procedure of the coupling electron and phonon transport simulation is illustrated in Fig. 3.19. The coupled simulation begins with an isothermal (300K) e-MC simulation (open loop). Net phonon generation rates as a function of position and the phonon frequency are extracted from e-MC and are used as inputs for the p-BTE solver that gives us the phonon temperatures. The resulting effective temperature is then re-injected in the e-MC simulator. As seen in the previous Section, each mode has its own temperature and the phonon distribution of each mode can be quite well approximated by the equilibrium distribution at temperature $T = T_{eff}$. Hence, we make this approximation for the lattice temperature. All electron scattering rates, as electron-phonon and electron-impurity scattering rates (see in ref. [Aubry-Fortuna04]), are re-calculated in each cell according to the position-dependent T_{eff}. Thus, the MC simulation is performed by taking into account the temperature effect. The electronic transport is modified through this field of temperature. Once the system reaches the stationary regime, the net phonon generation rates are extracted again and sent to the p-BTE solver. This two-step process, that successively includes an electron and a phonon transport simulation, is called a loop. After each loop, the potential, the drain current, the average velocity, the average energy of electrons and also the phonon generation rates are examined and compared with the previous loops until the convergence is reached. We have been empirically that by using this procedure, the convergence is reached after only three loops.

Then, the impact of self-heating on the electron transport in the 20 nm DG-MOSFET will be analyzed, through e.g. the drain current, the scattering location and the ballisticity. Regarding the effects on phonon transport, we will analyze mainly the temperature profiles. Finally, the effect of changing the roughness parameters (from 3.5Å to 30Å) in the phonon scattering rates will be analyzed too.

3.2. Convergence and influence of coupled non-equilibrium electron-phonon transport on the electronic and thermal transport

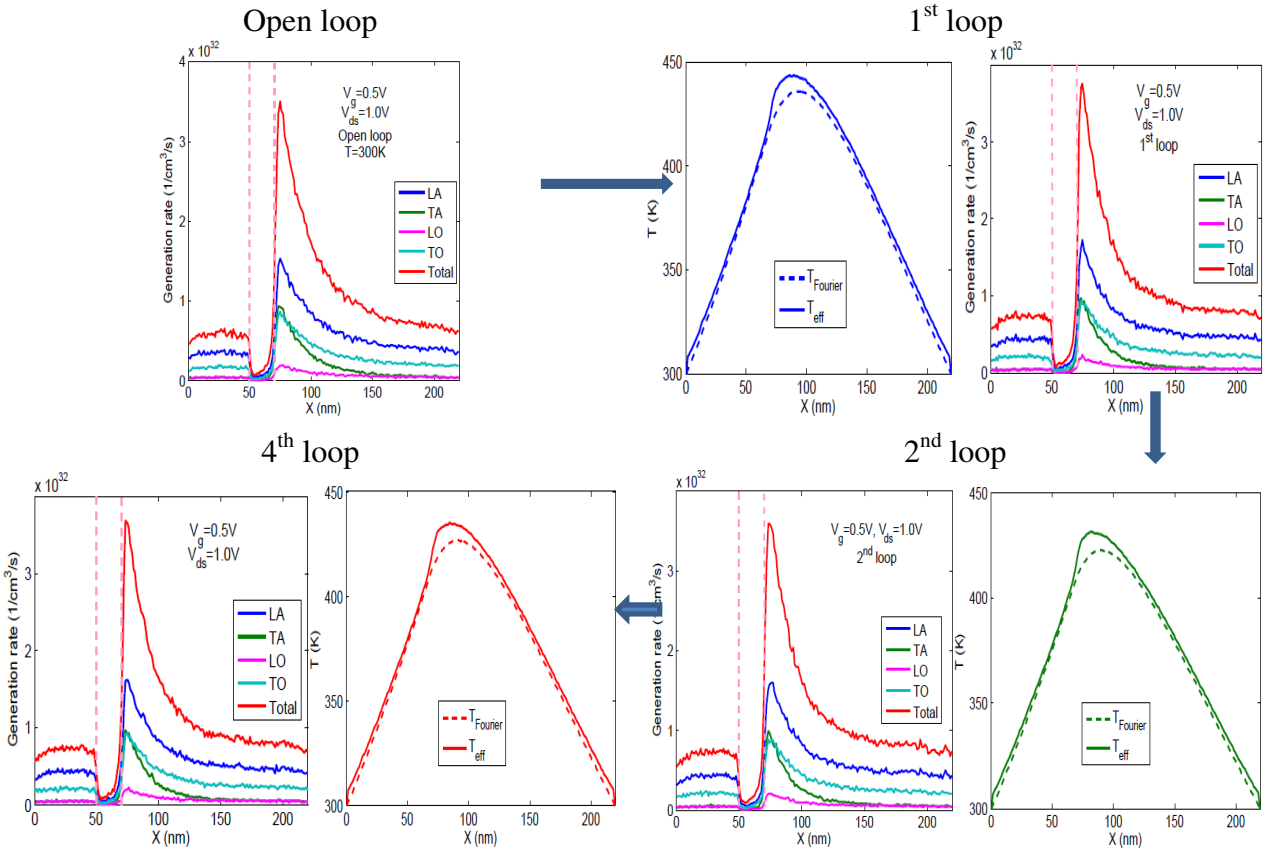

Fig. 3.20. Illustration of the coupled electron-phonon transport process in 20 channel length DG-MOSFET : net phonon generation rate and Fourier, effective temperature of each loop.

First, we analyze the convergence through the evolution of the temperature and the phonon generation rates after each loop for the 20 nm long channel DG-MOSFET. The results are summarized in Fig. 3.20.

From the open loop to the 1st loop, the phonon generation rates, or in other words, the electron-phonon scattering rates, are increased because of the temperature effect (see Eqs. 3.3 and 3.4). Then, from the 1st to the last loop (4th loop), these scattering rates are almost stable. Hence, the lattice temperature from the 3rd and 4th loop remains almost unchanged. In order to see clearly the convergence of the temperature, the Fourier and effective temperatures at $V_{gs} = 0.5$ V, $V_{ds} = 1.0$ V are put together in Fig. 3.21a. The corresponding thermal fluxes of each phonon mode and the total fluxes in the 1st and 4th (last) loop are shown in Fig. 3.21b.

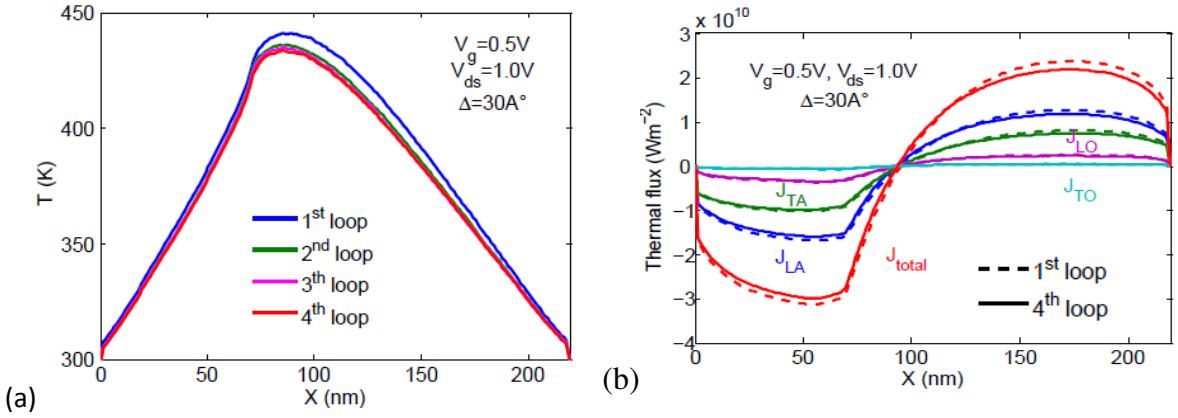

Fig.3.21. (a) Fourier (dashed lines) and effective (continued curves) temperatures along the device as a function of loop's number. (b) Thermal flux of each phonon mode and the total fluxes in the 1st and 4th loop.

In the coupled simulation, although the hot spot still exists, its magnitude is smaller when the self-heating is included. It induces smaller temperatures in the hotspot: the maximal value of the effective temperature in the 1st loop is 440.9 K, while this maximal value in the last loop (convergence value) is only 433.4 K. In addition, the thermal fluxes of each phonon mode and the total one in the last loop slightly decrease in comparison with the ones obtained in the open loop. This is due to the reduced temperatures of the 4th loop of the coupled simulation in comparison with the isothermal simulation (open-loop).

It is interesting to examine also the evolution of the potential. Fig. 3.22 displays the potential profile at $V_{gs} = 0.5$ V and $V_{ds} = 1.0$ V along the source-drain direction after different loops.

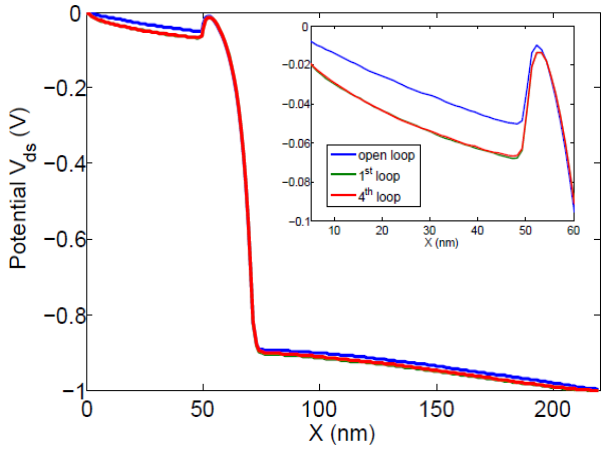

Fig. 3.22. Potential profile along the DGMOS for open loop (blue curve), 1st loop (green curve) and the last (4th) loop (red curve) at $V_{gs} = 0.5$ V, $V_{ds} = 1.0$ V.

The electrical resistances of the two accesses are increased in self consistent simulations due to the temperature increase in these regions. The inset shows the zoom of this potential from 0 nm to 60 nm (mid-channel). As the temperature rises, the electrical resistance increases, the potential is modified. We can see that a good convergence is reached after the first loop.

In addition, because of the raised of temperatures throughout the transistor, electrons are slowed down by scattering. To identify the most important scattering mechanisms, the number of electron interactions with impurities, intravalley acoustic and inter-valley phonons and roughness have been collected during 10,000 iterations of e-MC simulation in two cases: isothermal and electro-thermal case. In Fig. 3.23, we plot these interaction numbers in arbitrary units along the channel for V_{gs} = 0.5 V and V_{ds} = 1.0 V. The inter-valley interaction is the most increased scattering type. In particular, at the channel drain-end, this scattering type in coupled simulation is enhanced by 45.6 % in comparison with the case of isothermal simulation.

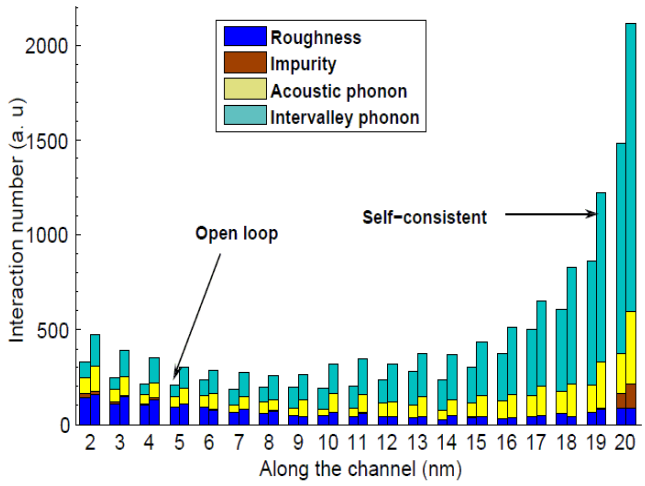

Fig. 3.23. Distribution of interaction number along the channel as a function of interaction types in DG-MOSFET at V_g=0.5V, V_{ds}=1.0V in both isothermal and electro-thermal case.

The increased scattering numbers along the device reduce the fraction of ballistic electrons that is quantified by the intrinsic ballisticity B_{int}. B_{int} corresponds to the percentage of purely ballistic electrons at the drain-end of the channel. The definition and the counting procedure in e-MC simulation are well detailed in ref. [StMartin04],[StMartin05]. In Fig. 3.24a, we plot the evolution of the percentage of ballistic electrons along the channel in two simulation cases

for the biases $V_{gs} = 0.5$ V, $V_{ds} = 0.5$ V and $V_{ds} = 1.0$ V. The reduction of intrinsic ballisticity B_{int} in coupled simulation for different biases V_{ds} is displayed in Fig. 3.24b.

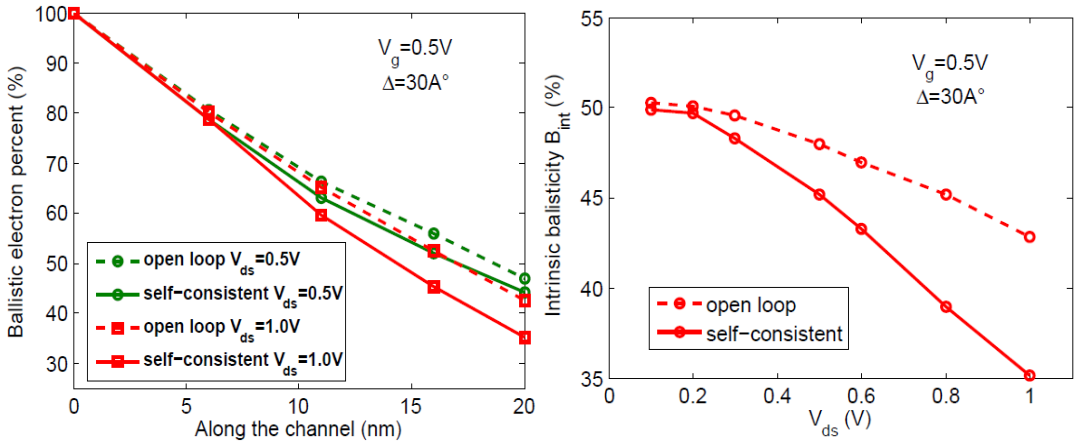

Fig. 3.24. (a) Evolution of the fraction of ballistic electrons along the channel in DGMOS of gate length 20 nm and $T_{Si} = 20$ nm at $V_{gs} = 0.5$ V, $V_{ds} = 0.5$ V and 1.0 V. (b). Evolution of intrinsic ballisticity as a function of the potential V_{ds} with the same gate voltage $V_{gs} = 0.5$ V in two simulation cases : isothermal or open loop (dashed line) and electro-thermal or self-consistent simulation (continuous line).

The B_{int} reduction is present at all positions along the channel. The higher the drain bias, the stronger is the reduction of the ballisticity. At the drain-end of the channel, the difference of ballisticity between the isothermal and electro-thermal cases is about 2.8 % for $V_{ds} = 0.5$ V and 7.4% for $V_{ds} = 1.0$ V.

Until now, we have quantitatively analyzed the scattering events that slow down electrons and increase the electrical resistance. Consistently, taking into account the thermal effects tends to reduce the average velocity and kinetic energy of electrons. The results are shown in Figs. 3.25 and 3.26 as a function of the number of loops. It illustrates once again the rapid convergence: after the 1st loop, the velocity and the kinetic energy of electrons are very close to that obtained after the 4th loop.

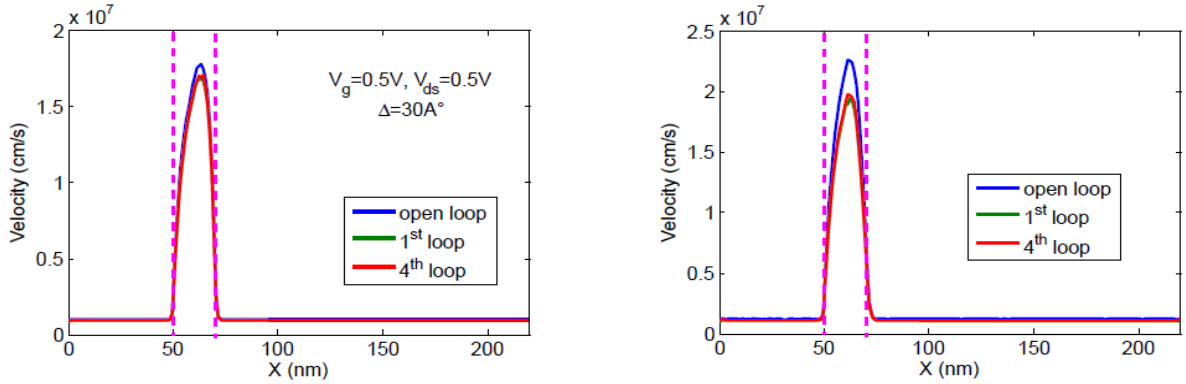

Fig. 3.25. Evolution of average velocity of electron along the channel for V_{gs} = 0.5 V, and for different drain biases V_{ds} = 0.5 V and1.0 V in the isothermal case and in two self-consistent cases.

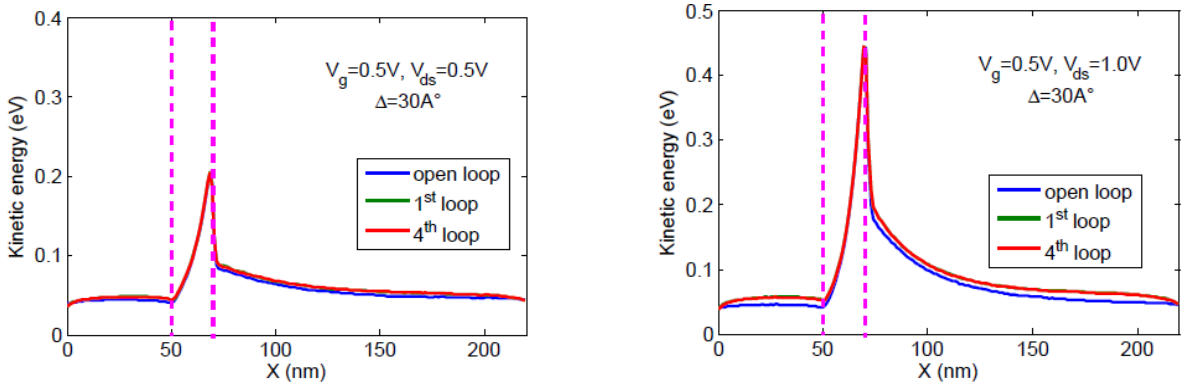

Fig. 3.26. Evolution of kinetic energy of electron along the channel for V_{gs} = 0.5 V, and for different drain biases V_{ds} = 0.5 V and 1.0 V in the isothermal case and in two self-consistent cases.

The velocity is slightly reduced when self-heating is included in particular in the middle of the channel, where the maximum velocity is reached. After the drain-end of the channel the overshoot velocity is rapidly relaxed in the drain extension. The situation is different regarding the average kinetic energy. It should be noted that a much greater length is needed to relax the kinetic energy in the drain extension than to relax the velocity. The self-heating effects influence mainly the energy in the two accesses that is increased due to higher temperatures. This is, of course, more visible when the drain bias is higher.

We plot in Fig. 3.27.a the evolution of the drain current for three bias points as a function of the number of loops. We can see again that the convergence can be reached after only 1 or 2 iterations whatever the drain bias value. The evolution of the I_d-V_{ds} characteristics at V_{gs} = 0.5 V is shown in Fig. 3.27b. Relative degradations of 6.9% and 8.1% of the drain current are observed for V_{ds} = 0.5 V and 1.0 V, respectively, for a roughness of 30 Å. The increase of this degradation as a function of the drain bias is shown in Fig. 3.28.

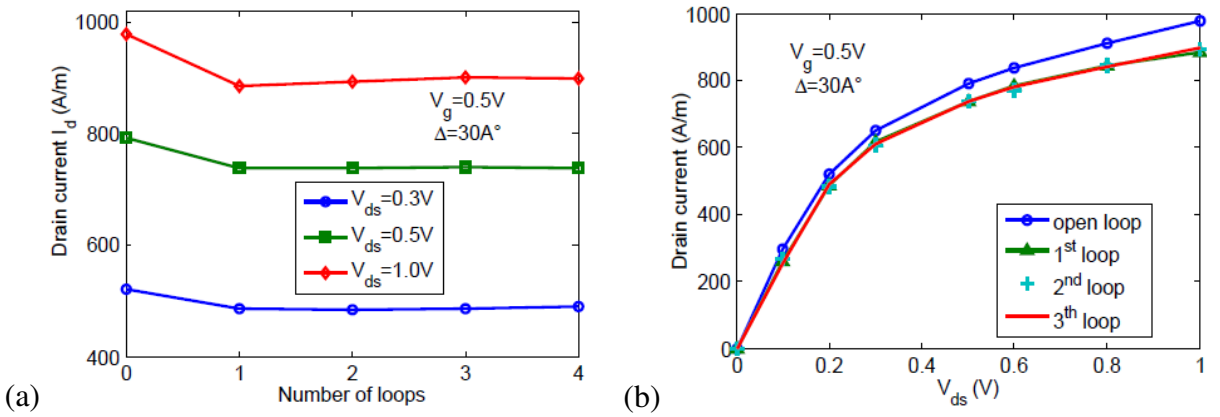

Fig. 3.27. (a) Current convergence as a function of the loop number for three drain bias V_{ds} = 0.3 V, 0.5 V and 1.0 V. (b) I-V_{ds} curves for V_{gs} = 0.5 V after open loop, the 1st loop, the 2nd loop and the last loop (4th loop) for the roughness of 30 Å.

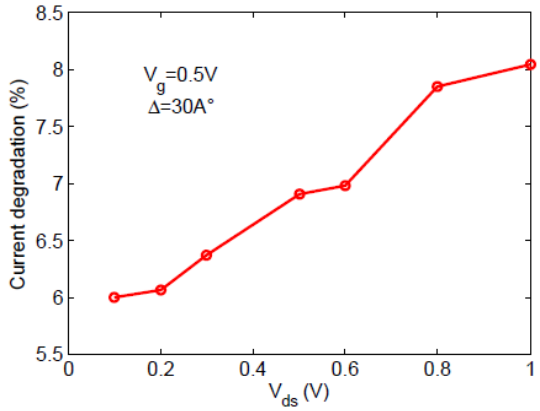

Fig. 3.28. Self-heating-induced drain current degradation as a function of the drain bias for V_{gs} = 0.5 V.

We have seen in sub-section 2.2 of the present chapter that, for given conditions of electronic transport, the more the Si-SiO_2 interface is rough, the more the temperature is raised in the transistor. Here, we analyze the effect of interface roughness on the final temperature, the intrinsic ballisticity and the drain current. The effective temperatures of the 1st loop and of the last loop with different roughness parameters (Δ = 3.5 Å, 10 Å and 30 Å) for V_{ds} = 1.0 V and V_{gs} = 0.5 V are plotted in Fig. 3.29. Note that the change of roughness parameters is considered here only for the phonon boundary scattering.

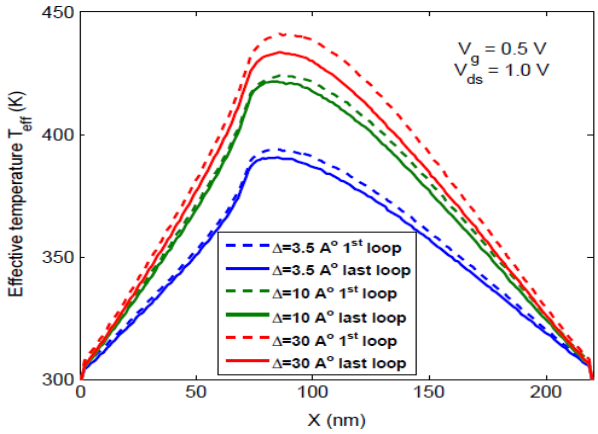

Fig. 3.29. Roughness dependence of effective temperature in DGMOS for V_{gs} = 0.5 V, V_{ds} = 1.0 V.

As discussed in the sub-Section 2.2, the more the heat transport is impeded by the rough Si-SiO_2 interface, the more the system is hot. This is observed not only for the temperature of the 1st loop but also for the temperature obtained after the self-consistent simulation.

The effective temperatures reach their maximal value always in the same region. With all roughness parameters, the final effective temperature is reduced (by about 8K-9K) in comparison with the corresponding temperature in the 1st loop. This reduction occurs principally in the drain-end of the channel and in the drain extension. Indeed, by taking into account the thermal effects, electrons are less accelerated and less energetic (see Figs. 3.25 and 3.26) in the drain region than in the isothermal case; consequently, the number of generated by electron scattering events is smaller.

Finally, the degradation of drain current as a function of roughness parameter for two bias conditions is displayed in Fig. 3.30.

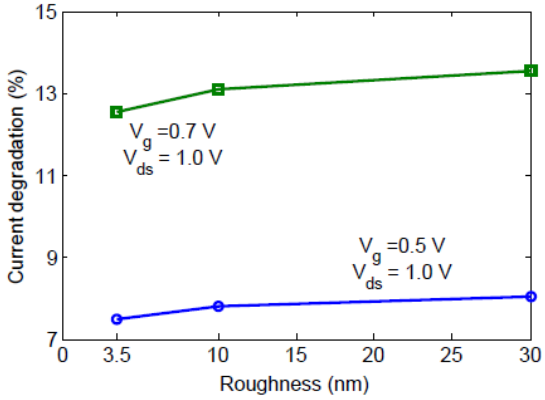

Fig. 3.30. Roughness dependence of current degradation in DGMOS for V_{gs} = 0.5 V, V_{ds} = 1.0 V and for V_{gs} = 0.7 V, V_{ds} = 1.0 V.

Even if the effective temperatures are very different when changing the roughness (see Fig. 3.27), the drain current degradation varies slightly. For $V_{gs} = 0.7$ V, $V_{ds} = 1.0$ V, this degradation is 12.5% with $\Delta = 3.5$ Å and 13.5% with $\Delta = 30$ Å. The variation of this quantity for $V_{gs} = 0.5$ V, $V_{ds} = 1.0$ V is about 8%. Hence, if the influence of roughness is limited to the phonon transport through the change of phonon boundary scattering rate (without changing the scattering rate of electrons) the influence on the current through the change of temperature is very small.

3.3. Conclusions

In this chapter, by using a typical Monte Carlo simulator (MONACO) and considering quadratic phonon dispersion, we take out the phonon generation due to electron scattering in silicon device. The LA and TO generation are the main contributions. This dissipation has been compared with a macroscopic approach (of the Joule effect) derived from the drift-diffusion approach. A discrepancy between these two models is observed at the drain end where the electric field is strong and where the majority of phonons is generated. Furthermore, in our simulator, the energy conservation is ensured, i.e. the electron energy gained during the carrier's acceleration by the electric field is transformed into phononic energy.

Our model includes the decay of optical phonons into the acoustic modes and a generation term from e-MC simulation that is used in the solution of the Boltzmann equation. The profile temperature per mode and the comparison between diffusion temperature and the effective temperature are presented. Our results show the significant role of LTO decay in heat transport, particularly at the hotspot region. One of the main advantages in our model is its capacity to take into account rough interface. The temperature in the device is dependent on the roughness of the Si-SiO_2 interface. In order to reduce the self-heating effect, it is required to fabricate transistors with Si-SiO_2 interface as smooth as possible. The phonon densities for each mode at the hotspot position are shown as an evidence of non-equilibrium phonon transport.

Finally, we have coupled the non-equilibrium transport of electrons and phonons in the 20nm-long DG-MOSFETs by taking into account in the electron scattering rates the effective

temperature obtained from the pBTE. A loop includes an e-MC simulation followed by a pBTE solution. The convergence is reached after only 3 or 4 loops. Electro-thermal effects on the electron and phonon transport in DG-MOSFETs is analyzed: effective temperature, thermal flux, electronic potential, electron velocity and energy… Taking into account electro-thermal effect increases the scattering of electrons along the devices, and therefore decreases the intrinsic ballisticity. Thus, self-heating leads to a current decrease.

GENERAL CONCLUSION

In the context of VLSI (Very Large Scale Integration) circuits and the continuation of downscaling, self-heating effects are identified as one of the most critical issue. In ultra-short transistors, the high power density generated during the working operation is related to the emission of phonons by hot electrons at the microscopic scale. As the transistor dimensions and the Si film thickness are scaled down to the order of ten nanometers, which is much less than the phonon mean free path, non-equilibrium effects will take place. However, it is difficult to study experimentally the heat transport in transistors, in particular during the device operation. Therefore, the simulation of coupled electron and phonon transports to evaluate the electro-thermal effects in nanoscale devices is of great interest for both academia and industry.

In this context, the present work has investigated and estimated theoretically the thermal transport in different regimes and in structures of various geometries. In particular, the heat generation and transport in bulk Si and the local heating in ultra-short Si devices have been studied. Finally, a fully coupled self-consistent electro-thermal simulation has been performed.

In chapter II, a new set of scattering parameters has been introduced to reproduce the thermal conductivity in bulk Si and GaAs materials. A model of optical phonon's decay into acoustic phonons was established. Then, an analytical model has been presented to calculate the thermal conductivity. By using our set of scattering parameters adjusted for a quadratic phonon dispersion and including the phonon-boundary scattering in various device geometries, our results capture well the trend of the thermal conductivity in thin films and in different kinds of wires. In addition, our analytic model is successfully used to fit the experimental thermal conductivities in rectangular cross-section wires by using realistic roughness parameters.

Next, an original numerical method to solve the stationary BTE for phonons under RTA for phonons has been presented. A solution of the Fourier heat equation is coupled to the BTE to estimate the scattering terms properly. Our method gives the good predictions of thermal conductivity for pure Si bulk at 150K and higher temperatures. Then, to predict the thermal

conductivity of Si nano-structures, the phonon-boundary scattering is taken into account. In-plane conductivities match very well with the experimental data. In addition, the cross-plane conductivity, which is until now difficult to measure experimentally, is investigated with our BTE model. The resulting conductivity is in better agreement with the experiment than other theoretical approaches.

For GaAs nano-pillars, with sine type phonon dispersion and an appropriate set of scattering parameters, our BTE solver in the RTA has been used successfully to reproduce the thermal conductance in ultra-short GaAs nano-pillars. The ballistic phonon transport is clearly dominant though the thermal conductivity in nanometer-long pillars is slightly affected by scattering at temperatures higher than 100 K.

Furthermore, our numerical results have been successfully assessed in all heat transfer regimes: diffusive, intermediate and ballistic regimes. Our method is consistent with the Stefan-Boltzmann law at the ballistic limit and with the Fourier law in the diffusive limit. The LA and TA phonon occupations are analyzed from our simulations to make clear the physics in each regime.

In chapter III, by using the analytical model for electron dispersion in MONACO and by employing the quadratic and isotropic phonon dispersion, we showed out the phonon generation by electron scattering during the electronic transport in bulk silicon. It appears that the highest contribution to the phonon generation comes from LA and TO modes (about 40% each), while the TA and LO contributions are smaller. The resulting exact dissipation is compared with the Joule heating estimated using conventional macroscopic calculations in bulk Si and also in a DG-MOSFET of 20 nm gate length under several bias conditions. In the latter case, a strong discrepancy between the two approaches is observed at the drain-end of the channel and in the drain extension where almost all phonons are generated by hot electrons which relax their energy by emitting phonons.

Next, we have investigated the heat transport in this transistor by taking into account the phonon generation obtained from MONACO as an input in the pBTE solver. The profile temperature per mode and the comparison between diffusion temperature and the effective temperature are pointed out. The TA and LA mode temperatures are higher than that of the LO and TO modes which are higher than the diffusion temperature. The contribution to the total heat transport of each mode has been discussed through the analysis of the thermal flux.

Then, we have studied the dependence on the Si-SiO_2 roughness of the temperature profile. As expected, it appears that to reduce the self-heating effect under strong electric field, it is required to fabricate the transistors with a Si-SiO_2 interface as smooth as possible. Finally, the phonon occupation densities for each mode at the hotspot region are shown as an evidence of non-equilibrium phonon transport.

Finally, we have coupled the non-equilibrium transport of electrons and phonons in a 20 nm-channel DG-MOSFET by taking into account the effective temperature obtained from the steady-state pBTE in the update of phonon-electron scattering rates. The convergence is reached after only 3 or 4 loops. The influence of electro-thermal effects on the electron and phonons transport in DG-MOSFETs is analyzed in terms of effective temperature, thermal flux, electronic potential, electron velocity and energy… Because of the raised temperatures throughout the transistor, all types of electron interaction are significantly increased in the coupled electro-thermal simulation with respect to the isothermal simulation. In particular, at channel drain-end, the inter-valley scattering in the coupled simulation is enhanced by 23 % for the bias conditions $V_{gs} = 0.5$ V, $V_{ds} = 1.0$ V. As a consequence, the intrinsic ballisticity, velocity and kinetic energy of electrons obtained from electro-thermal simulation are reduced. Consistently, the drain current is also reduced in comparison with the isothermal simulation. This current degradation is discussed as a function of the bias voltage and of the surface roughness.

Suggestion for the future work

1. Development the RTA for each phonon mode

As seen in chapter III, we coupled the non-equilibrium electron and phonon transport in transistor with the assumption that the lattice temperature is the effective one obtained from pBTE and all electron scattering rates are updated at this temperature. At this point, we can extend the model for each electron-phonon mode scattering: electrons should scatter with a phonon at the temperature T_{mode} of the phonon. Other scattering mechanisms, such as the electron-impurity and alloy scattering could be dependent on the lattice temperature.

2. Extension of the BTE simulation to two dimensions and improved treatment of interfaces

In this work, we solved the pBTE in one dimension to reduce the calculation time for the long-drain transistor. For shorter devices and other device architectures, it would be relevant to implement the 2D-BTE.

Then, the energy transmission at the Si-SiO_2 interfaces could be taken into account to evaluate better the role of SiO_2. In addition, with 2D simulation, we could investigate the phonon temperature with different boundary conditions (Neumann/Dirichlet).

APPENDIX

APPENDIX A: Giant piezoresistance effect in p-Si nanowires [Nghiem11]

The piezoresistance is defined as the change in electrical resistance under the effect of mechanical stress [Smith54]. Indeed, depending on its orientation with respect to the crystallographic direction, strain can induce major changes in the band structure of semiconductors and therefore in the carrier mobility [Leu08, Shiri08, Maegawa09, Huet08-1]. This effect has been reported for the first time in the 50s by the group of Smith [Smith54].

Recently, He and Yang have reported measurements of giant piezoresistance in p-type silicon nanowires, for diameters ranging from 50 to 350 nm. High piezoelectric coefficients (up to about 3500×10^{-11} Pa^{-1}) were obtained for structures of high resistivity (i.e. lightly doped) and small diameter [He06]. It opens the way to the design and implementation of very small piezoresistive sensors, 5 to 10 times smaller than current MEMS components, with performance at least equal or even superior to those of the state of the art. For this purpose, the theoretical understanding of this phenomenon by means of accurate simulation is of practical importance is necessary.

Some studies have attempted to explain the origin of this giant piezoresistivity effect [Cao08, Nakamura09] which, at the microscopic level is not fully understood yet. In the study presented here, we investigate the effect of piezoresistivity in thin silicon layers using the particle Monte Carlo (MC) method to solve the Boltzmann transport equation within a "full-band" description of the band structure [Huet08]. The model proposed by Rowe is used to model the effect of stress on the surface potential [Rowe08].

Model and simulated structures

A nanowire is essentially a three-dimensional object. However, in a first approach to the problem of giant piezoresistance and to reduce the computation time, we restricted ourselves to the consideration of silicon nano-layers of infinite width described in 2D real space. The

effect of stress on the surface potential is applied on both sides of the nano-layer. The effect of stress on the surface potential is applied on both sides of the nano-layer, as illustrated in Fig. A.1 that schematizes the simulated structures. They consist of p-type silicon layers of different thicknesses and resistivities (i.e. doping density).

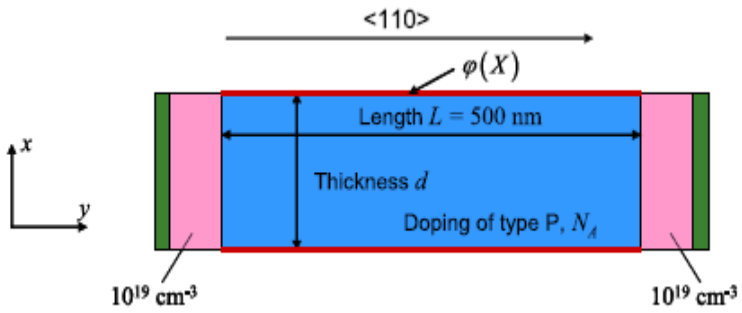

Fig. A.1. Schematic cross-section of simulated structures.

In nanostructures, the size quantization effects may be very important. Several works on silicon nanowires have shown that these effects may substantially influence their electrical and mechanical properties. In particular, for diameter smaller than 20 nm, many physical quantities such as the Young's modulus, the Poisson ratio, the electron and hole effective mass, the band gap and the mobility are strongly affected with respect to bulk data [Leu06, Leu08, Ghetti07]. However, in this study, to compare with available experimental data, we simulated structures with minimum thicknesses of 80 nm that are much larger than the critical size above mentioned. Thus, though our model is able to include them [StMartin06], quantization effects may be neglected here.

All simulated structures had an effective length of 500 nm. The thicknesses were 80 nm, 100 nm, 150 nm or 200 nm. The p-type Si layer was doped to 10^{18} cm^{-3}, 2.7×10^{17} cm^{-3} or 1.49×10^{16} cm^{-3}, which correspond to bulk resistivities of 0.044 Ωcm, 0.1 Ωcm and 1 Ωcm, respectively. At both ends, the Si layer is overdoped to 10^{19} cm^{-3} and contacted by an Ohmic contact which injects/detects the flux of particles flowing through the structure. An uniaxial stress was uniformly applied along the <110> transport direction y. The surface potential φ was defined as the difference in the top of valence band between the surface and the volume of the material where neutrality was assumed to be recovered. The effect of stress was modeled along the line proposed by Rowe who investigated the giant piezoresistance effect in

Si nanowires using a very simple approach of transport [Rowe08]. For a uniaxial stress X, the surface potential is assumed to vary according to the law

$$\frac{d\varphi}{dX} = 0.5meV / MPa \qquad \text{(A-1)}$$

considering that for unstrained Si, φ_0 = 0.54 eV. The nano-layers were simulated under a bias voltage of 0.5 V for stresses ranging from 0 to ± 200 MPa (the sign "+" for a tensile stress, the "–" for a compressive stress).

Simulation results

+ Potential and hole density

According to Eq. A-1, the surface potential is reduced under tensile strain while it is enhanced under compressive strain.

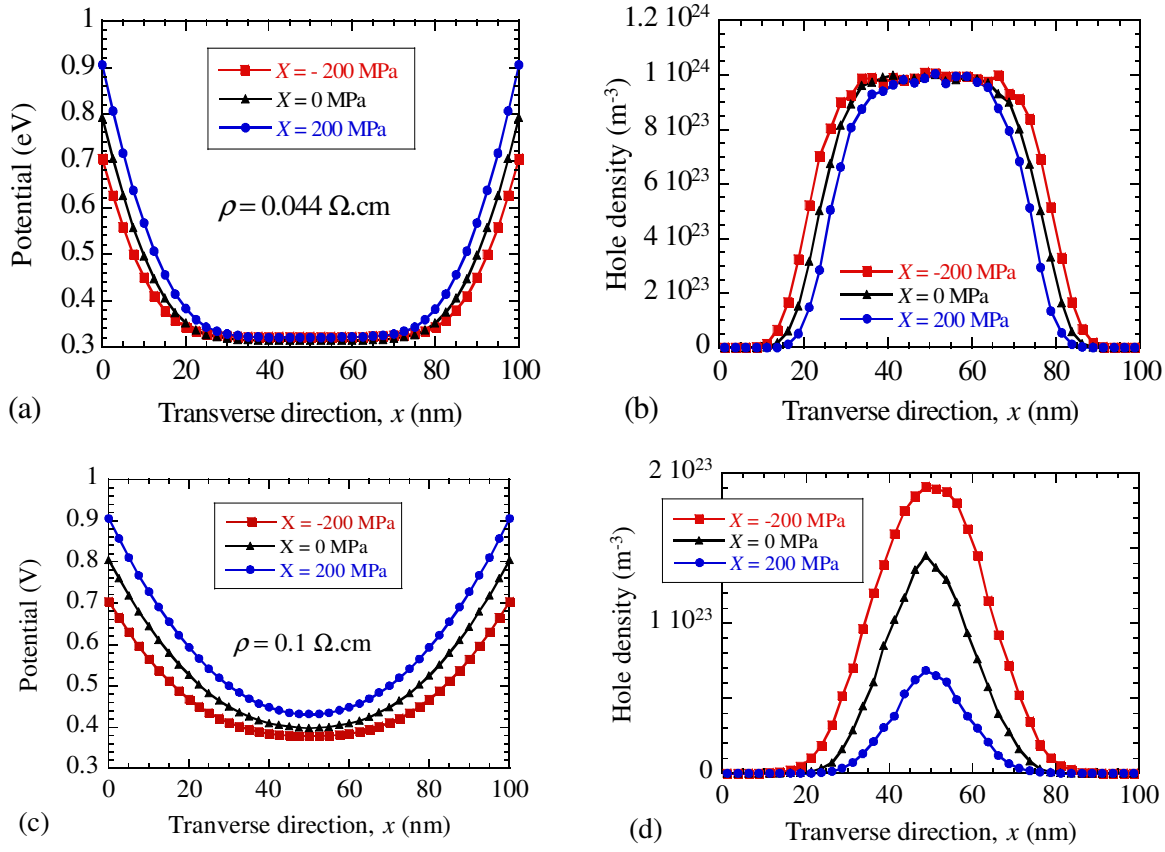

Fig. A.2. (a) Potential and (b) hole density profiles in an 100 nm-thick Si layer of resistivity 0.044 Ω.cm for three stress conditions *X*. (c) Potential and (d) hole density profiles in an 100 nm-thick Si layer of resistivity 0.1 Ω.cm for three stress conditions *X*.

Fig. A.2a shows the typical potential profile in the middle of the device along the transverse direction for three values of stress and a small resistivity ρ = 0.044 Ω.cm. The stress essentially modulates the depth of the surface depleted region, while the potential in the center of the structure remains unchanged and equal to its equilibrium position. Accordingly, the maximum hole density remains equal to the impurity concentration in the central region. The stress controls only the width of this neutral region, i.e. the conductive area, as shown in Fig. A.2b.

The situation is different for a higher resistivity ρ = 0.1 Ω.cm, as shown in Fig. A.2c and Fig. A.2d. Due to its lower doping concentration, the depleted region extends more deeply into the structure and the potential does not fully recover its equilibrium position (Fig. A.2c). Accordingly, there is no longer any neutral region in the device and the stress not only controls the width of the conductive area but also the height of the potential barrier for holes and the maximum hole density (Fig. A.2d). These results are in qualitative agreement with experimental C-V measurements on nanowires [Garnett09].

+ Current

Figure A.3 shows the current as a function of stress in the nano-layers for a thickness of 100 nm and various resistivity values. In the low-resistivity (ρ = 0.044 Ω.cm) structure, the current is controlled by the width of the conductive area and is linearly dependent on stress.

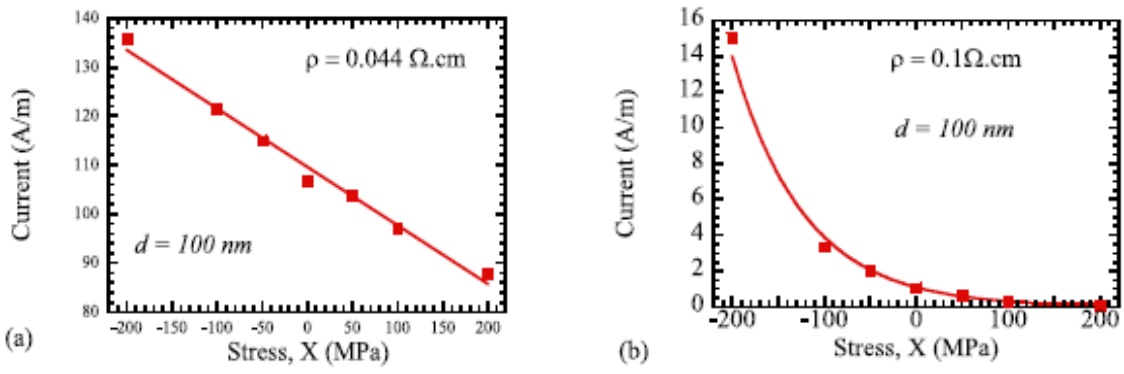

Fig. A.3. Currents versus stress in nano-layers of 100 nm-thickness for (a) resistivity of 0.044 cm; (b) resistivity of 1 cm. The solid lines are exponential fitting curves.

For higher resistivity ($\rho = 0.1$ Ω.cm and 1 Ω.cm), the current is much lower and controlled by the height of the potential barrier in the center of the structure, which leads to a quasi-exponential dependence of the current with the stress.

+ Variation of conductivity

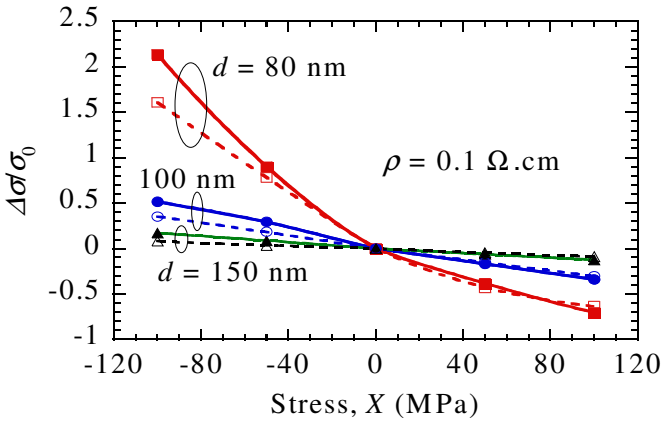

Fig. A.4. Relative variation of conductivity $\Delta\sigma/\sigma_0$ as a function of stress with (solid lines) and without (dashed lines) inclusion of changes in band-structure for a resistivity of 0.1 Ω.cm.

To separate the contributions of stress-induced changes in the valence band structure and in the surface potential, we first considered the effect of surface potential modulation while keeping the band structure of unstrained Si. The results are plotted in Fig. A.4.

The variation of conductivities is presented by the dashed line. The effect of stress on the band structure was considered in a second stage (curves are in solid lines curves). Comparison of solid and dashed lines in Fig. A.4 shows that both contributions of the potential surface variation and of the change in bands must be taken into account, though the latter is smaller, especially in the case of thin layers. The impact of the band's changes is mainly noticed under compressive uniaxial stress. Indeed, in such case the strong reduction of heavy-hole mass [Huet08-2] induces a significant enhancement of mobility [Huet08-1,Huet08-2]. The change in conductivity is not always linear and it strongly depends on both the doping level and the thickness (that is to say, the diameter in the case of a nanowire). For a given resistivity, the variation $\Delta\sigma/\sigma_0$ as a function of stress is higher and more nonlinear when the layer thickness is reduced. The amplitude of the conductivity variation obviously increases when increasing the resistivity (see fig. A.5a).

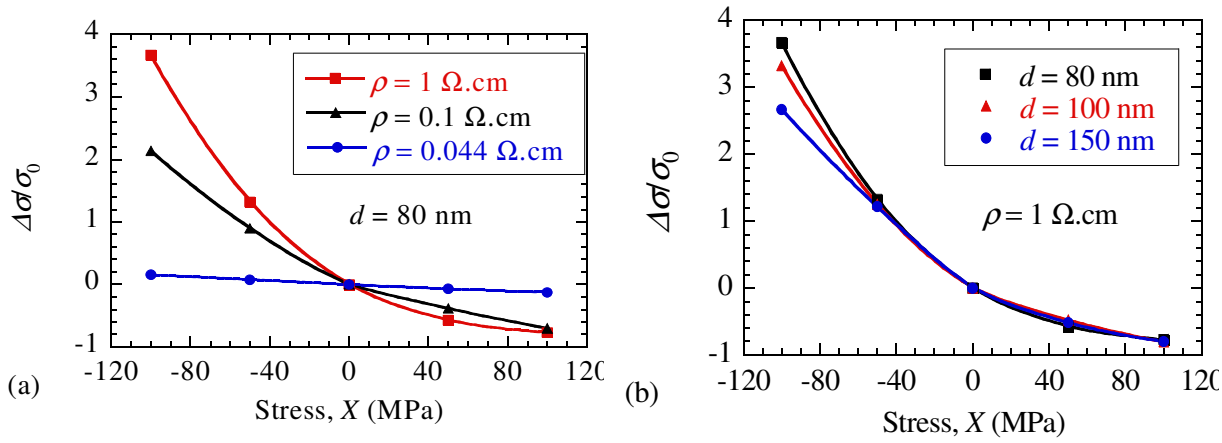

Fig. A.5. (a) $\Delta\sigma/\sigma_0$ as a function of stress including stress-effects on bands for the thickness of 80 nm and for different resistivities. (b) $\Delta\sigma/\sigma_0$ as a function of stress for the resistivity of 1 Ω.cm and for different thicknesses.

For a high resistivity (1 Ω.cm), the relative change in conductivity as a function of stress seems to be nearly independent of the layer thickness, as shown in Fig. A.5b. This is probably associated to the fact that the current in a quasi-fully-depleted region is exponentially controlled by the potential barrier whatever the thickness, which makes the stress-dependent change of relative conductivity weakly dependent on thickness.

Overall, these results are in agreement with trends observed experimentally by He and Yang's for nanowires [He08].

+ Piezoresistive coefficient

The corresponding piezoresistive coefficients were calculated around $X = 0$ using the following expression

$$\pi_l^{\sigma} = \frac{1}{\sigma_0}\frac{d\sigma}{dX} \qquad \text{(A-2)}$$

where σ_0 is the conductivity under zero stress. The resulting piezoresistive coefficients are summarized in Table A.1. As expected, they are strongly dependent on the nano-layer thickness and resistivity. A large piezoresistive coefficient of 1750×10^{-11} Pa^{-1} is obtained for a 80 nm thick layer with resistivity of 1 Ω.cm.

Thickness d (nm)	Piezoresistive coefficient (x $10^{-11}Pa^{-1}$)		
	ρ= 0.044 $\Omega.cm$	ρ =0.1 $\Omega.cm$	ρ = 1 $\Omega.cm$
80	141	842	1750
100	111	420	1589
150	80	149	1564
200	60	105	1505

Table A.1. Piezoresistive coefficient in p-type <110> oriented Si nano-layers for different thicknesses and resistivities (values given in 10^{-11} Pa^{-1}).

The results obtained are quite consistent with experimental results of He and Yang. For instance, they obtained a first order piezoresistive coefficient of 660×10^{-11} Pa^{-1} for a 75 nm thick <110> oriented nanowire with a resistivity of 0.3 Ω.cm [He06]. Reck et al. obtained 455×10^{-11} Pa^{-1} for a 140×200 nm^2 wire of resistivity 0.4 Ω.cm [Reck08]. The highest piezoresistive coefficient measured was 3100×10^{-11} Pa^{-1} for a nanowire with resistivity of 10^2 Ω.cm. Accurate MC calculation in such a high resistivity layer is very difficult because of very small current level.

Conclusion on the simulation of giant piezoresisitif effect

Using 2D MC simulation, we have been able to reproduce the giant piezoresistance in silicon nano-layers with thickness of 80–200 nm which are assumed to behave as nanowires. Taking into account the effects of stress on both the surface potential and the valence bands make it possible to modulate the depletion depth and the conductivity of the structure. The effective conduction area, wide in the case of compression, becomes much narrower in the case of tensile strain. The relative variation of conductivity and the piezoresistive coefficient show a strong dependence on both the thickness and the resistivity. Our results are in satisfying agreement with experimental data available for nanowires.

APPENDIX B: Solution of diffusive equation

The diffusive equation is written as

$$\partial T / \partial t = \nabla \cdot \left(K_T \nabla T \right) + P, \tag{B-1}$$

Where K_T is the thermal conductivity that depends on temperature T and P is the power in system. In the steady-state, without power P, the above equation is reduced in form like

$$\nabla \left(k_T \nabla T \right) = 0. \tag{B-2}$$

The temperature dependence of silicon thermal conductivity K_T can be described by

$$k_T = C \cdot T^{\alpha}. \tag{B-3}$$

Where C and α are constant.

By replacing (B-3) in (B-2), we have

$$\nabla \left(C \cdot T^{\alpha} \nabla T \right) = 0. \tag{B-4}$$

Then, the use of $T^{\alpha} \nabla T = \frac{\nabla T^{\alpha+1}}{\alpha+1}$ gives

$$\frac{C}{\alpha+1} \cdot \Delta T^{\alpha+1} = 0. \tag{B-5}$$

By setting $U = T^{\alpha+1}$, the equation (B-5) has the form similar to the Fourier's equation form

$$\frac{C}{\alpha+1} \Delta U = 0. \tag{B-6}$$

Numerical solution of (B-6) can be easily obtained, then the temperature T is $U^{1/(\alpha+1)}$.

Analytic solution

The equation (B-5) for one direction is

$$\frac{\partial^2 T^{\alpha+1}}{\partial z^2} = 0. \tag{B-7}$$

By integrating the above equation, we have

$$T^{\alpha+1}(z) = F(z), \tag{B-8}$$

Where $F(z)$ is a linear function of z.

For a bar with temperatures at the two extremities are T_h and T_c, the limit conditions are

$$T^{\alpha+1}(0)=T_h^{\alpha+1}=F(0), \tag{B-9a}$$

$$T^{\alpha+1}(L)=T_c^{\alpha+1}=F(L). \tag{B-9b}$$

The analytic solution is easily obtained as

$$T=\left(\frac{z}{L}\cdot T_c^{\alpha+1}+\left(1-\frac{z}{L}\right)\cdot T_h^{\alpha+1}\right)^{1/(\alpha+1)}. \tag{B-10}$$

PUBLICATION

International peer review journals

T.T. Trang Nghiêm, V. Aubry-Fortuna, C. Chassat, A. Bossebeuf and P. Dollfus *"Monte Carlo simulation of giant piezoresistance effect in p-type silicon nanostructures"*, Modern Physics Letters B, vol. **25**, Issue 12-13, pp. 995-1001, 2011.

International conference with proceedings

T.T. Trang Nghiêm, V. Aubry-Fortuna, C. Chassat, A. Bossebeuf and P. Dollfus, *"Giant piezoresistance effect in p-type silicon*", International conference on Simulation of Semiconductor Processes and Devices (SISPAD), Bologne, Italie, 6-8 September 2010, pp. 321-324 (2010).

International conference without proceedings

T.T. Trang Nghiêm, J. Saint-Martin, P. Dollfus, *"Self-heating in ultra-small DG-MOSFET"*, EuroSOI 2013, Paris, France, 21-23 Janvier 2013 (accepted).

T.T. Trang Nghiêm, J. Saint-Martin, P. Dollfus, *"Non-equilibrium thermal transport modelling at nanometer-scale in silicon"*, Phonons and fluctuations meeting, Paris 8-9 September 2011.

T.T. Trang Nghiêm, J. Saint-Martin, P. Dollfus, *"Thermal dissipation and transport at nanometer-scale in silicon"*, Poitier, France, 29-31 August 2011, Eurotherm 91, Microscale heat transfer III**.**

T.T. Trang Nghiêm, V. Aubry-Fortuna, C. Chassat, A. Bossebeuf and P. Dollfus, *"Monte Carlo simulation of giant piezoresistance effect in p-type silicon nanostructures*", The international conference on frustrated spin systems, cold atoms, nanomaterials (STATPHYS), Hanoi, Vietnam, 11-13 Julliet 2010.

National conference with and without proceedings

T.T. Trang Nghiêm, J. Saint-Martin, P. Dollfus, *"Modélisation du transport thermique hors-équilibre dans des dispositifs nanoélectroniques en silicium",* Orsay, France, GDR Thermoélectricité, 11-12 July 2011.

T.T. Trang Nghiêm, J. Saint-Martin, P. Dollfus, *"Etude du transport de phonons et de la dissipation thermique dans du silicium à l'échelle nanométrique"*, Journées nationales du réseau doctoral en Micro-nanoélectronique (JNRDM), Cachan, France, 23-25 May 2011.

T.T. Trang Nghiêm, J. Saint-Martin, P. Dollfus, *" Etude de l'effet de piézo-résistivité géante dans les nano-fils de silicium"*, Journées nationales du réseau doctoral en Micro-nanoélectronique (JNRDM), Montpellier, France, 07-09 June 2010.

Book chapter

Valérie Aubry-Fortuna, Karim Huet, T.T. Trang Nghiêm, Arnaud Bournel, Jérôme Saint-Martin and Philippe Dollfus (2011). *Strain Effects in p-type Devices using Full-Band Monte Carlo Simulations*, Applications of Monte Carlo Methods in Biology, Medicine and Other Fields of Science, Charles J. Mode (Ed.), ISBN: 978-953-307-427-6, InTech, Available from: http://www.intechopen.com/articles/show/title/strain-effects-in-p-type-devices-using-full-band-monte-carlo-simulations

BIBLIOGRAPHY

[Aksamija10-1] Z. Akasamija & I. Knezevic, *Anisotropy and boundary scattering in the lattice thermal conductivity of Si nanomembranes*, Phys. Rev. B **82**, pp. 045319 (2010).

[Allain12] P. Allain, *Etudes des proprieties électro-thermo-mécaniques de nanofils en silicium pour leur integration dans les microsystems*, Ph. D. Thesis, Université Paris Sud (2012).

[Anantram08] M. P. Anantram et al., *Modeling of nanoscale devices*, Proceed. IEEE, **96**, pp. 1511 (2008).

[Asche81] M. Asche & O. G. Sarbei, *Electron-phonon interactions in n-Si*, Phys. Stat. Sol. **108**, 11 (1981).

[Asheghi02] M. Asheghi *et al.*, *Thermal conduction in doped single-crystal silicon films*, J. Appl. Phys. **91**, 5079 (2002).

[Asheghi97]: M. Asheghi, *Phonon-boundary scattering in thin silicon layers*, Appl. Phys. Lett. **71**, 13 (1997).

[Askamija10] Z. Aksamija & U. Ravaioli, *Anharmonic decay of g-process longitudinal optical phonons in silicon*, Appl. Phys. Lett. **96**, 091911 (2010).

[Aubry-Fortuna05] V. Aubry-Fortuna *et al.*, *Electron effective mobility on strained-Si/$Si_{1-x}Ge_x$ device using Monte Carlo simulation*, Solid-State Electronics **49**, 1320 (2005).

[Aubry-Fortuna11] V. Aubry-Fortuna *et al.*, *Strain Effects in p-type Devices using Full-Band Monte Carlo Simulations*, Applications of Monte Carlo Methods in Biology, Medicine and Other Fields of Science, Charles J. Mode (Ed.), ISBN: 978-953-307-427-6, InTech, Available from: http://www.intechopen.com/articles/show/title/strain-effects-in-p-type-devices-using-full-band-monte-carlo-simulations

[Baillis09] D. Baillis & J. Randrianalisoa, *Prediction of thermal conductivity of nanostrucutres : Influence of phonon dispersion approximation*, Int. J. Heat & Mass transfer, Vol. **52**, pp. 2516 (2009).

[Balandin98] A. Balandin and K. L. Wang, *Significant in a free-standing semiconductor quantum well* , Phys. Rev. B **58**, 1544 (1998).

[Balkan98] N. Balkan, *Hot electrons in semicondutors: Physics and Devices*, Clarendon Press Oxford (1998).

[Baro05] M. Baro et al., *A 1D coupled Schödinger drift-diffusion model including collisions*, J. Compt. Phys., **203**, pp. 129 (2005).

[BartschPRL2012] Th. Bartsch *et al.*, *Thermal conductance of ballistic point contacts*, Phys. Rev. Let. **108**, 075901 (2012).

[Berman1953] R. Berman et al., *The thermal conductivity of diamond at low temperatures*, Proc. R. Soc. London, Ser. A **220**, 171 (1953).

[Bir&Pikus74] G. L. Bir & G. E. Pikus, *Symmetry and Strain-induced Effects in Semiconductors*, Wiley, New York (1974).

[Blackemore82] J. S. Blakemore, *Semiconducting and other major properties of gallium arsenide*, J. Appl. Phys. **53**, R123 (1982).

[Brisset94] C. Brisset, *Etude theoriques par simulation Monte Carlo 3D de la sensibilité aux irradiations des technologies CMOS/SOI*, Ph. D. Thesis, Université Paris Sud (1994).

[BroidoPRB2005] A. A. Broido et al., *Lattice thermal conductivity of silicon from empirical interatomic potentials*, Phys. Rev. B **72**, 014308 (2005).

[Cadona66] M. Cardona & F. H. Pollak, *Energy-band structure of germanium and silicon: the k.p method*, Phys. Rev., **142**, pp. 530-543 (1966).

[Callaway59] J. Callaway, *Model for lattice thermal conductivity at low temperatures*, Phys. Rev. **113**, 1046 (1959).

[Canali75] C. Canali *et al.*, *Electron drift velocity in silicon*, Phys. Rev. B **12**, pp. 2265 (1975).

[Cao08] J. X. Cao *et al.*, *Giant piezoresistance and its origin in Si (111) nanowires: First-principles calculations*, Phys. Rev. B, **75**, pp. 233302 (2008).

[Chen98] G. Chen, *Thermal conductivity and ballistic phonon transport in the cross-plane direction of superlattices*, Phys. Rev. B **57**, 14958 (1998).

[ChenPRL08] R. Chen et al., *Thermal conductance of thin silicon nanowires*, Phys. Rev. Lett. **101**, 10501 (2008).

[Conwell67] E. M. Conwell, *High field transport in semiconductors*, Academic Press, New York (1967).

[Debernardi95] A. Debernardi *et al.*, *Anharmonic phonon lifetimes in semiconductors from Density-Funtional Perturbation theory*, Phys. Rev. Lett. **75**, 1819 (1995).

[Degond02] P. Degond & A. El Aayyadi, *A coupled Schödinger dirft-diffusion model for quantum semiconductor device simulations,* J. Compt. Phys. **181**, pp. 222 (2002).

[Degond05] P. Degond et al., *Quantum energy-transport and drist-diffusion models*, J. Stat. Phys., **118**, pp. 625 (2005).

[DudaJAP2010] J. C. Duda et al., *Role of dispersion on phononic thermal boundary conductance*, J. Appl. Phys. **108**, 073515 (2010).

[Ferry76] D. K. Ferry, *First order optical and intervalley scattering in semiconductor*, Phys. Rev. B **14**, pp. 1605 (1976).

[Flik90] M. I. Flik and C. L. Tien, *Size-effect on the thermal conductivity of high T_C thin-film superconductors*, J. Heat Trans. **112**, 872 (1990).

[Fortier76] D. Fortier & K. Suzuki, *Effect of P donors on thermal phonon scattering in Si*, J. de Phys. **37**, 143 (1976).

[Galdin92] S. Galdin, *Etude du transport bipolaire à double hétérojonction Si/SiGe/Si par simulation Monte Carlo*, Ph. D. Thesis, Université Paris Sud (1992).

[Gardner94] C.L. Gardner, *The quantum hydrodynamic model for semiconductor devices*, J. Appl. Math. **54.2**, pp. 409 (1994)

[Germatt08] E. C. Garnett *et al.*, *Dopant profiling and surface analysis of silicon nanowires using capacitance--voltage measurements*, Nature Nanotech., **4**, pp. 311 (2008).

[Ghai05] S. S. Ghai *et al.*, *A novel heat transfer model and its application to information storage systemes*, J. Appl. Phys. **97**, 10P703 (2004).

[Ghetti07]A. Ghetti et al., *Coupled Mechanical and 3-D Monte Carlo Simulation of Silicon Nanowire MOSFETs*, IEEE Trans. on Nanotech.*,* **6**, pp. 659 (2007).

[Glassbrenner64] C. J. Glassbrenner and G. Slack, *Thermal conductivity of silicon and germanium from 3°K to the melting point*, Phys. Rev. **134**, 4A, A1058, (1964).

[Goodnick87] S. M. Goodnick et al., *Surface roughness at the Si(100)-Si interface*, Phys. Rev. B **32**, 8171 (1987).

[Granzner06] R. Granzner et al., *Simulation of nanoscale MOSFETs using modified drift-diffusion and hydrodynamic models and comparison with Monte Carlo results*, MicroElec. Eng., **83**, pp. 241 (2006).

[HDRBournel06] A. Bournel, *Composants pour la spintronique, la microélectronique ultime et la nanoélectronique*, Habilitation à diriger les recherches, Université Paris Sud (2006).

[HDRDollfus99] P. Dollfus, *Etudes théoriques de structures pour l'électronique rapide et contribution au développement d'un simulateur particulaire Monte Carlo*, Habilitation à dirige des recherches, Université Paris Sud (1999).

[He06] R. He *et al.*, *Giant piezoresistance effect in silicon nanowires*, Nature Nanotech., **1**, pp 42 (2006).

[Heaslet65] M. Heasler& R. Warming, *Radiative transport and wall temperature slip in an absorbing planar medium*, Int. J. Heat Mass Transfer **8**, 979 (1965).

[Henry08] A.S. Henry & G. Chen, *Spectral phonon transport properties of Silicon based on molecular dynamics simulations and lattice dynamics*, J. Compt. Theor. Nanosci., vol. **5**, No. **2**, 2008.

[Hesto84] P. Hesto, *Simulation Monte Carlo du transport non stationnaire dans les dispositifs submicroniques: importance du phénomène balistique dans GaAs à 77K*, Thèse de doctorat d'état, Université Paris Sud (1984).

[Hochbaum08] A. I. Hochbaum et al., *Enhanced thermoelectric performance of rough silicon nanowires*, Nature letter **451**, 10 (2008).

[Holland63] M. G. Holland, *Analysis of lattice thermal conductivity*, Phys. Rev. **132**, 2461 (1963).

[Holland64] M. G. Holland, *Phonon scattering in semiconductors from thermal conductivity studies*, Phys. Rev. **134**, A471 (1964).

[Hopkins11] P. E. Hopkins et al*., Reduction in the thermal conductivity of single crystalline silicon by phononic crystal patterning*, Nano Let. **11**, 107 (2011).

[Huet08] K. Huet, *Modélisation du transport sous contrainte mécanique dans les transistors sub-65nm pour la microélectronique CMOS*, Ph. D. Thesis, Université Paris Sud (2008).

[Huet08-1] K. Huet *et al.*, *Experimental and Theoretical Analysis of Hole Transport in Uniaxially Strained pMOSFETs*, Proc. ESSDERC, pp. 234 (2008).

[HVNguyen09] V. Hung Nguyen et al., *Controllable spin-dependent transport in armchair graphene nanoribbon structures*, J. Appl. Phys. **106**, pp. 053710 (2009).

[Jeong10] C. Jeong *et al.*, *On Landauer versus Botlzmann and full band versus effective mass evaluation of thermoelectric transport coefficients*, J. Appl. Phys. **107**, 023707 (2010).

[Jeong12] C. Jeong & M. Lundstrom, *Analysis of thermal conductance of ballistic point contacts*, Appl. Phys. Lett. **100**, 233109 (2012).

[Jeong12] C. Jeong, S. Datta and M. Lundstrom, *Thermal conductivity of bulk and thin-film silicon : A Landauer approach*, J. Appl. Phys. **111**, 093708 (2012).

[Jørgensen78] M. H. Jørgensen, *Electron-phonon scattering and high field transport in n-type Si*, Phys. Rev. B **18**, pp. 5657.

[Ju05] Y. S. Ju and K. E. Goodson, *Phonon heat transport in silicon nanostructures*, Appl. Phys. Lett. **87**,153106 (2005).

[Ju99] Y. S. Ju and K. E. Goodson, *Phonon scattering in silicon films with thickness of order 100nm*, Appl. Phys. Lett. **74**, 20 (1999).

[Jungeman03] C. Jungeman & B. Meinerzhagen, *Hierarchical device simulation: the Monte Carlo perspective*, Springer Wien NenYork (2003).

[Kamakura10] Y. Kamakura *et al.*, *Coupled Monte Carlo Simulation of Transient Electron-Phonon Transport in Nanoscale Devices*, Proc. of SISPAD, 6-8 September Bologna, Italy (2010).

[Kittel71] C. Kittel, *Introduction to solid state physics*, Wiley&Sons, New York, 4th edition, 1971.

[Klemens51] P. G. Klemens, *The thermal conductivity of dielectric solids at low temperatures (Theoretical)*, Proc. R. Soc. Lond. A 7 August 1951, **208**, pp. 108 (1951).

[Klemens55], P. G. Klemens, *The scattering of low-frequency lattice waves by static imperfections* , Proc. Phys. Soc., London **68**, 1113 (1955).

[Klemens66] P. G. Klemens, *Anharmonic decay of optical phonons*, Phys. Rev. **148**, 845 (1966).

[Kumar05] M.J. Kumar & G. V. Reddy, *Diminished Short Channel Effects in Nanoscale Double-Gate Silicon-on-Insulator Metal–Oxide–Semiconductor Field-Effect-Transistors due to Induced Back-Gate Step Potential*, Jpn. J. Appl. Phys., Vol. **4**, No. 9A, pp. 6508 (2005).

[Lacroix09] D. Lacroix et al*., Phonon transport in silicon, influence of the dispersion properties choice on the description of the anharmonic resistive mechanisms*, Eur. Phys. J. B **67**, 15-25 (2009).

[Lacroix05] D. Lacroix et al., *Monte Carlo transient phonon transport in silicon and germanium at nanoscale*, Phys. Rev. B **72**, 064305 (2005).

[Lacroix06] D. Lacroix et al., *Monte Carlo simulation of phonon confinement in nanostructures: Application to the determination of the thermal conductivity of Silicon nanowires*, Appl. Phys. Let. **89**, 103104 (2006).

[Lang99] G. Lang et al., *Anharmonic line shift and linewidth of the Raman mode in covalent semiconductors*, Phys. Rev. B **9**, 6182 (1999).

[Lax72] M. Lax & J.L. Birman, *Intervalley scattering selection rules for Si ang Ge*, Phys. Stat. Solidi, **49**, K153-K154 (1972).

[Leu06] P.W. Leu *et al.*, *Surface chemical control of the electronic structure of silicon nanowires: Density functional calculations*, Phys. Rev. B, **73**, pp. 195320 (2006).

[Leu08] P.W. Leu *et al.*, *Ab initio calculations of the mechanical and electronic properties of strained Si nanowires*, Phys. Rev. B, **77**, pp. 235305 (2008).

[Li03] D. Li et al., *Thermal conductivity of Si/SiGe superlattice nanowires*, Appl. Phys. Lett **83**, 15 (2003).

[Liu04] : W. Liu and M. Asheghi, *Phonon-boundary scattering in ultrathin single-crystal silicon layers*, Appl. Phys. Lett. **8**, 19 (2004).

[Liu05] W. Liu and M. Asheghi, *Thermal conduction in ultrathin pure and doped single-crystal silicon layers*, J. Appl. Phys. **98**, 123523 (2005).

[Long60] D. Long, *Scattering of conduction electron by lattice vibrations in Silicon*, Phys. Rev. **120**, 2024 (1960).

[Lungstrom00] M. Lungstrom, *Fundamentals of carrier transport*, 2nd edition, Cambrige Universiy Press, 2000.

[Luttinger55] J.M. Luttinger & W. Kohn, *Motion of electrons and holes in perturbed periodic fields*, Phys. Rev., **97**, pp. 869 (1955).

[Maegawa09] T. Maegawa *et al.*, *Strain effects on electronic bandstructures in nanoscaled silicon: From bulk to nanowire*, IEEE Trans. Elec. Dev., **56**, pp. 553 (2009).

[MajumdarJHT93] A. Majumdar, *Microscale heat conduction in dielectric thin films*, J. Heat Trans. **115**, 7, (1993).

[Martin09] P. Martin et al., *Impact of phonon-surface roughness scattering on thermal conductivity of thin silicon nanowires*, Phys. Rev. Lett. **102**, 125503 (2009).

[Mazumder01] S. Mazumder & A. Majumdar, *Monte Carlo study of phonon transport in solid thin films including dispersion and polaeization*, J. Heat Transfer **123**, 479 (2001).

[Mazzamuto11] F. Mazzamuto et al., *Enhanced thermoelectric properties in graphene nanoribbons by resonant tunneling of electrons*, Phys. Rev. B, **83**, pp. 235426 (2011).

[Mazzamuto12] F. Mazzamuto et al., *Thermoelectric perormance of disordered and nanostructures graphene ribbons using Green's function method*, J. Comput. Electron. **11**, pp. 67 (2012).

[McGaughey11] A. McGaughey, *Size-dependent model for thin film and nanowire thermal conductivity*, APpl. Phys. Lett. **99**, 131904(2011).

[Menéndez84] J. Menéndez & M. Cardona, *Temperature dependence of the fisrt-order Raman scattering by phonons in Si, Ge, and α-Sn: Anharmonic effects*, Phys. Rev. B **29**, 2051 (1984).

[Milne10] J.S. Milne *et al.*, *Giant piezoresistance effetcs in Silicon nanowires and microwires*, Phys. Rev. Let. **105**, pp. 226802 (2010).

[Mingo03] N. Mingo & Y. Liu, *Phonon transport in nanowires coated with amorphous material: An atomistic Green's function approach*, Phys. Rev. B **68**, pp. 245406 (2003).

[Mittal10] A. Mittal & S. Mazumder, *Monte Carlo study of phonon heat conduction in Si thin films including contributions of optical phonons*, J. Heat Transfer **132**, 052402 (2010).

[Mizuno93] H. Mizuno *et al.*, *Electron-transport simulation in silicon including anisotropic phonon scattering rate*, Phys. Rev. B **48**, 1512 (1993).

[Murthy05] J.Y. Murthy *et al.*, *Review of multi-scale simulation in sub-micron heat transfer*, Int. J. Multiscale Comp. Eng. **3**, 5 (2005).

[Nakamura09] K. Nakamura *et al.*, *First-Principles Simulation on Orientation Dependence of Piezoresistance Properties in Silicon Nanowires*, Jpn J. Appl. Phys., **48**, 06FG09 (2009).

[Narumanchi04] S. V. J. Narumanchi et al., *Submicron heat transport model in Silicon accouting for phonon dispersion and polarization*, J. Heat Transfer **126**, 946 (2004).

[Narumanchi05] S. V. J. Narumanchi et al., *Comparison of different phonon transport models for predicting heat conduction in silicon-on-insulator transistors*, J. Heat Transfer **127**, pp. 713 (2005).

[Narumanchi05] S. V. J. Narumanchi et al., *Computations of sub-micron heat transport in silicon accounting for phonon dispersion*, Paper no. HT2003-47490, pp. 569 (2003).

[Ni09] C. Ni, *Phonon transport models for heat conduction in sub-micron geometries with application to microelectronics*, Ph. D. Thesis, Purdue University (2009).

[Ni12] C. Ni *et al.*, *Coupled electro-thermal simulation of MOSFETs*, J. Compt. Electron **11**, pp. 93 (2012).

[Nilsson72] G. Nilsson & G. Nelin, *Study of the homology between silicon and germanium by thermal-neutron spectroscopy*, Phys. Rev. B **6**, 3777 (1972).

[Odanaka04] S. Odanaka, *Multidimensional discretization of the stationary quantum drift-diffusion model for ultrasmall MOSFET structure*, IEEE Trans. Comp.-Aided Design of Integareted circuits and systems, Vol. **23**, pp. 837 (2004).

[Park11] Y-H. Park et al., *Thermal conductivity of VLS-grown rough Si nanowires with various surface roughnesses and diameters*, Appl. Phys. A **104**, 7 (2011).

[Pop04] E. Pop et al., *Analytic band Monte Carlo model for electron transport in silicon including acoustic and optical phonon dispersion*, Jour. Appl. Phys. **96**, 4998 (2004).

[Pop05] E. Pop *et al.*, *Monte Carlo simulation of Joule heating in bulk and srained silicon*, Appl. Phys. Lett. **86**, pp. 082101 (2005).

[Pop06] E. Pop *et al.*, *Heat generation and transport in nanometer-scale transistor*, Proc. IEEE **94**, 1587 (2006).

[Querlioz08] D. Querlioz, *Phénomène quantiques et décohérence dans les nano-dispositifs semiconducteurs : étude par une approche Wigner Monte Carlo*, Ph. D. Thesis, Université Paris Sud (2008)

[Querlioz10] D. Querlioz & P. Dollfus, *The Wigner Monte Carlo method for nanoelectronic devices – A particle description of quantum transport and decoherence*, Series Edition Wiley (2010).

[Ramayya12] E. B. Ramayya *et al.*, *Thermoelectric properties of ultrathin silicon nanowires*, Phys. Rev. B **86**, pp. 115328 (2012).

[Reck08] K. Reck et al.,*IEEE 21st International Conference on Micro Electro Mechanical Systems, MEMS 2008*, pp. 717-720 (2008).

[Richard 04] S. Richard *et al.*, *Energy-band structure of Ge, Si and GaAs*, Phys. Rev. B, **70**, pp. 235204 (2004).

[Rideau06] D. Rideau *et al.*, *Strained Si, Ge and $Si_{1-x}Ge_x$ alloys modeled with a fisrt-princibles-optimized full-zone k.p method*, Phys. Rev. B, **74**, pp.195208 (2006).

[Romano01] V. Romano, *Non-parabolic band hydrodynamical model of silicon semiconducors and simulation of electron devices*, Math. Meth. Appl. Sci., **24**, 439 (2001).

[Rowe08] A. C. H. Rowe, *Silicon nanowire feel the pinch*, Nature Nanotech., **3**, pp. 311 (2008).

[Rowlette08] J. Rowlette & K. E. Goodson, *Fully coupled nonequilibrium electron-phonon transport in nanometer-scale silicon FETs*, Trans. Elec. Dev. **55**, 220 (2008).

[Sadi10] T. Sadi & R. W. Kelsall, *Monte Carlo study of the electrothermal phenomenon in silicon-on-insulator and silicon-germanium-on insulator metal-oxide field-effect transistors*, J. Appl. Phys. **107**, pp. 064506 (2010).

[Sadi12] T. Sadi *et al.*, *Monte Carlo study of self-heating in nanoscale devices*, J. Comput. Electron. **11**, pp. 118 (2012).

[SaintMartin04-1] J. Saint Martin et al., *Influence of ballistic effects in ultra-small MOSFETs, J. Compt. Elec.*, Vol. **3**, pp. 207 (2004)

[SaintMartin04-2] J. Saint Martin et al., *On the ballistic transport in nanometer-scaled DG MOSFETs*, IEEE Trans. Elec. Dev., Vol. 51, No. **7**, pp. 1148 (2004).

[SaintMartin05] J. Saint-Martin, *Etude par simulation Monte Carlo d'achitectures de MOSFET ultracourts à grille multiple sur SOI*, Ph. D. Thesis, Université Paris Sud (2005).

[SaintMartin06] J. Saint-Martin *et al.*, *Multi sub-band Monte Carlo simulation of an ultra-thin double gate MOSFET with 2D electron gas*, Sicond. Sci. Technol. **21**, L29-L31 (2006).

[Sellan10] D. P. Sellan et al., *Cross-plane phonon transport in thin films*, J. Appl. Phys. **108**, 113524 (2010).

[Shi11] M. Shi, *Simulaton Monte Carlo de MOSFET à base de matériaux III-V pour une électronique haute fréquence ultra basse consommation*, Ph. D. Thesis, Université Paris Sud (2011).

[Shiri08] D. Shiri *et al.*, *Strain induced change of bandgap and effective mass in silicon nanowires*, App. Phys. Lett,. **93**, pp. 073114 (2008).

[Sinha06] S. Sinha *et al.*, *Non-equilibrium phonon distribution in Sub-100 nm silicon transistors*, J. Heat Tranfer **128**, 638 (2006).

[Slisher99] Slisher, Dustin K., et al., *Scaling of Si MOSFETs for Digital Applications*, *Rensselaer Polytechnic Institute* (1999).

[Smith54] C. S. Smith, *Piezoresistance effect in germanium and silicon*, Phys. Rev., **94**, pp 42 (1954).

[Soffer67] S. B. Soffer, *Statistical model for the size effect in electrical conduction*, J. Appl. Phys. **38**, 1710 (1967).

[Strauch90] D. Strauch & B. Dorner, *Phonon dispersion in GaAs*, J. Phys.: Condens. Matter **2**, 1457 (1990).

[Streiwolf70] H. W. Streitwolf, *Intervally scatteing selection rules for Si and Ge*, Phys. Stat. Solidi. K47-K49 (1970).

[Sverdrup00] P. G. Sverdrup *et al.*, *Sub-continuum thermal simulation of deep sub-micron devices under ESD conditions*, SISPAD, Sept. 6-8, pp. 54 (2000).

[Sverdrup01] P. G. Sverdrup *et al.*, *Sub-continuum thermal simulation of heat conduction in silicon-on-insulator transistors*, J. Heat Transfer **123**, pp. 130 (2001).

[Terris09] D. Terris et al., *Modeling semiconductor nanostructures thermal properties : The dispersion role*, Jour. Appl. Phys. **105**, 073516 (2009).

[Terris09-1] D. Terris *et al.*, *Predicting of the thermal conductivity anisotropy of Si nanofilms. Results of several numerical methods*, Int. J. Therm. Scien. **48**, pp. 1467 (2009).

[Terris09-2] D. Terris et al., *Modeling semiconductor nanostructures thermal properties : The dispersion role*, Jour. Appl. Phys. **105**, 073516 (2009).

[Thompson] S. Thompson, P. Packan, M. Bohr, *MOS Scaling: Transistor Challenges for the 21st Century*, Intel Technology Journal, **Q398**, pp. 1-19.

[Thompson06] S. E. Thompson et al., *Uniaxial-process-induced srained-Si : extending the CMOS roadmap*, IEEE Trans. Electron. Dev. **53**, pp. 1010 (2006).

[TianAPL2011] Z. Tian et al., *On the importance of optical phonons to the thermal conductivity in nanostructures*, Appl. Phys. Lett. **99**, 053122 (2011).

[Vasileska08] D. Vasileska et al., *Semicondutor device modeling*, J. Comput. Theor. Nanosci. **5**, pp. 1 (2008)

[Vasileska10] D. Vasileska *et al.*, *Inclusion of phonon dispersion and its influence on electrical characteristic degradation due to heating effects in nanoscale DSOI devices*, AIP Conf. Proc. **1199**, pp. 493 (2010).

[Vasileska-course] D. Vasileska, *Drift-Diffusion Model: Introduction*.

[Vitusevich03] S. A. Vitusevich et al., *Separation of hot-electron and self-heating effects in two-dimensional AlGaN/GaN-based conduting channels*, Appl. Phys. Let., Vol. **82**, pp. 748 (2003).

[Volovichiev08] I.N. Volovichiev, J.E. Velázquez-Perez and Yu.G. Gurevich, *Transport boundary condition for semiconductor structures*, Solid-State Electron. **52**, pp. 1703 (2008).

[Volz09] S. Volz *et al.*, *Thermal nanosystems and nanomaterials*, Topics in Appl. Phys. **118**, Tokyo (2009).

[Weber77] W. Weber, *Adiabatic bond charge model for the phonons in diamond, Si, Ge, ans α-Sn*, Phys. Rev. **B** 15, 4789 (1977).

[Wong11] B. Wong et al., *A Monte Carlo for phonon transport within silicon structures at nanoscales with heat generation*, Int. J. Heat Mass Transfer **54**, 1825 (2011).

[Young89] K. K. Young, *Short-channel effect in fully depleted SOI MOSFETs*, IEEE Trans. Elec. Dev, Vol. **36**, pp. 399(1989).

[Yu&Cardona95] P.Y. Yu & M. Cardona, *Fundamentals of semiconductors-Physics and materials properties*, Springer, New York, 1995.

[Ziman99] J.M. Ziman, *Principles of the theory of solids*, Cambrige Univ. Press, 2nd edition, 1999.